NORTHWESTERN UNIVERSITY

Active Controllable Light-Matter Interaction in the Flatland

A DISSERTATION

SUBMITTED TO THE GRADUATE SCHOOL

IN PARTIAL FULFILLMENT OF THE REQUIREMENTS

for the degree

DOCTOR OF PHILOSOPHY

Field of Electrical Engineering

By

Zizhuo Liu

EVANSTON, ILLINOIS

September 2018

ABSTRACT

Active Controllable Light-matter Interaction in the Flatland

Zizhuo Liu

Ultrathin optical platform including two-dimensional materials and metasurfaces have emerged as potential candidates for novel nanophotonic applications. In this dissertation, I will present the possibility to achieve full active control of the electromagnetic waves with the platform in the flatland. We could achieve the amplitude control, which will be useful for absorbers and sensors, the spatial phase control, which might lead to holograms and flat lenses, and the temporal phase control, which would find use as frequency converter and isolator. 2D materials plasmonics using monolayer black phosphorus will be calculated and discussed to utilize the intrinsic anisotropic properties from black phosphorus. The extrinsic control by using metal antennas will also be shown in both simulations and experiments for realization of anisotropic absorption by treating black phosphorus as a semiconductor. I will cover the special patterning method using DNA-mediated nanoparticles, which will form the cornerstone to build the desired metasurfaces. By controlling the DNA length, the performance of the metasurfaces could be tuned to switch functionality. Active features of graphene and engineered phase control of metasurfaces

will be discussed to fulfill time-varying metasurfaces. Two additional examples of the spectra control will be also discussed. One is to enhance the transmission through the gold nanoslits with the surface plasmons of graphene. The other is to build the dynamic absorber with phase transition materials vanadium dioxide by tuning the temperature. Then I will briefly show the possibility to combine the anisotropy in plane for the hyperbolic metasurfaces and the emerging inverse-design methods that will help for the flatland optical component designs.

Acknowledgements

First and foremost, I would like to express my deepest gratitude to my advisor, Professor Koray Aydin for his enlightening guidance. When I started my PhD study, I am a complete novice to the field of plasmonics and nanophotonics. Koray has been serving as an excellent guide who showed me from acquiring the fundamental skills to forming the whole picture and making differences. I learnt a lot about how to choose a direction and conduct the effective work to make an initial idea into a complete fulfillment. I will always be grateful for what Koray have taught me in the past five years.

I would like to give special thanks to Professor Mark C. Hersam, Professor Hooman Mohseni, and Professor Selim M. Shahriar for serving as my dissertation committee members. I'm so fortunate to have the opportunity to take the courses from them during my first two years. And many thanks for their valuable comments and suggestions to guide the preparation for this dissertation work.

I must thank my collaborators Spencer A. Wells, Wenjie Zhou, Dr. Qingyuan Lin in Northwestern. We had a lot of fruitful discussions of brainstorming new ideas. Thanks a lot for their hard work to make those ideas become possible to achieve.

And thanks a lot for my lab mates in Metamaterials and Nanophotonic Devices Laboratory. Great thanks to previous group members Dr. Serkan Butun and Dr. Zhongyang Li who helped me to obtain the necessary training and get started. Thanks to Edgar Palacios who shared a lot of experience in the fabrication and characterization. I also want to thank Dr. Hasan Kocer, Dr. Bin Tang, Dr. Xianglian Song, Francois Callewaert, Sina A. Dereshgi, and Wisnu Hadibrata for their discussions and suggestions.

And this dissertation would not be possible without the unconditional support of my family. Thanks for their encouragement and care alongside my journey. I am especially grateful for my parents, who have sacrificed so much so that I could pursue my dreams in United States. I always know that they want the best for me. This dissertation is dedicated to them.

Zizhuo Liu

Evanston, IL

Table of Contents

List of Figures

CHAPTER 1

Introduction

1.1. Motivation: Why flatland optics?

In 1884, a famous satirical science fiction written by Edwin A. Abbott was published in United Kingdom with the name "Flatland: A romance of many dimensions". The book was pseudonymously written by "A Square". And in the book, the author described a two-dimensional universe occupied by lines, triangles, squares, polygons and circles, which were used to stand for different classes in the two-dimensional kingdom. Similar to the described scenario of bizarre properties in the flatland world, flatland optics could also lead to quite interesting properties for both fundamental studies and useful applications.

The light-matter interaction has been one of the most important process in the whole universe. Controlling the light-matter action has enabled fruitful technology breakthroughs that change the way of human living. However, conventional optical component in the bulk forms suffers from the weight and functionality with the emerging need of the light-weight optical devices when the world is embracing the virtue reality (VR), augmented reality (AR) or mixed reality (MR).
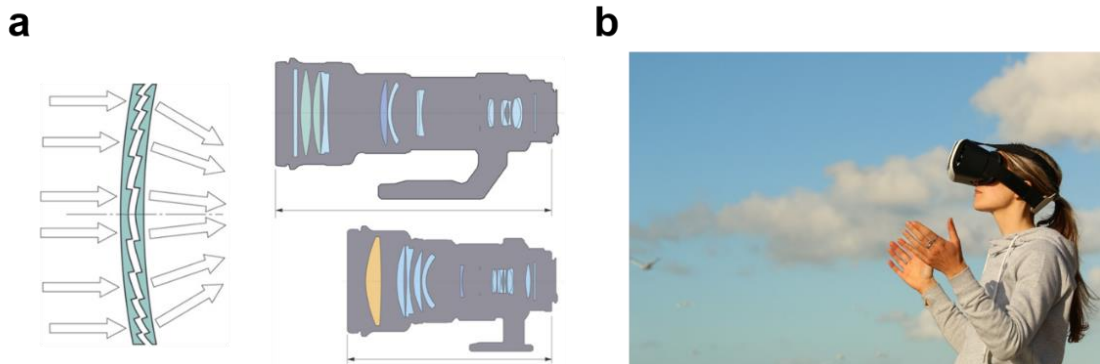
Figure 1.1. (a) DO lenses compared with conventional lenses, adapted from *www.canon.com*. (b) Headset for the VR, AR, MR in the future, adapted from *www.pexels.com*

Conventional lenses with large magnification usually come with a very cumbersome form. Carrying them for photographers could be a really tiring job. By introducing the diffractive optical elements, Canon has proposed so-called DO lenses (Figure 1.1(a)) to make the lenses smaller in length. The light path could be largely controlled by replacing the convex and concave mirrors with the subwavelength structures. With the optical components become thinner and thinner in the flatland, we would expect the lenses could be made even thinner. At the same time, active control of the flatland optical components becomes a necessary task to fulfill the key components in the screen for the headsets (Figure 1.1(b)).

1.2. Two dimensional materials in the flatland

In the flatland optics kingdom, atomically thin two-dimensional (2D) materials have formed a great family to prosper[1]. 2D materials are usually indicated to van der Waals layered materials, which could be exfoliated into few layers or monolayer form. They exhibit interesting electronic, optical, mechanical and thermal properties due to their thicknesses[2]. The 2D materials offer a new class of platform to achieve novel electronic and photonic properties in ultracompact sizes. They can be easily integrated with other optoelectronic platforms and there is no "lattice mismatch" issue. Compared with their bulk parental materials, they could show quite novel electronic and optical properties. Although

such materials have inherently monolayer to few-layer thicknesses, it has been showed that 2D materials can interact strongly with the incident light. And nowadays, there are various 2D materials with different structures and bandgaps, which make them possible to cover a really broad spectrum, as shown in Figure 1.2.
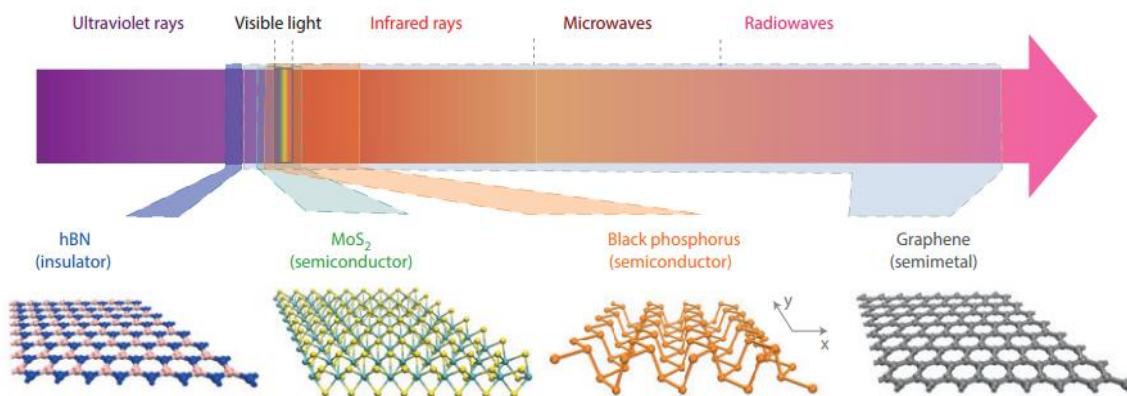
Figure 1.2. Various 2D materials cover a broad spectrum. hBN has large bandgap and works as dielectric. TMDCs has bandgaps in the visible spectra. Black phosphorus covers the spectra from visible to infrared. Broadband material graphene could work even in microwaves and radiowaves[1].

In particular, graphene emerged as a monolayer plasmonic platform[3]. Theoretical and experimental studies confirmed that both propagating and localized surface plasmon modes can be excited in an atomically thin, nanostructured graphene[4-5]. Until the discovery of the graphene as a plasmonic material, noble metals such as silver and gold have been the material of choice both for fundamental and applied research. And besides graphene, it has been shown that mono to few-layer black phosphorus (BP) supports anisotropic plasmonic dispersion due to different effective mass along different crystal directions[6]. 2D plasmonic materials provide a unique opportunity by confining plasmons in an extremely thin optical material and also represent a great challenge for light-matter interactions due to their

inherent atomically thin thickness. With such highly localized electric fields in 2D plasmonics, it is possible to build and integrate devices in smaller sizes that exhibit novel electronic and optical properties compared with traditional bulk plasmonic materials[7-8].

1.3. Metasurfaces in the flatland

Together with 2D materials, metasurfaces also features light-matter interaction in the ultrathin structures composed of artificially designed, subwavelength-thick metallic and/or dielectric resonant elements[9-10]. As opposed to the conventional optical devices like lenses, mirrors, waveguides where device thicknesses are on the order of a wavelength or larger, metasurfaces facilitate strong light-matter interactions by modifying and controlling light propagation within extremely-thin, space-gradient resonators and scatterers. Metasurfaces can be easily designed at will to yield a specific, desired optical performance. In recent years, there has been tremendous progress in designing, realizing and demonstrating wide variety of optical metasurfaces such as flat lenses, holograms, polarization converters, anomalous deflectors, photonic spin Hall effect and so on[11].
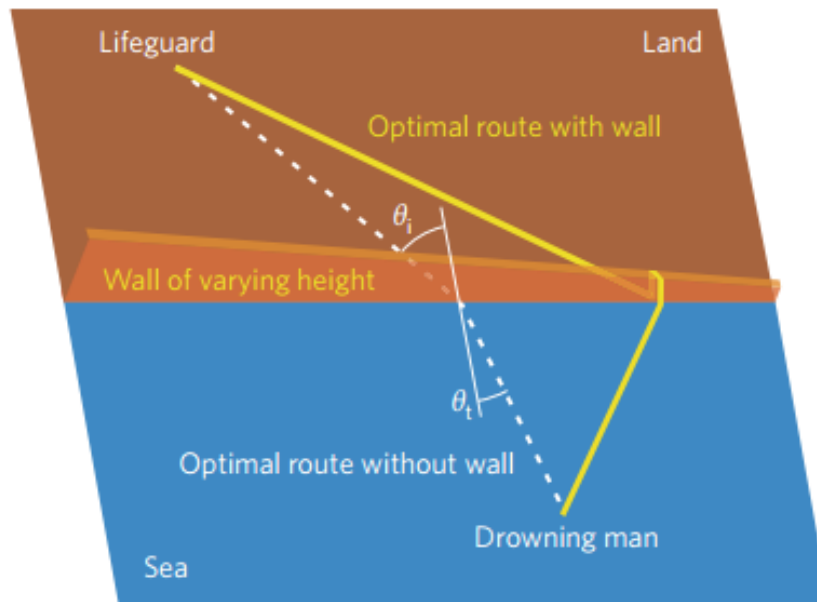
Figure 1.3.1. Analogy of the generalized Snell's law. The metasurface acts like a wall with varying height along the seashore.

The mechanisms for the metasurfaces for phase engineering could be explained with the generalized Snell's law[12]. Richard Feynman has used a famous illustration to explain the refraction of light. When considering how the light would choose path in two mediums with an interface, we could imagine a lifeguard who wants to save a drowning man. Assuming the lifeguard runs faster than swims, the lifeguard needs to choose a point in the seashore to start swimming to save time to reach the drowning man. The optimal path in this scenario will no longer be straight line and the light path of the refraction follows exact the same way. When we include the metasurfaces in the light path, the metasurfaces will introduce the abrupt phase change profile in the interface, which is like the wall with varying height along the seashore. Instead of choosing the previous path, our lifeguard

would prefer to start swimming at a different point to bypass some high walls, as shown in Figure 1.3.1.

The generalized Snell's law for both the refraction and reflection will take the form:

$$n_t \sin(\theta_t) - n_i \sin(\theta_i) = \frac{1}{k_0} \frac{d\Phi}{dx}$$

$$\sin(\theta_r) - \sin(\theta_i) = \frac{1}{n_i k_0} \frac{d\Phi}{dx}$$

The index *i, t* and *r* indicate incident, transmitted and reflected, correspondingly. The additional terms in the right of the equation are the introduced phase change profile along the interfaces.

The first demonstration of the generalized Snell's law was using V-shape gold antenna arrays on a silicon wafer[13] as shown in Figure 1.3.2(a), which studied the symmetric mode and antisymmetric mode supported in this configuration. Eight antennas in one unit cell of $\Gamma = 11 \, \mu m$ covered the phase change of $0 - 2\pi$ at around $8 \, \mu m$ wavelength. Both anomalous reflection and refraction with the mid-IR beam incident were observed. Later people utilized similar antennas configuration with sizes shrunk to make them work at a broadband wavelength from 1.0 to $1.9 \, \mu m$. The broadband performance is believed coming from the broad effective resonances of the V-antennas over the interested wavelengths and the phase change is also approximately linear[14].

Inspired by the proof-of-principle demonstrations, people have worked other reflect-arrays to fulfill the anomalous light guiding with higher efficiency. The most common platform is composed of the metallic antennas and back mirror separated by a thin dielectric layer. The formed cavity could reflect most power of the light to the desired direction without other scattering. And the coupling between the antennas with the image dipole

provides the necessary phase control. Figure 1.3.2(b) shows one example using trapezoid reflect-arrays to guide broadband visible light to the anomalous angle. Instead of using multiple gradient optical resonators, the single gradient building block in one unit cell could also provide the desired phase change and high-efficiency light guiding. The spatial-variant surface produces the anomalous reflected rainbow from red to blue. Besides plasmonic metal antennas, dielectric metasurfaces also emerge as the potential low-loss candidate for light-guiding applications. In one of the flagship work for dielectric metalenses[15], titanium oxide nanofins (Figure 1.3.2(c)) were adopted to build the devices with NA = 0.8 and efficiencies of 86, 73, and 66% at wavelengths of 405, 532, and 660 nm. Another interesting subarea is building active tunable metasurfaces. Figure 1.3.2(d) shows one example utilizing the field-effect modulation of the complex refractive index of conducting oxide layers to achieve dynamic electrical control of the phase and reflection from the metasurfaces[16].
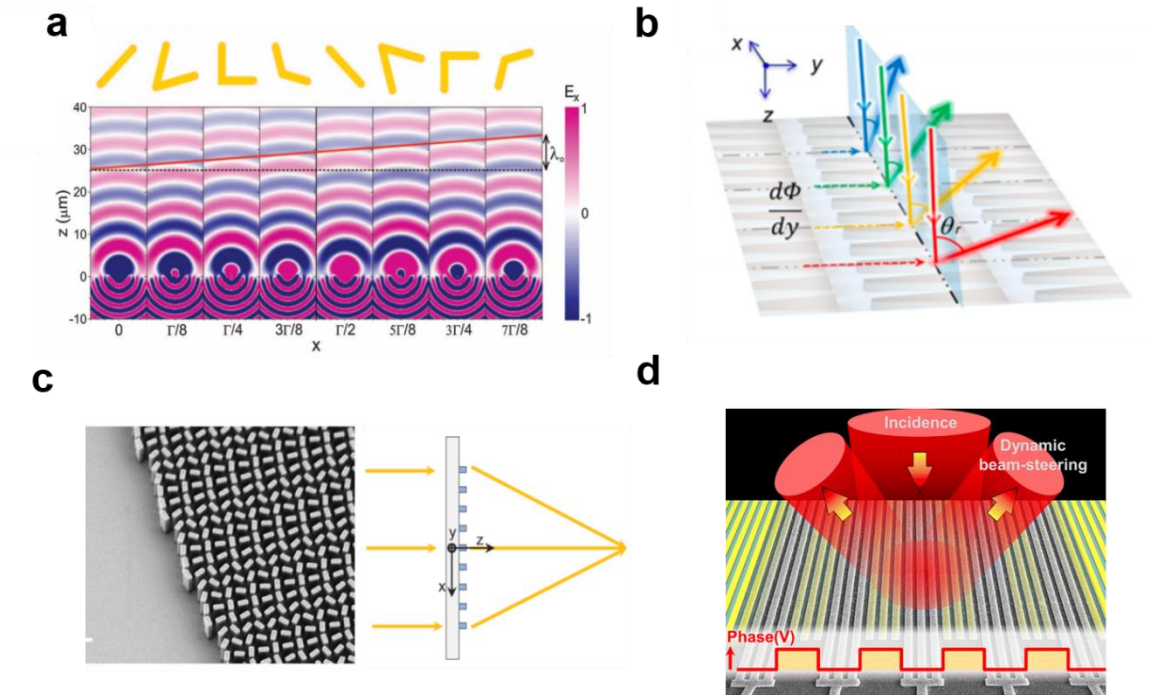
Figure 1.3.2. Various fulfillments and applications of metasurfaces. Figures are adapted from the references mentioned in the text.

1.4. Scope of this dissertation

In this dissertation, I will show the possibility to achieve full active control of electromagnetic waves with the optical platform in the flatland. The electromagnetic wave can be described using following approximation:

$$E = \epsilon e^{i\phi}$$

where ϵ is the wave amplitude that can be relaxed to a slowly-varying component compared with the wavelengths in space scale and the periodicities in time scale. For plane waves, the phase ϕ takes the form of $k\boldsymbol{n} \cdot \boldsymbol{x} - \omega t$. Specifically, the wave vector and the frequency can be deducted from the phase factor:

$$kn = \nabla\phi, \qquad \omega = -\frac{\partial\phi}{\partial t}$$

Thus I would like to show three major types of controls: amplitude control (ϵ), spatial phase control (k), and the temporal phase control (ω).

In Chapter 2, I will cover the amplitude control by incident light polarization, which will be useful for absorbers and sensors. Specifically, 2D materials plasmonics using monolayer black phosphorus will be calculated and discussed to utilize the intrinsic anisotropic properties from black phosphorus. I will also show a general approach to model 2D materials with effective thin film. Then the extrinsic control by using metal antennas will also be shown in both simulations and experiments for realization of anisotropic absorption by treating black phosphorus as a semiconductor.

After showing the amplitude control, I will discuss the spatial phase control for the applications of tunable metasurfaces with DNA dynamics, which might lead to holograms and flat lenses. In Chapter 3, I will cover the special patterning method using DNA-mediated nanoparticles, which will form the cornerstone to build the desired metasurface. By controlling the DNA length, the performance of the metasurface could be tuned to switch functionality.

Then I will show the possibility for temporal phase control, which would find use as frequency converter and isolator. I will move to the topic of time-varying metasurfaces in Chapter 4, in which I combine both the active features of graphene and engineered phase control of metasurfaces. With the power of this specific platform, we could potentially achieve frequency conversion in the flatland.

In Chapter 5, two additional examples of the spectra control will be discussed. In the first part, I use the excitation of the continuous graphene plasmons to enhance the transmission through the gold nanoslits. In the second part, I will show how to build a dynamic absorber with phase transition materials vanadium dioxide by tuning the temperature.

Then in Chapter 6, some outlooks of the flatland optics about 2D materials and metasurfaces will be discussed. I will briefly show the possibility to combine the anisotropy in plane for the hyperbolic metasurfaces. I will also present the emerging inverse-design methods that will help for the flatland optical component designs.

CHAPTER 2

Amplitude control by incident light polarization

2.1. Black phosphorus as an emerging anisotropic material

Black phosphorus (BP) is a recently emerging 2D layered material that can be exfoliated to few layers and monolayer[17]. BP is one allotrope of phosphorus, which is thermodynamically stable at room temperature compared with other allotrope forms. In a monolayer BP, the phosphorus atoms form a hexagonal lattice with a puckered structure resulting in in-plane anisotropic properties[18]. In center of the Figure 2.1, one schematic of the puckered crystal structure is shown. The Raman scattering spectra and photoluminescence measurements from BP revealed its highly anisotropic properties[19].

As shown in Figure 2.1, black phosphorus has been recently utilized for many potential applications. It could be used to enhance the power density to fulfill flexible supercapacitors[20], support bipolar transition in field effect transistors[21], detect poisonous gas[22] and work as photodetectors[23]. BP enjoys a lot of special properties to be potential alternative compared with conventional plasmonic materials and semiconductor.

In this chapter, I will cover the plasmonic properties of monolayer BP as well as using noble metal plasmons to enhance absorption in thin film BP. Plasmons are known to control the local electric field to enhance the light-matter interaction. The controlled electric field would lead to the desired absorption amplitude. Specifically, for BP with anisotropic optical response, we could control the amplitude with the polarization of the incident light.

Figure 2.1. Black phosphorus has been utilized for many applications. Figures are adapted from the references mentioned in the text.

2.2. General approach to model 2D surface with effective thin film

Before the emerging 2D material plasmonics, noble metals like gold and silver have been the material of choice in the fields of plasmonics for either fundamental or applied research. Compare with traditional noble metals, surface plasmons supported by 2D materials have both large localization and long propagation length due to its monolayer thickness.

I would like to start with the general approach to model the 2D materials in our calculation. The finite-difference time-domain (FDTD) methods with Lumerical FDTD

solutions, a commercialized software package will be employed through this dissertation to calculate the electromagnetic responses from different materials and structures.

For 2D materials, there is intrinsic difficulty to model the collective response due to the out-of-plane quantum confinement. In the numerical simulations, we need to work with the surface conductivity with infinitesimal thickness, which is not easy to fulfill in the FDTD method. However, as shown below, we could actually use an effective thin film model to describe the collective response from 2D films with certain assumptions.

Let us first consider the case treating the 2D materials with infinitesimal thickness. Assume we put the 2D surface between two mediums (II) and (III), as shown in Figure 2.2.1. In this case, we will use the surface conductivity from the 2D materials as the boundary conditions. By solving the Maxwell equations, we could easily obtain the dispersion relation as:

$$\frac{\epsilon_3}{k_3} + \frac{\epsilon_2}{k_2} = \frac{-i\sigma_{jj}}{\epsilon_0 \omega}$$

Where ϵ_3 and ϵ_2 are the permittivity for two mediums, σ_{jj} is the surface conductivity along certain crystal direction, k_3 and k_2 are the wavevectors in two mediums.

Figure 2.2.1. Model to calculate the dispersion relation for collective response from 2D surface.

In the other scenario, let's treat the 2D material as a thin film with really small thickness, like 1 nm. The actual number should be determined through the convergence test. Now we consider the triple-layer structures with two layers of dielectric separated by 2D film, as shown in Figure 2.2.2.

III   2D thin film

I

II

Figure 2.2.2. Model to calculate the dispersion relation for collective response from 2D thin film.

In this setting, the dispersion relations could also be easily obtained by solving the Maxwell equations[24]:

$$e^{-2k_1 a} = \frac{\dfrac{k_1}{\epsilon_1} + \dfrac{k_2}{\epsilon_2}\dfrac{k_1}{\epsilon_1} + \dfrac{k_3}{\epsilon_3}}{\dfrac{k_1}{\epsilon_1} - \dfrac{k_2}{\epsilon_2}\dfrac{k_1}{\epsilon_1} - \dfrac{k_3}{\epsilon_3}}$$

where indices indicate the 2D film (1), medium (2) and medium (3) separately. The 2D dielectric function can be modeled with thickness a:

$$\epsilon_1 = \epsilon_{jj} = \epsilon_r + \frac{i\sigma_{jj}}{\epsilon_0 \omega a}$$

where ϵ_r is the background dielectric constant for its bulk form. Since 1 nm is still quite small, we can expand the dispersion into dominant terms and plug in the dielectric function to get:

$$\frac{\epsilon_3}{k_3} + \frac{\epsilon_2}{k_2} = \frac{-i\sigma_{jj}}{\epsilon_0\omega}$$

which is identical compared with the case treating it as monolayer material without thickness.

2.3. Excitation of localized surface plasmons in black phosphorus

Here, we propose and numerically demonstrate that localized surface plasmons can be excited in nanostructured monolayer black phosphorus. We present the study of the electromagnetic response of periodically patterned black phosphorus sheet. We consider the parameters varied in a wide range and the different absorption spectrum is compared due to the inherent anisotropy in BP. In particular, we analyze the confinement of the electromagnetic field in both BP nanoribbon and nanopatch arrays. We demonstrate the anisotropic behavior by replacing BP nanoribbons in *x*-direction (armchair direction) and *y*-direction (zigzag direction). The performance of the structures may allow for the realization of new plasmonic devices which will take advantage of the directional dependence of its plasmon properties.

The photonic properties of a monolayer BP can be described by employing a simple semiclassical Drude model. The conductivity is given as[6]:

$$\sigma_{jj} = \frac{iD_j}{\pi(\omega+\frac{i\eta}{\hbar})} \quad D_j = \frac{\pi e^2 n}{m_j}$$

where j denotes the direction concerned and D_j is the Drude weight. A similar expression has been utilized for graphene[25] with $D = \frac{\mu e^2}{\hbar^2}$. The electron mass along the x direction and y direction can be described by:

$$m_{cx} = \frac{\hbar^2}{\frac{2\gamma^2}{\Delta} + \eta_c} \qquad m_{cy} = \frac{\hbar^2}{2\nu_c}$$

The parameters are determined by fitting the known anisotropic mass. For monolayer BP, we have $\gamma = \frac{4a}{\pi} eVm$, $\Delta = 2eV$, $\eta_c = \frac{\hbar^2}{0.4m_0}$, $\nu_c = \frac{\hbar^2}{1.4m_0}$. We choose the electron doping $n = 10^{13} cm^{-2}$ as well as $\eta = 10\ meV$ to describe the relaxation rate. a is the scale length of the BP and $\frac{\pi}{a}$ is the width of the Brillouin zone.

The dielectric function for a thin film reads (with 2D conductivity):

$$\epsilon_{jj} = \epsilon_r + \frac{i\sigma_{jj}}{2\epsilon_0 \omega a}$$

For a monolayer BP, the relative permittivity is given as $\epsilon_r = 5.76$.

In the FDTD simulations, BP film thickness (a) is chosen to be 1 nm. This audacious assumption will speed up the simulation time and resemble the real results as long as the simulation mesh is fine enough in the BP film. In our simulation setup, we choose the mesh to be 0.25 nm.

In our designs, periodic monolayer BP nanoribbons are placed on a transparent insulator and an optically thick gold mirror. The metallic mirror is used to reflect light and suppress the transmission. Compared with free-standing BP nanoribbons, the dielectric layer between the BP and gold mirror forms a Fabry−Perot cavity and therefore increases the interaction of light with monolayer BP. Dielectric thickness can be chosen to maximize the absorption using Fabry−Perot interference. In our simulations, the dielectric thickness is chosen to be 5 μm . We performed full-field electromagnetic simulations with the wavelengths between 20 - 80 μm. For the optical constants in the simulation, we used a

constant, nondispersive refractive index of n = 1.7 for the dielectric spacer and perfect electric conductor model for the metallic mirror.

Localized plasmon resonances can be excited with an incident light when electric field is perpendicular to the nanoribbons (Figure 2.3.1(a))). Since metallic mirror suppresses the transmission, absorptivity (A) can be calculated with a simple formula $A = 1 - R$, where R is the reflectivity from the simulated structure.

Because BP exhibits anisotropic optical and electronic properties along x- and y-directions, we anticipate polarization-dependent localized plasmon resonance behavior for monolayer BP nanoribbons along the armchair and zigzag directions. In order to investigate the effect of anisotropic optical properties on the plasmonic behavior of the BP, we performed electromagnetic (EM) simulations for two different nanoribbon structures as shown in Figure 2.3.1(b). The structural parameters for both x- (armchair) and y- (zigzag) directions are chosen to be the same. Having the period $p = 250$ nm and the monolayer BP ribbon width $w = 150$ nm, the absorption spectrum is plotted in Figure 2.3.1(b). For both cases, an absorption peak has been observed for s polarized light. Because of the mass
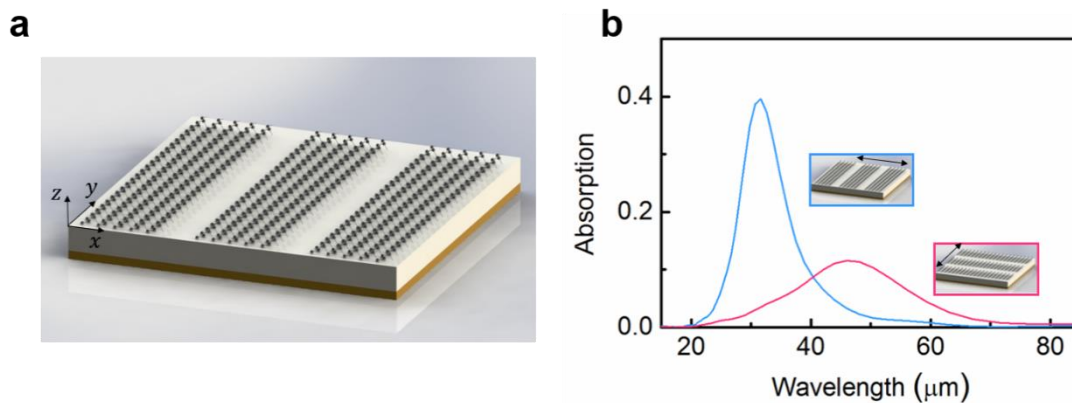
Figure 2.3.1. (a) Schematics of periodically patterned BP nanoribbons. (b) Anisotropic absorption spectrum can be observed in BP ribbon arrays along x- and y-direction. The arrows in the inset indicate the polarization of the electric field.

anisotropy, the smaller mass along x indicates higher resonance frequency therefore shorter wavelength. Compared with the zigzag direction (red line), the absorption peak in armchair direction is higher and the resonance line width is narrower. This result suggests that the black phosphorus is optically more lossy for the zigzag direction at the corresponding resonance wavelength. As mentioned before, because graphene has also been described with the similar Drude model but with different Drude weight, the plasmons in BP nanoribbons also behave differently in scales compared with graphene nanoribbons.
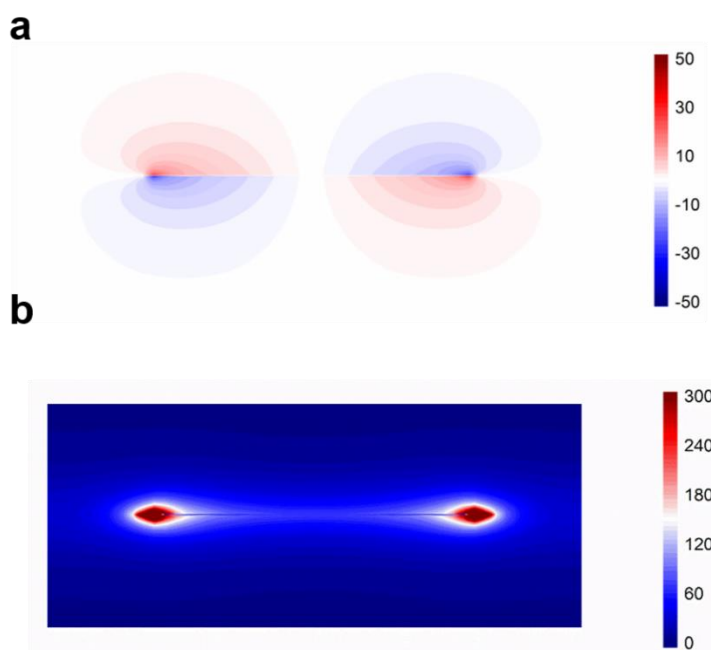
Figure 2.3.2. (a) Calculated electric field amplitude, E_z for one BP nanoribbon unit cell (along x-direction). (b) Calculated total electric field intensity ($|E|^2$) for one BP nanoribbon unit cell (along x-direction). Electromagnetic field is localized around the edges of the nanoribbon.

The sideview electric field profile of the vertical component (E_z) shown in Figure 2.3.2(a) is plotted with the case of the nanoribbon arrays along *x*-direction at the resonance wavelength (31.5 μm). Positive and negative dipoles can be easily seen indicating a localized plasmon resonance behavior. The edges of the BP nanoribbon distort the in-plane component of the electric field. Also, for the edge surface plasmon modes, the electric field enhancement is mostly pronounced around the edges, which resemble the edge modes in graphene ribbon structures. Figure 2.3.2(b) confirms that the total electric field intensity is localized around the two edges of the BP nanoribbon.

In Figure 2.3.3, we show the side-view electric field distribution for the ribbons patterned along *y* direction. Compared with Figure 2.3.2, the field resembles the *x* case however with lower amplitude.
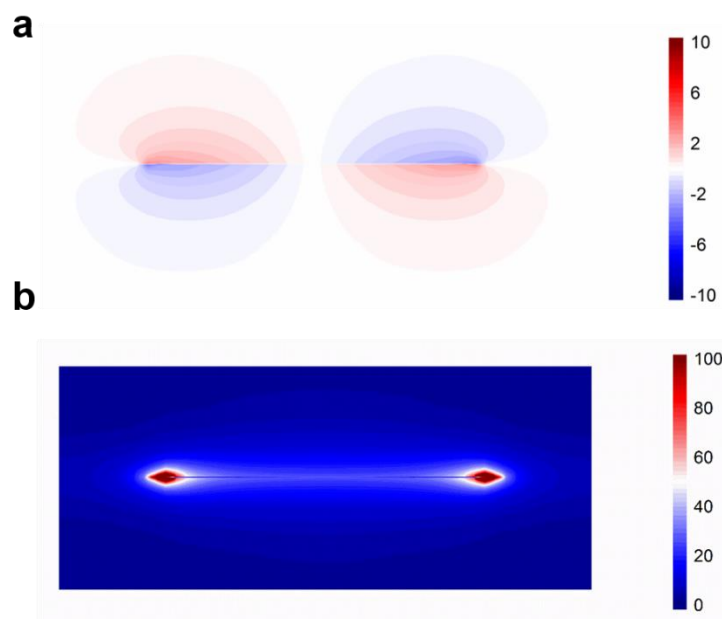
Figure 2.3.3. (a, b) Side-view electric field distribution of one BP ribbon along *y* direction. Electromagnetic field is localized around two edges of the ribbon.

Figure 2.3.4 shows the absorption of freestanding BP nanoribbons and graphene nanoribbons with the structure parameters described for Figure 2.3.1. Compared with Figure 2.3.1(b), the absorption in both armchair and zigzag cases has decreased, which is due to the weak light-matter interaction in the atomically thin BP film. The peak positions have also moved to new wavelengths, which is caused by the changing of environmental index below the BP film. In this case, the overall shape of the spectrum keeps similar. Compared with freestanding graphene, BP interacts much weaker with light, which could be confirmed from the permittivity data. We've run the simulation for free standing graphene nanoribbons with Fermi level 0.64 eV and mobility 10000 cm^2/Vs The resonance appears at smaller wavelength with much sharper shape.
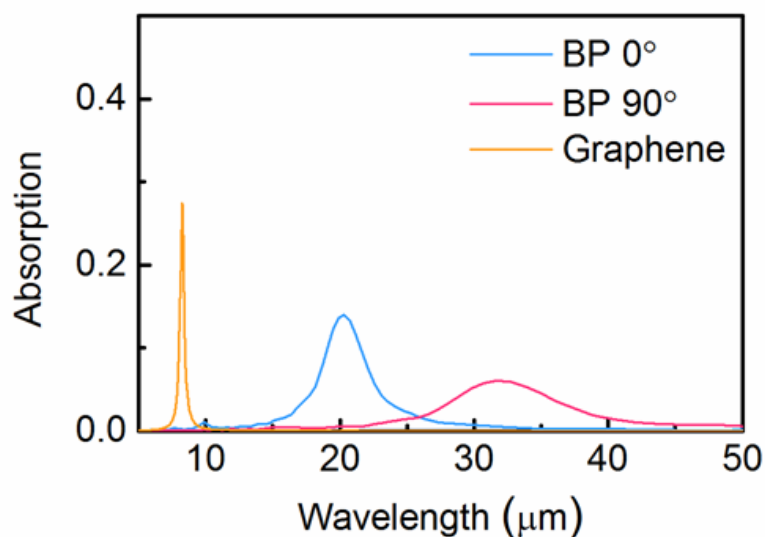
Figure 2.3.4. Absorption spectrum of the freestanding BP nanoribbons along *x* and *y* direction and freestanding graphene nanoribbons.

To enhance the light-matter interaction as well as absorption, we design the Fabry-Perot setup below the BP film. In the simulation setup, the thickness of the dielectric between the BP ribbons and the bottom metal will influence the absorption in the BP. With various dielectric thickness, the electric field as well as the absorption in BP film can be tuned. Figure 2.3.5 shows the absorption spectra for both x and y cases with thickness changing from 1μm to 30 μm. The period and widths kept at 250 nm and 150 nm separately. The absorption resonance for the ribbons along x direction is at about 31.5 μm and it keeps at the same position when we change the dielectric thickness since it is just determined by the size of the BP nanostructures. We observe the absorption reaches maximum at certain thickness.
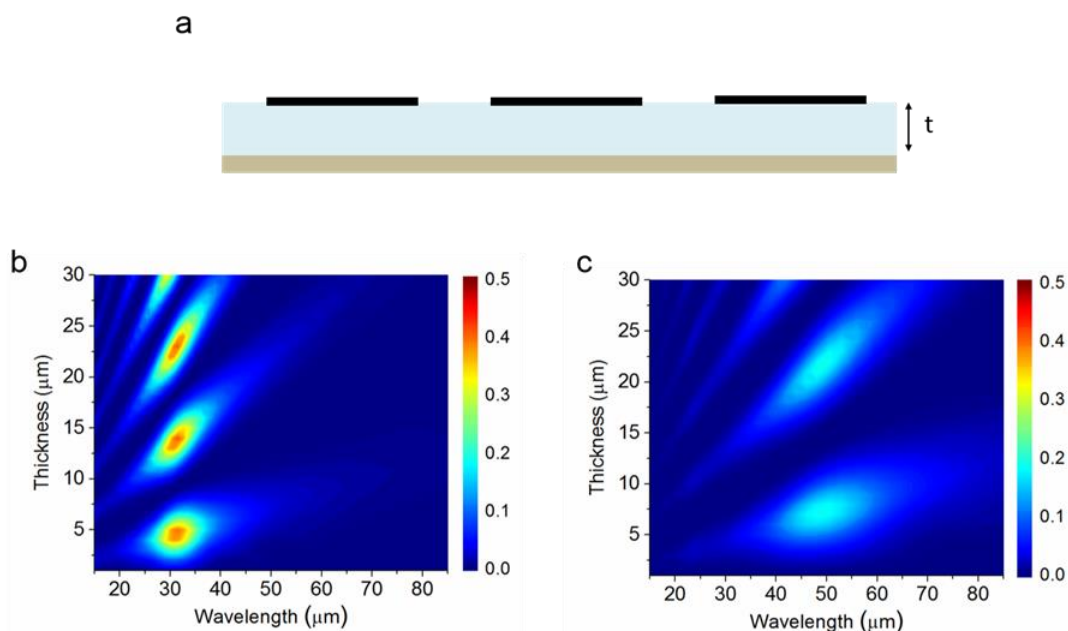
Figure 2.3.5. (a) Schematics of periodically patterned BP ribbons with t indicating the dielectric thickness. (b, c) Absorption maps of two directions with fixed period 250 nm, fixed widths 150 nm and various dielectric thicknesses.

Figure 2.3.6 provides the explanation for the thickness dependency. The electric field intensity is plotted for the x cases with thickness 4.6 µm, 9.2 µm and 13.8 µm. The first and third one indicates the absorption at the maximum, while the second shows the absorption minimum. Since the dielectric constant is chosen at 1.7, the effective wavelength of the resonance is about 18.5 µm. These three numbers of the thickness are just the lengths of the quarter, half and three-quarter effective wavelengths. At 4.6 µm and 13.8 µm, the electric field intensity reaches maximum which increases the absorption either. At 9.2 µm, the electric field intensity is almost 0 and the absorption is mainly reduced.
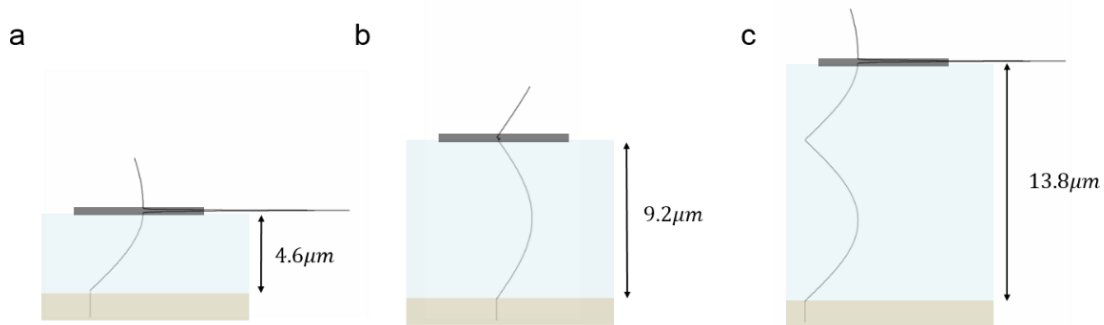
Figure 2.3.6. (a, b, c) Schematics and electric field intensity with three particular thicknesses. The BP is placed exactly at either the maximum or the minimum of the field intensity in these thicknesses.

We have also performed additional simulations for different nanoribbon widths as well as different periodicities in order to understand the effect of the nanoribbon array parameters on the observed plasmon resonance behavior. In Figure 2.3.7, we summarize

our results for monolayer BP nanoribbon arrays with various widths. In these simulations, the periodicity of the arrays is kept at 250 nm, as shown from the side-view in Figure 2.3.7(a, b) for ribbons along both x- and y-directions. The width is changed from 0 nm (no BP) to 250 nm (continuous BP). Absorption spectra as a function of wavelength and varying widths for nanoribbon arrays along x- and y-directions are plotted in Figure 2.3.7(c, d), respectively. It is clear that the absorption peak position and therefore the resonance wavelength increases to longer wavelengths with increasing nanoribbon width, which follow the scaling behavior of localized plasmons. The wider BP nanoribbons support the electromagnetic oscillations at longer wavelengths. The shift trends are similar for both armchair and zigzag directions, but the absorption peak is much larger for armchair direction (x). In Figure 2.3.7(e, f), we plot the absorption spectra for different nanoribbon widths along x- and y-directions separately. It can be seen that with increasing width, the resonance peaks become broader due to the increasing optical losses at longer wavelengths. One interesting property we note is that there is an absorption maximum of 0.47 for 190 nm width nanoribbon with a periodicity of 250 nm.
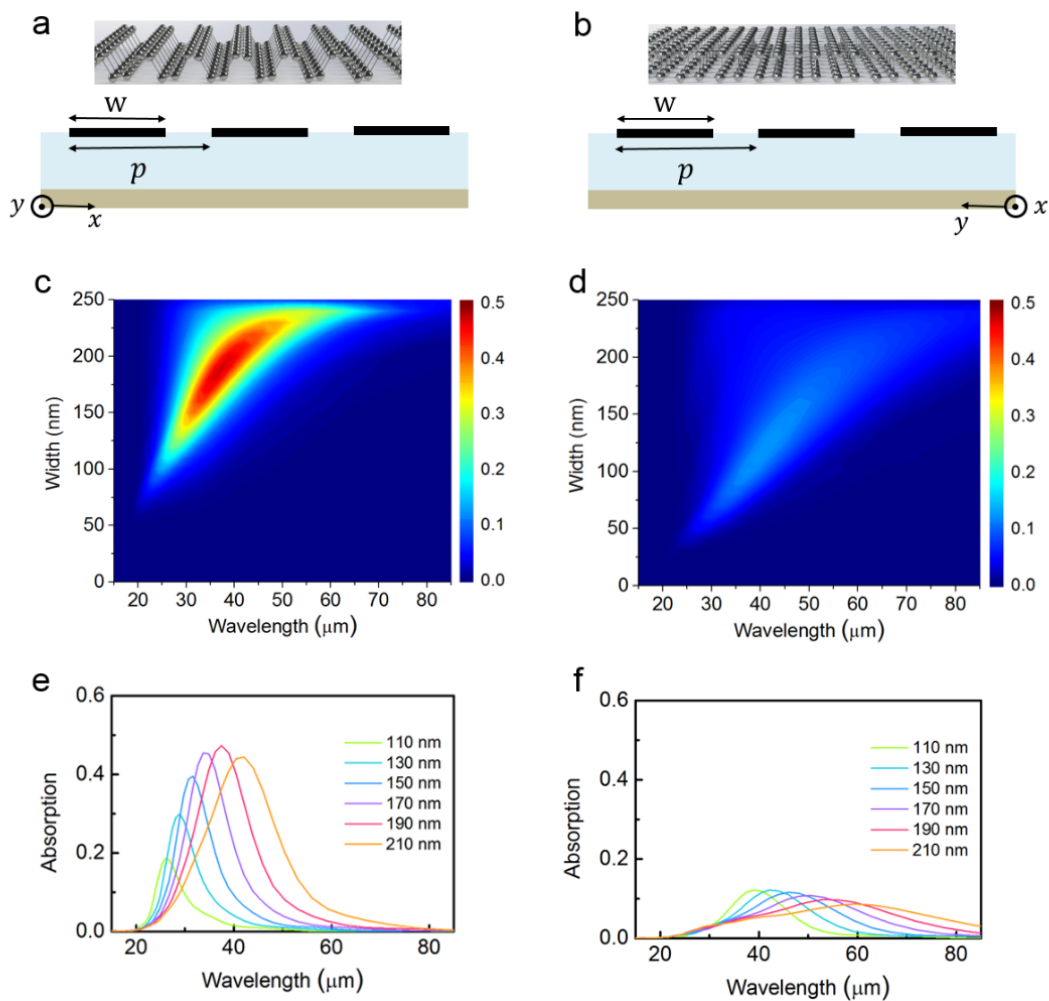
Figure 2.3.7 (a, b) Schematics and perspective side view of the BP ribbon arrays along x-and y-direction separately. (c, d) Absorption map of two directions with fixed period 250 nm and various widths. (e, f) Absorption spectra for various widths of two directions.

Additional simulations are performed for different periodicities changing from $p = 150$ to 500 nm for fixed nanoribbon width of $w = 150$ nm. Results are summarized in Figure 2.3.8. For small periodicities (periodicity is closer to the nanoribbon width), there is a strong coupling between neighboring nanoribbons resulting in a change for the resonance wavelength positions. The absorption increases for reduced periodicities mainly due to the

smaller gap between the nanoribbons and stronger inter-ribbon coupling. However, for larger periodicities where the interaction between neighboring BP nanoribbons are weak the position of the absorption peak shifts to shorter wavelengths. Also, the total absorption decreases due to the smaller volume of the BP in certain areas. For the large period case, the resonance almost stays at the same wavelength as expected for a localized plasmon resonance, and the plasmon wave vector follows the trend $q \sim \frac{\pi}{w}$.
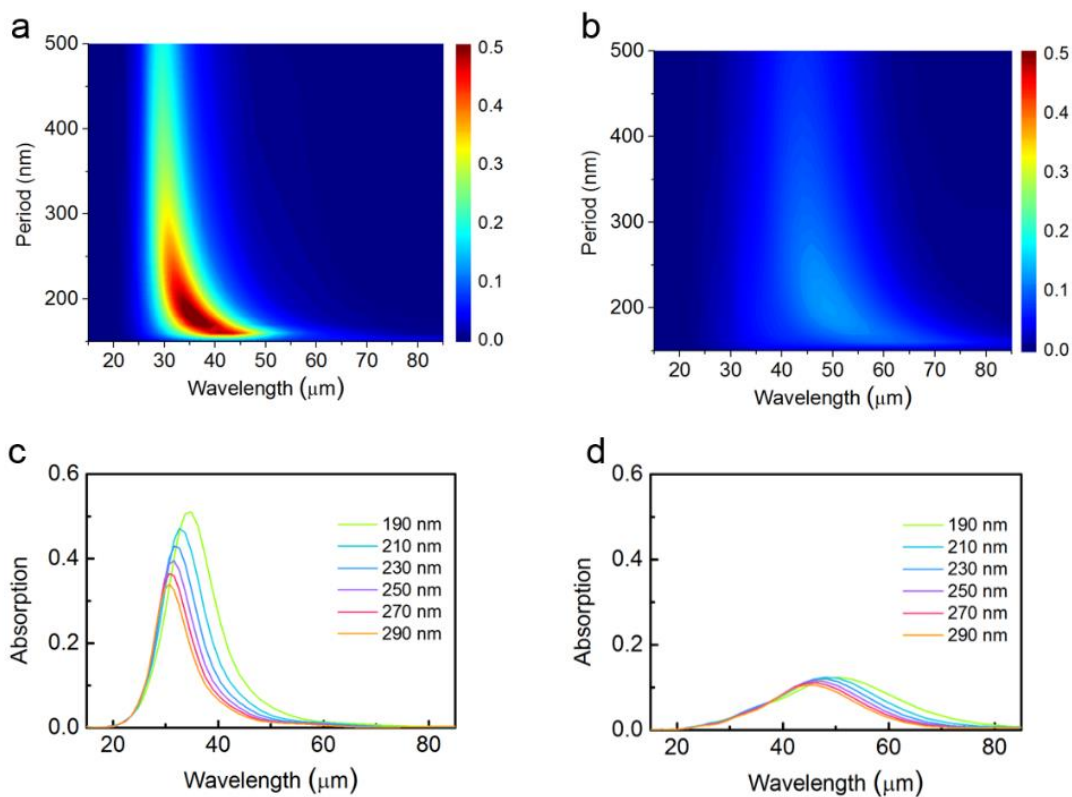
Figure 2.3.8. (a, b) Absorption map of two directions with fixed width 150 nm and various periods. (c, d) Absorption spectra for various periods of two directions.

We've run additional simulation for the case of large period when the resonance peak is not changing when increasing the period and keeping the same BP nanoribbon width. In

this large period case, the resonance position is mainly determined by the ribbon width only. So we've run the sweep with different nanoribbon width (changing from 100 nm to 450 nm) with large period (period to width set as 3:1) and mark the plasmonic dispersion by picking up the resonance peak positions.

There could be the anomalous reflection phase at the ribbon edges. And the exact formula could possibly be written as q=(constant)$\times\pi/w$, such as graphene ribbon case[26]. Since we don't have any experimental data, it is not fair to assume an arbitrary phase here to calculate the actual wave vector q. We just plot the dispersion by comparing the "plasmon resonance" vs "π/w", which mimics the plasmon behavior shown in BP (Figure 2.3.9).
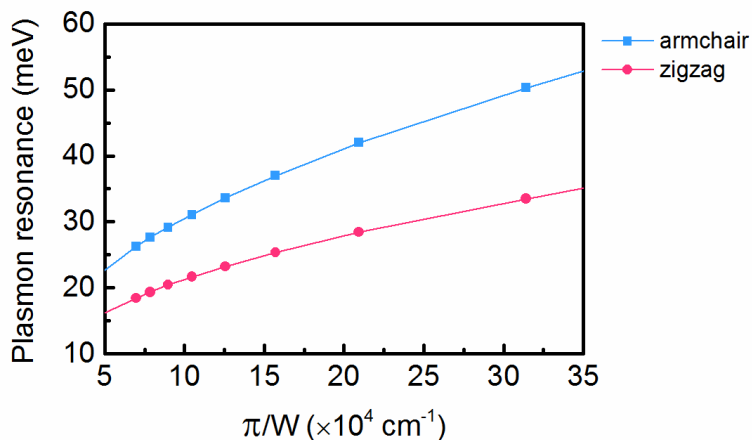
Figure 2.3.9. Dispersion relations of BP nanoribbons in armchair and zigzag direction.

Inspired by the anisotropic plasmonic response of the BP nanoribbon arrays along x and y-direction, we can construct BP nanopatch arrays (square shaped isolated BP nanostructures) as shown in Figure 2.3.10(a). For consistency and ease of comparison with

earlier discussions, we choose the nanopatch array parameters as $p = 250$ nm and $w = 150$ nm in both x- and y-directions. When light is polarized along the x-direction (0°), we observe a high absorption resonance peak at shorter wavelength. For y-polarization, that is, the polarization angle is 90°, the resonance shifts to longer wavelengths as expected due to higher effective mass along the zigzag (y) direction. Compared with Figure 2.3.1(b), the resonance wavelengths are kept at the same position as expected. But the absorption intensity is reduced, which can be explained due to the discontinuity of the ribbons in the
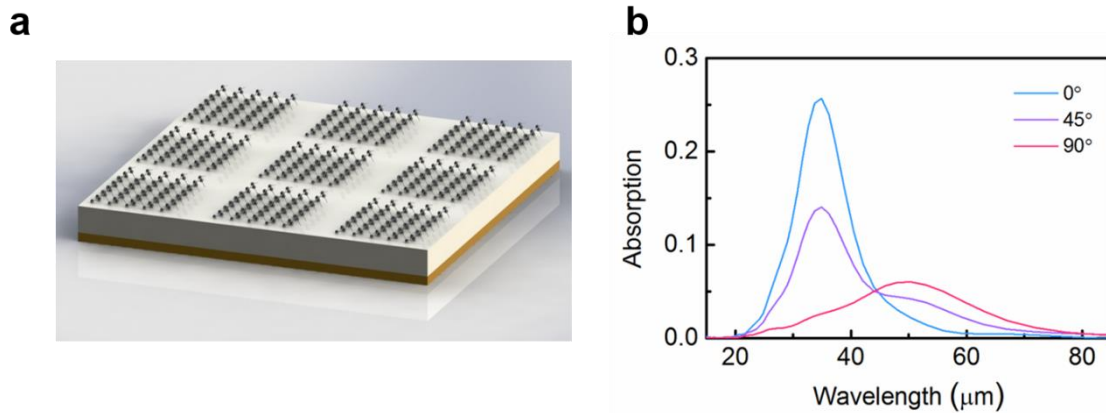
Figure 2.3.10. (a) Schematics of periodically patterned BP nanopatches. (b) Anisotropic absorption spectrum can be observed when applying light with different angles.

case of nanopatch arrays resulting in lower BP volume. Interestingly, for polarization angle of 45° localized plasmon resonances for armchair and zigzag directions can be excited simultaneously. Absorption intensity reduces at respective plasmon resonance wavelengths due to reduced light intensity at corresponding x- and y-directions.
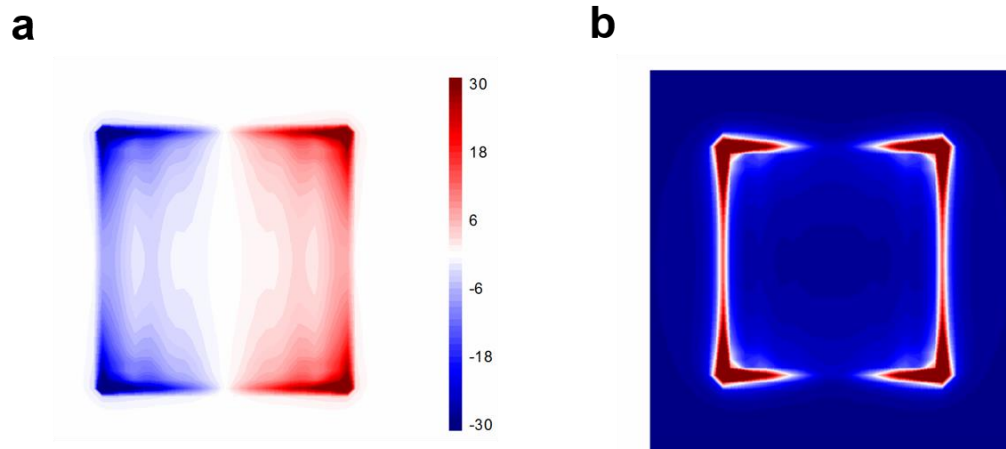
Figure 2.3.11. (a) Calculated electric field amplitude, E_z for one BP nanopatch unit cell (along x-direction). (b) Calculated total electric field intensity ($|E|^2$) for one BP nanopatch unit cell (along x-direction).

In order to understand the resonance behavior for monolayer BP nanopatch arrays, we calculated the amplitude and electric field intensity using EM simulations. Figure 2.3.11(a) plots the amplitude of the E_z for x-polarization (0°) right above the BP film and clearly illustrates the electric dipole behavior expected in structures exhibiting localized plasmon resonances. Total electric field intensity profile shown in Figure 2.3.11(b) implies that the electric field is mostly localized at the left and right edges corresponding to the polarization of the light. The electric field intensity is highest around four corners of the square due to the sharpness in shape.

2.4. Plasmon for enhanced light-matter interaction

After discussing treating BP as the plasmonic material to enhance the light-matter interaction. We will discuss the possibility to use the extrinsic plasmons to enhance the absorption in thin BP film by treating it as a semiconductor.

Plasmonic nanostructures are widely utilized in enhancing light-matter interactions by strongly localizing electric fields around localized surface plasmon resonances (LSPRs). In particular, optical emission and absorption in layered 2D materials including semiconducting transition metal dichalcogenides (TMDCs) can be enhanced significantly around LSPR frequencies[27-29]. BP has attracted interest as an optoelectronically active 2D semiconductor[6, 18, 21, 30-34]. Unlike gapless graphene or TMDCs with wider bandgaps, the moderate 0.3 eV bulk bandgap of BP makes it a promising electronic and optoelectronic material to enable optical performance from visible to mid-IR wavelengths[35-41]. Additionally, BP exhibits an anisotropic optical response due to its puckered crystal structure[42-45], allowing for polarization-dependent photoresponse due to its strong intrinsic linear dichroism[46-51]. This unique property makes BP stand out from other existing materials working in the visible wavelengths, either 2D TMDCs or conventional semiconductor such as silicon. Observing and controlling the anisotropy of BP can lead to the new trail for designing optoelectronic devices fulfilling novel functionalities. Although isotropic plasmon-enhanced optical absorption in TMDCs has been investigated[52-55], plasmon-enhanced photoresponse in anisotropic BP has not yet been achieved. Aside from the plasmon-enhanced light-matter interaction, we further extend possibilities of plasmonic nanostructures to include the coupling of an anisotropic plasmonic lattice rotationally

commensurate with an anisotropic semiconductor, a concept never previously demonstrated. These hybrid structures provide significant control over the polarization-dependent optical properties of the plasmon-BP hybrid material system[30, 56], which not only enable polarization-dependent optical absorption and photoresponse enhancement but also elucidate the coupling mechanisms between the extrinsic anisotropy of plasmonic antennas and the intrinsic anisotropy of BP. Moreover, as other examples of anisotropic 2D materials emerge[54, 57-58], our work could serve as a model framework for future studies on anisotropy control.

What we want to demonstrate here is a hybrid material platform composed of encapsulated BP flakes and plasmonic resonators that exhibit polarization-controlled optical anisotropy. We show that by exciting the silver LSPRs in periodic isotropic nanodisk or anisotropic rectangular nanopatch arrays, the absorption as well as the photoresponse in BP can be enhanced either in a similarly isotropic or an anisotropic manner due to the strongly localized plasmon-induced electrical field penetrating into the BP flake. The hybrid plasmon-BP thin film platform proposed in this study is likely to enable the design and realization of high-performance polarization-sensitive and anisotropic optoelectronic devices including photodetectors, photovoltaic devices, and thermal emitters.

2.5. Isotropic silver antennas for optical anisotropy control

In this study, we investigate symmetric as well as asymmetric plasmonic nanostructures to investigate polarization-controlled optical and optoelectronic properties of exfoliated BP

flakes. We first utilized periodic silver nanodisk arrays on top of BP flakes as an isotropic, symmetric plasmonic resonator platform exhibiting polarization-independent LSPR (Figure 2.5.1(a)). The device fabrication started with the exfoliation of BP flakes onto a 300 nm SiO_2/Si substrate. After the exfoliation, we fabricated two 10/40 nm of Ni/Au electrodes separated by 10 µm as contact pads (In Figure 2.5.1(b), one additional set of electrodes were prepared for spare use, while only the top set was used in the measurements) and then encapsulated the entire device with a 10 nm thick Al_2O_3 thin film grown by atomic layer deposition (ALD) to protect the BP from degradation[59]. Following encapsulation, structural characterization was performed using atomic force microscopy (AFM) and optical microscopy. AFM results indicated that the BP flake has a uniform thickness of 36 nm. Periodic silver nanodisk arrays (Figure 2.5.1(c)) were fabricated using electron-beam lithography followed by electron-beam deposition of silver and lift-off. Figure 2.5.1(d) shows a scanning electron microscopy (SEM) image of silver nanodisk arrays on top of BP. The crystal orientations of armchair (x) and zigzag (y) directions (shown in Figure 2.5.1(c)) were determined by measuring the reflection spectrum by exciting BP with linearly polarized light with varying polarization angles.

a

b

c

d
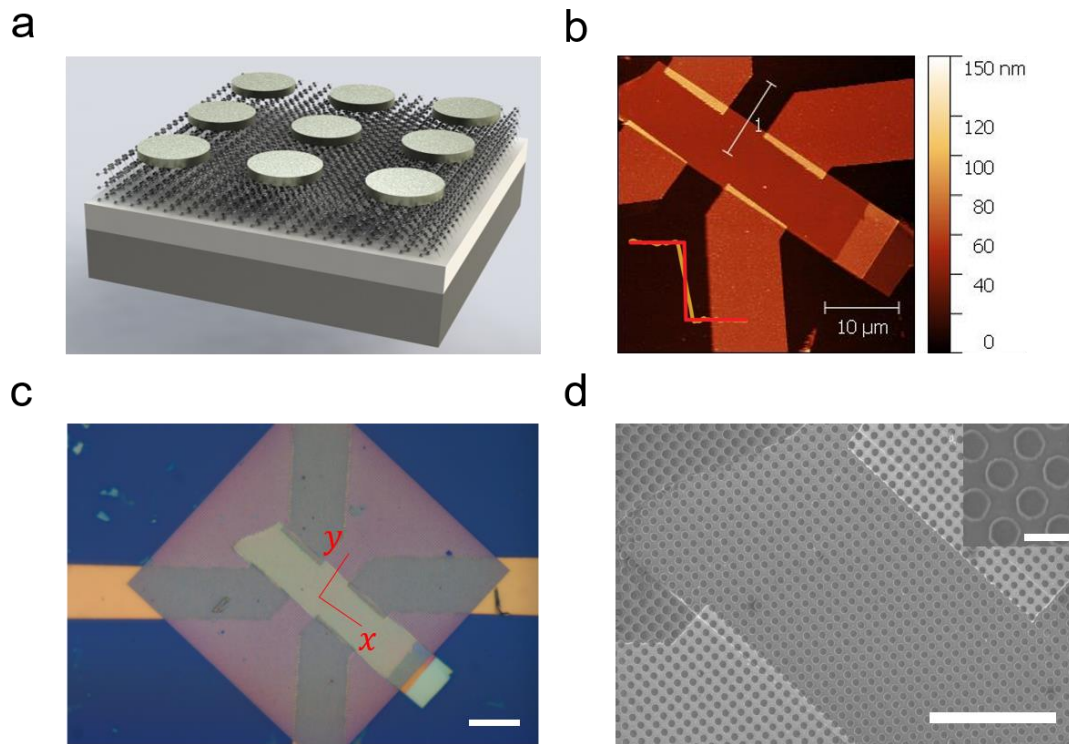
Figure 2.5.1. (a) Schematic of periodically patterned silver disks on exfoliated BP. (b) AFM micrograph of a BP flake prior to plasmonic antenna fabrication with the height profile for trace 1 shown in the inset. The thickness of the BP flake is 36 nm. (c) Optical microscope image after deposition and lift-off. The shaded area on top of the device denotes the silver plasmonic arrays. The crystal orientations, x and y, are labeled in red. The scale bar is 10 μm. (d) SEM image of the silver nanodisk array on top of the BP flake. The inset shows a zoomed-in version of the plasmonic nanodisks. The scale bar is 5 μm and 500 nm respectively.

The diameter and periodicity of the Ag nanodisk resonator arrays are optimized by performing full-field electromagnetic simulations based on the FDTD method. Ag nanodisks with a diameter of 320 nm that were arranged periodically with a periodicity of 420 nm in both directions result in an LSPR wavelength of ~600 nm. These structural parameters result from the optimization for the best performance of BP absorption enhancement after many electromagnetic simulations. In the simulation setup, the

dispersive anisotropic complex dielectric permittivity of BP was obtained from a previously published material model[60]. We assumed a constant refractive index of 1.6 and 1.46 for the Al_2O_3 and the SiO_2, respectively. The complex dispersive refractive indices of Ag and Si were fitted from the Palik database[61]. We calculated and measured the reflection spectra of a 36-nm thick BP flake without and with Ag nanodisk arrays. Figure 2.5.2(a) and 2.5.2(c) show the calculated and measured reflection spectra of the BP flake with ALD layer prior to plasmonic nanodisk patterning. We observed different reflection intensities for various incident light polarization angles arising from the anisotropic response of BP. Here, we used this reflection measurement technique to differentiate the armchair and the zigzag crystal directions. The armchair direction (0°) of BP has lower reflectivity and thus higher optical absorption compared with the zigzag direction (90°). For polarization angles of 30° and 60°, which were not along the principal axes, the reflection power followed the trends in between while the scatter fields would be of elliptical form due to the birefringence of BP. We also noticed there were small dips near 600 nm in reflection measurements shown in Figure 2.5.2(c). These dips were attributed to small portion of phosphorene oxides which were inevitably formed during the encapsulation, as has been observed in previous studies[42, 44, 46]. Since these dips are so small, we do not expect they could play important roles when combined with the metal LSPR resonances. Figure 2.5.2(b) and 2.5.2(d) plot simulated and measured reflection spectra of a BP flake with Ag nanodisk arrays. In both simulations and measurements, a reflection dip around 600 nm was observed due to the LSPRs of the periodic Ag nanodisk array. We notice a slight resonance wavelength and reflection amplitude mismatch between our simulated and measured results, which is attributed to the differences between the material index in the literature

and our BP samples as well as deviations from the ideal geometry of Ag nanodisks that occurred during nanofabrication.
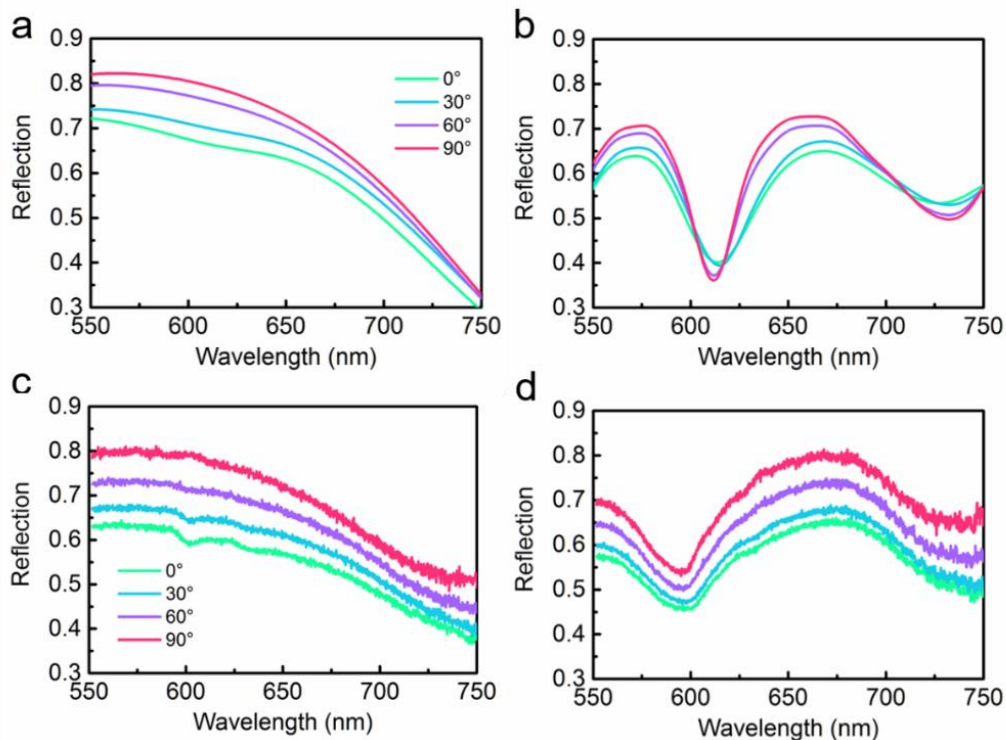
Figure 2.5.2. (a, c) Calculated and measured reflection spectra of a 36 nm thick BP flake without Ag nanodisks. (b, d) Calculated and measured reflection spectra of the hybrid material system composed of the plasmonic nanodisk array fabricated on top of the BP flake.

In Figure 2.5.2, we plot the reflection from the entire sample including reflections from the Ag nanodisks, BP flake, and the SiO_2/Si substrate. However, for practical optoelectronic applications, it is the optical absorption in the BP itself that is responsible for photocarrier generation. Therefore, it is important to quantify the optical absorption in the semiconducting BP flake by isolating it from the absorption from the Ag nanostructures

and the silicon substrate. In simulations, it is straightforward to calculate the optical absorption in BP by placing power monitors within the BP flake. Figure 2.5.3(a) and 2.5.3(b) plot the simulated optical absorption spectra in BP without and with Ag nanodisk arrays for four different linear polarization angles. As mentioned earlier, BP exhibits higher optical absorption when incident light is polarized along the armchair direction (0°). The optical absorption gradually decreases once the polarization angle is increased and reaches the minimum value once it is parallel to the zigzag direction (90°). The absorption enhancement stems from the enhanced localized electric field induced by LSPRs of Ag nanodisks. The larger the enhanced electric field could penetrate into the BP film, the higher the absorption enhancement will be. We would expect better performance with thinner ALD layer separating the resonant elements and BP, while the drawback is the shorter time before degradation. In Figure 2.5.3(b), we observe enhanced optical absorption at ~600 nm corresponding to the LSPR wavelength of the Ag nanodisks. There is a slightly blue shift of the resonance peaks when increasing the polarization angles. We believe it is coming from the influence of the intrinsic higher absorption along armchair direction near ~620 nm, as observed in Figure 2.5.3(a).

Quantifying the optical absorption in the BP thin film, as opposed to the entire system, using optical measurements alone is not possible since Ag nanodisks and the Si substrate also absorb light. However, one can make use of an electrical measurement technique to collect photo-generated carriers in the BP flake resulting from optical absorption. In particular, we performed photocurrent measurements for BP flakes without (Figure 2.5.3(c)) and with (Figure 2.5.3(d)) the Ag nanodisks. The BP photoresponse spectra without Ag nanodisks exhibit flat, non-resonant behavior that agrees well with the optical

absorption simulations shown in Figure 2.5.3(a). On the other hand, we observe enhanced photoresponse from the BP thin film at ~600 nm in the presence of plasmonic nanostructures for all polarization angles. Specifically, the photoresponse enhancement is 2 and 10 times for armchair and zigzag directions, respectively. We note that one must take care while interpreting the electrical measurements compared with the optical absorption, since photogenerated carriers require both generation and transport to the contacts to be measured as photocurrent. And previous studies have revealed that the photoresponse in BP film was dominated by thermoelectric and bolometric process instead of photovoltaic effect. Indeed, we observe that the measured photoresponse spectra exhibits a broader linewidth when compared with the absorption spectra. Similar behaviors could be observed in the previous work[46, 62] The broadening is most likely due to the loss from the contact resistance and the Schottky barriers. Since the previously noticed resonance blue shift in the absorption spectra is ~10 nm, the phenomenon is not observed in the photocurrent measurements where the full width at half maximum (FWHM) of the resonance is ~100 nm.
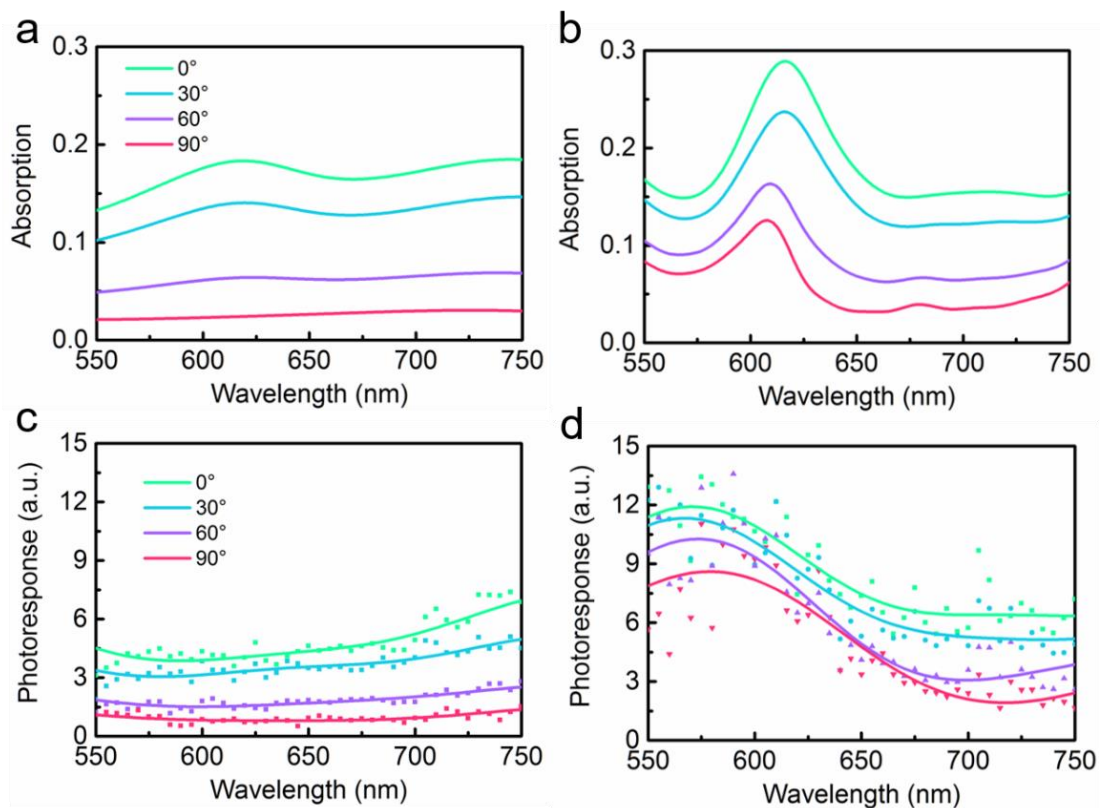
Figure 2.5.3. (a, b) Calculated absorption in BP and the hybrid BP/plasmonic array structure. (c, d) Measured photoresponse in BP and the hybrid BP/plasmonic array structure. Dots and the lines are referred to the raw measurements and the fitted lines.

2.6. Anisotropic silver antennas for optical anisotropy control

As well as enhancing optical absorption and photoresponse in an anisotropic BP flake in the presence of isotropic plasmonic nanodisk resonators, it is also possible to control absorption and enhancement asymmetrically by using anisotropic plasmonic resonators that cause different LSPR wavelengths for different incident polarization angles. In other words, we aim to combine the extrinsic anisotropic plasmonic structures with the intrinsic

anisotropic properties, to obtain a system with enhanced anisotropy compared with planary BP film.
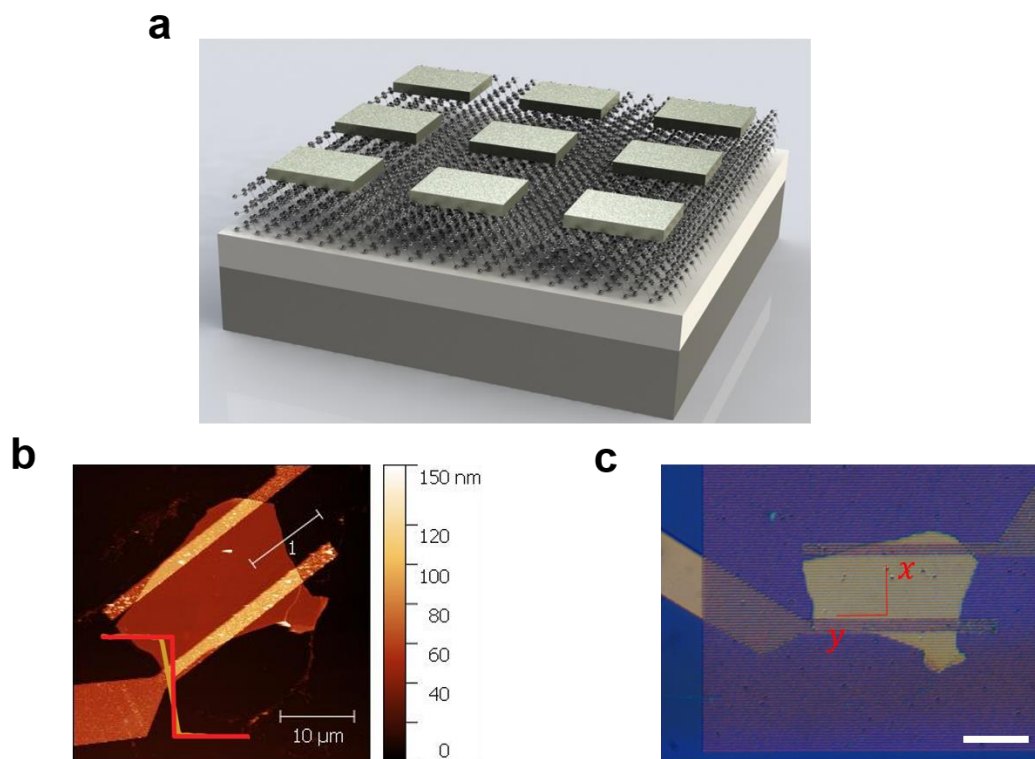
Figure 2.6.1. (a) Schematic of periodically patterned rectangular silver patches on BP. (b) AFM image of the BP flake with the height profile for trace 1 shown in the inset. The thickness of the flake is 38 nm. (c) Optical image after nanostructures patterning with the denoted crystal orientation. The shaded area on top of the device denotes the silver plasmonic array. The scale bar is 10 μm.

Towards this end, we used rectangular plasmonic silver nanopatch arrays (Figure 2.6.1(a)) as an extrinsically anisotropic resonator element. Silver rectangular nanopatches with lengths of 270 nm in the x direction and 200 nm in the y direction were arranged periodically with the same periodicity as before (i.e., 420 nm). The exfoliated BP flake used in this case is 38 nm thick as characterized with AFM (Figure 2.6.1(b)). We measured

the reflection spectra of the BP flake with different incident light polarization angles to determine the crystal orientation, which is denoted in the optical image in Figure 2.6.1(c). During the nanofabrication process, we aligned the silver rectangles to line up with the desired x and y crystal directions as designed in electromagnetic simulations. Figure 2.6.2(a) and 2.6.2(b) plot the calculated absorption inside the 38 nm thick BP flake before and after the nanofabrication of silver rectangles, respectively. The LSPR along the x direction (a = 270 nm) resides at ~620 nm. However, since the length of the silver antenna along the y direction is shorter (b = 200 nm), the resonance peak is blue-shifted to shorter wavelengths as expected. Due to different LSPR with respect to incident polarization, we observe an anisotropic absorption enhancement, where the absorption is enhanced for incident light polarized parallel to the x (intrinsically strongly absorbing) direction due to the excitation of the LSPR, but minimal enhancement is observed for polarization along the y (intrinsically weakly absorbing) direction. We also measured the photoresponse with the results plotted in Figure 2.6.2(c) along with the SEM image of the silver patches shown in the inset. The photoresponse for the zigzag direction is unchanged, whereas it is enhanced for the armchair direction in the presence of the silver rectangular nanopatch resonators, leading to a broad resonance peak at ~650 nm with ~1.5-fold enhancement. We note that the absorption and photocurrent response is already small for BP flakes along the zigzag direction, which implies that even a minor electrical field enhancement will lead to a photoresponse. This explains why we observe certain enhancement for the zigzag direction at ~550 nm, which corresponds to the LSPR wavelength for b = 200 nm length silver antennas.
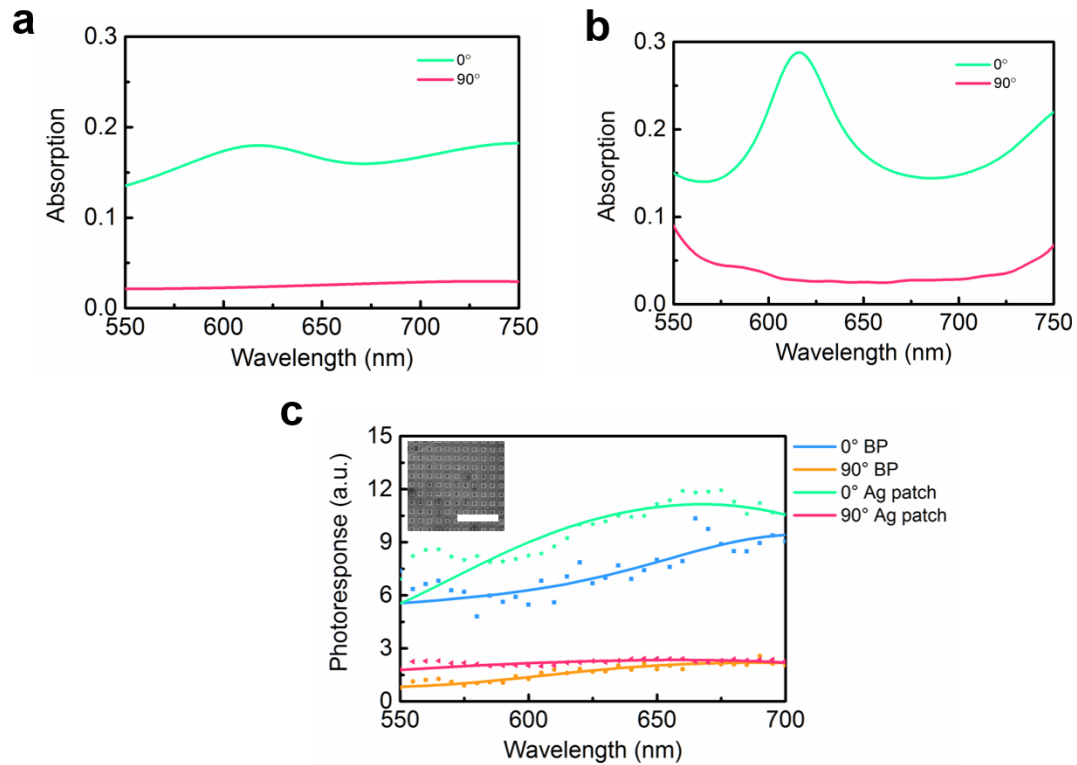
Figure 2.6.2. (a, b) Calculated absorption for BP alone and the hybrid BP/plasmonic array structure. (c) Measured photoresponse comparison for BP alone and the hybrid BP/plasmonic array structure. Dots and the lines are referred to the raw measurements and the fitted lines. The SEM image of the silver patches is provided in the inset. The scale bar is 2 μm.

2.7. Chapter summary

In conclusion, in this chapter we cover two cases for the amplitude control with BP by controlling the incident light polarization.

In the first case, we propose and numerically demonstrate localized surface plasmons modes in monolayer BP using nanoribbon and nanopatch arrays. Anisotropic behavior in the absorption spectra are predicted when exciting BP plasmons along two different directions (armchair and zigzag). Various structure parameters are examined to analyze the

material properties and the localized nature. Furthermore, we find that the electric field is mostly localized around the edges of the structure. It is possible to design a symmetric metasurface with BP and fulfill the polarization conversion due to the anisotropic absorption. And BP could also be used to build a polarization sensor at IR wavelengths even with symmetrical structures.

In the second case, we have demonstrated for the first time the coupling of an anisotropic plasmonic array aligned to an anisotropic semiconductor to increase optical absorption and photoresponse. Indeed, this is also the first plasmonic resonators on BP, enabling the polarization-controlled optical anisotropy in the visible wavelengths. Periodic silver nanodisk arrays were utilized to facilitate LSPRs and enhance light-matter interaction in BP for both crystal orientations. Furthermore, by coupling the intrinsically anisotropic optical properties of BP with an extrinsically anisotropic plasmonic lattice, we achieved the enhancement of the BP photoresponse along only the armchair direction, further improving the optical anisotropy about 50% more. Since BP also has anisotropic properties in the near IR, our work will provide the concepts and the guidelines to fulfill similar polarization-controlled performances with IR resonators. And similarly, the concepts presented here should prove useful when coupling plasmonic nanostructures with other, less well understood anisotropic 2D materials. We believe the hybrid devices consisting of plasmonic nanostructures that exhibit strong optical resonances with BP will enable high-performance polarization-dependent and anisotropic photodetection, as well as radiative and thermal emission in the future.

CHAPTER 3

Spatial phase control for tunable metasurfaces

3.1. DNA-mediated nanoparticle assembly

The spatial phase control of the wavevector in the flatland is majorly controlled with the generalized Snell's law as described in Chapter 1. Metasurfaces are majorly fabricated with building blocks in naoscales with precise and controlled positioning[9, 13], which is the key part to introduce the abrupt wave vector change at the interface to form the desired phase gradient.

Traditional method usually uses electron beam lithography and deposition to generate patterns. However, to get deep subwavelength structures, high energy electron beam is needed to obtain desired precision. Moreover, most of the structures cannot be changed after the fabrication. For applications requiring active control, there is barely space to play with to change the structure.

In this section, a novel patterning method developed by our collaborator will be introduced. By combining top-down lithographic patterning with bottom-up assembly, it is possible to generate highly precise nanostructures through DNA-mediated interactions in lithographically defined templates[63]. The nanoparticles and the substrate are functionalized with DNA and hybridized with complementary linkers so that they could be connected, as shown in Figure 3.1.1(a). The process starts with the silicon substrate deposited with 100 nm gold. After coating PMMA and electron beam exposure with development, the nanoparticles are attached to the generated trenches. After removing the

PMMA, we could acquire the nanostructures. Figure 3.1.1(b) shows the typical process routine.
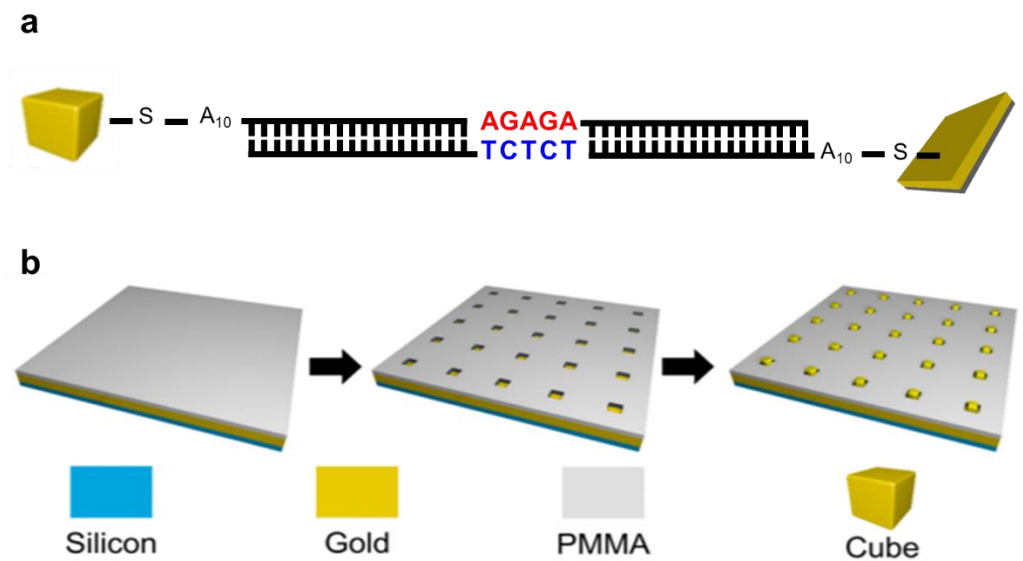
Figure 3.1.1. (a) Complementary linkers to connect the nanoparticles and the substrate. (b) Process combining top-down lithography and bottom-up assembly. The figures are adapted from the mentioned reference[63].

However, just with this kind of recipe is not enough since the assembled nanoparticles might randomly fall in the trenches. Thus, our collaborator also fulfills the orientation control by controlling the optical trench sizes. Figure 3.1.2 compares three different type of trenches. For circle trenches, no orientation control could be achieved. For non-optimal square trenches, the nanocubes will still randomly fall in the trenches with high yields to attach the nanocubes. But with carefully choosing the size of the trenches, the angular offset could be precisely controlled and the nanocubes will stay at the desired position.
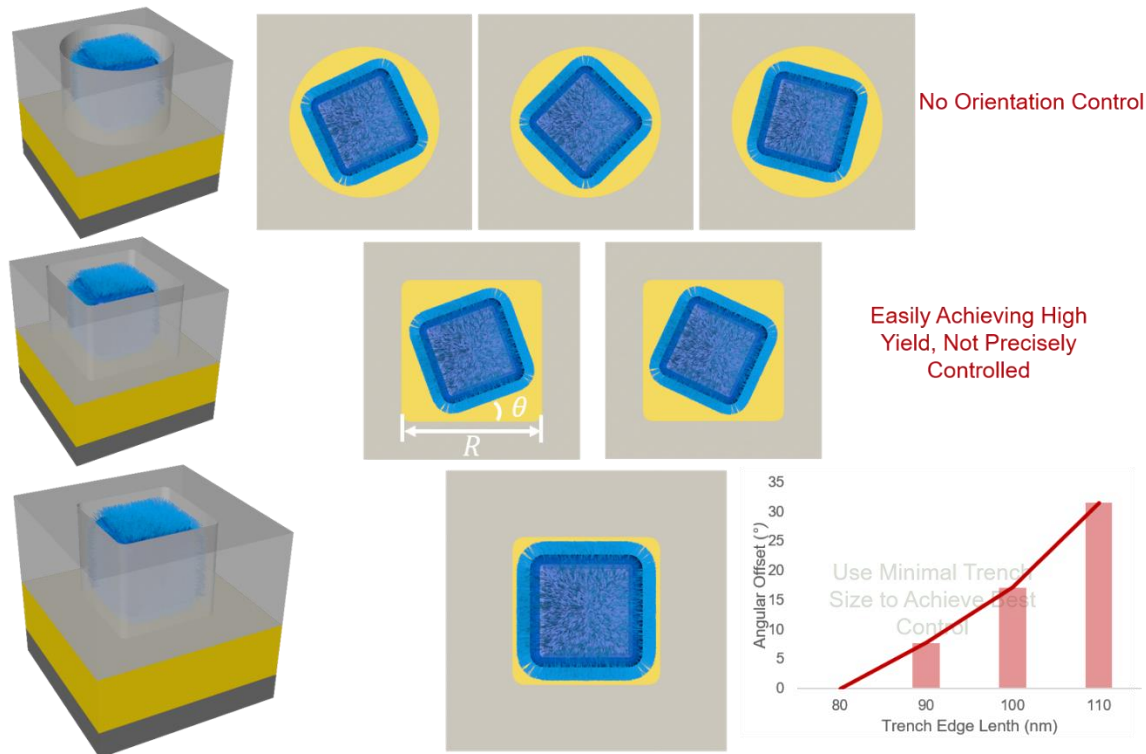
Figure 3.1.2. Orientation control performance with round trenches, large trenches and perfect trenches.

3.2. Tunable metasurfaces for light guiding

One particular advantage of using DNA in the patterning is that we could combine the DNA dynamics with the device designs to achieve a highly tailorable system that no other technique can generate. Specifically, as shown in Figure 3.2.1(a) and (b), due to the existence of DNA, there is a gap mode resonance could be excited other than the lattice mode and localized mode. The gap mode is quite dependent on the distance between the nanocube and the substrate, which indicates that if we could control the size of the DNA, we could potentially control the gap mode resonance as well.

One way to control the DNA length is using the ethonal (EtOH) to introduce the dielectric environment to tune the Column force around the DNA[64]. It has been shown that

by changing the environment EtOH concentration, the length of the DNA could be largely tuned, as shown in Figure 3.2.1(c). Typically, in this system with gold nanocubes, with 0% EtOH (water buffer), the length of the DNA is around 20 nm, while with 80% EtOH, the length of the DNA will contract to around 3 nm. As mentioned before, the gap mode is quite sensitive to the distance between the particles and the substrate. Figure 3.2.1(d) shows the measured reflection spectra with three different EtOH concentration. The resonance positions could be largely tuned from 650 nm to 775 nm.

To build the abrupt phase profile along the surface, we need to make use of the resonant elements to introduce large enough phase change. Thus, we usually design the structures to have the desired performance near the resonance. Here we would like to achieve anomalous reflection with the building blocks of gold nanocubes to work around 600 nm to 700 nm. This is the wavelength range just between two lowest resonance positions for 0% EtOH and 80% EtOH so that we could benefit from the gap mode resonances.
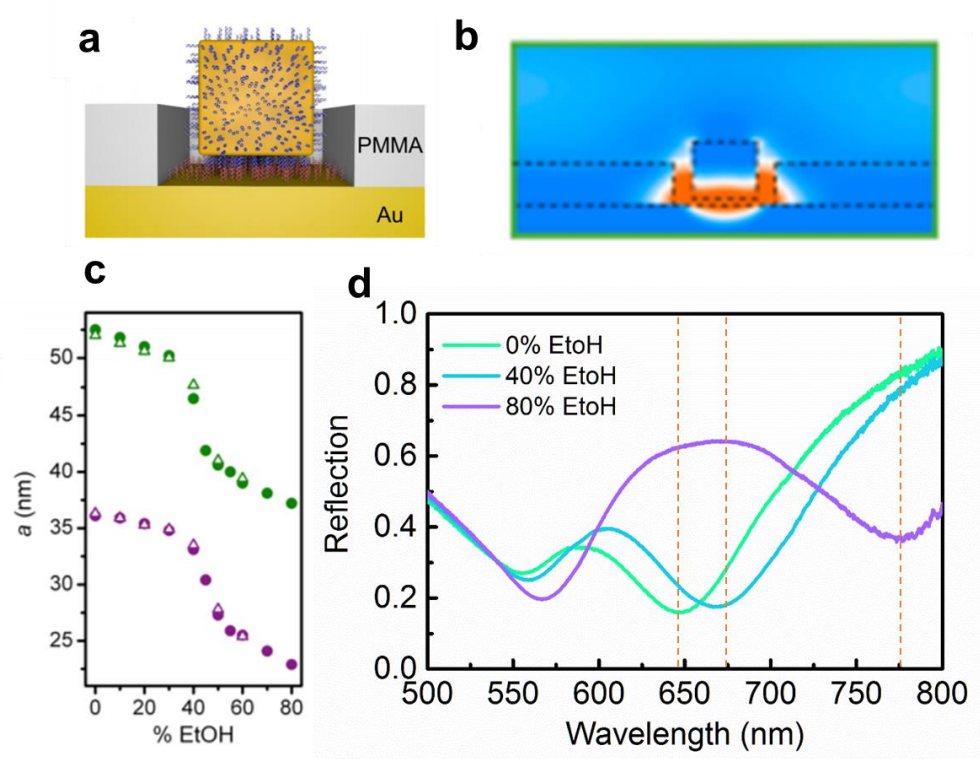
Figure 3.2.1. (a, b) Gap mode between the gold nanocube and the substrate. The figures are adapted from the mentioned reference[63]. (c) DNA length dependence of the EtOH concentration. The figures are adapted from the mentioned reference[64]. (d) Measured reflection spectra for the cubes with different EtOH concentration.

In Figure 3.2.2(a), I show the designed metasurface structures for anomalous absorption. The structure is composed of three different elements: one cube arrays, two cube arrays and three cube arrays. The corresponding reflective phases are shown in Figure 3.2.2(b). They could form the phase gradient along the space to achieve the metasurface light guiding. One thing to notice here is that the phase shift is just a proof of concept to indicate the phase shift. The calculated phase is based only on isolated element. The actual structure will also include the coupling between the elements. In Figure 3.2.2(c), we show the

scanning electron microscope (SEM) image for the fabricated metasurface. The yield of the structure is quite good.
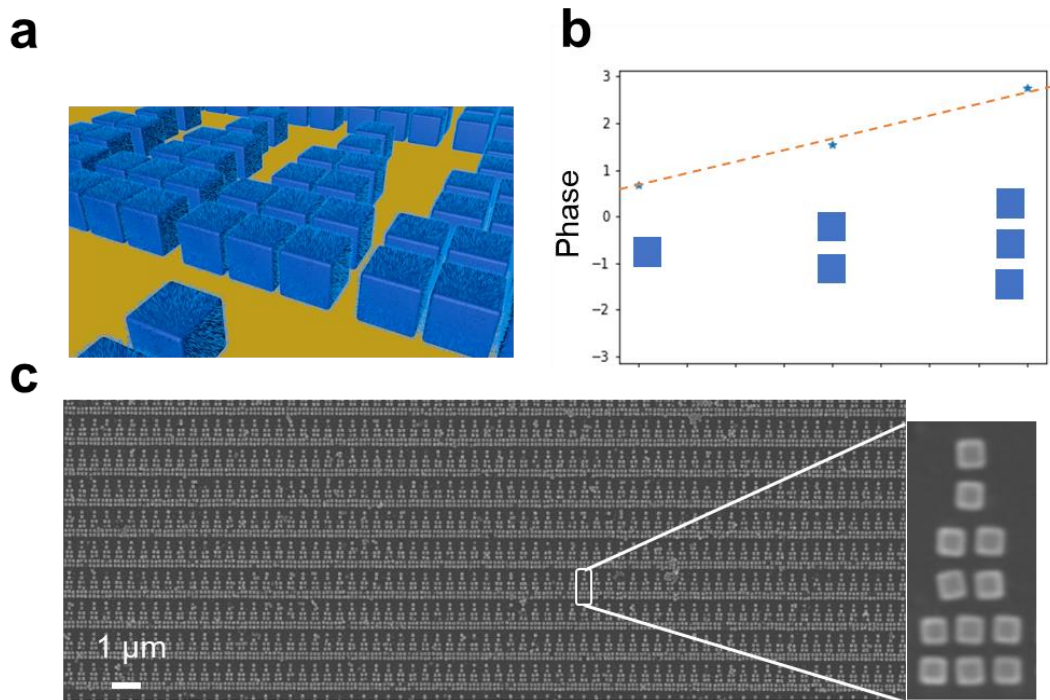
Figure 3.2.2. (a) Designed metasurfaces with gold nanocubes patterned with one cube arrays, two cube arrays and three cube arrays. (b) Calculated phase profile for three elements. (c) SEM image of the fabricated periodic structures.

To analyze the deflection, I calculated the far field power at various collection angles from -90° to 90°. Figure 3.2.3 show results of far field reflection power at different wavelengths. It could be seen that when the DNA length is 3 nm (Figure 3.2.3(a)), we achieve the anomalous reflection around -60° in a quite broad bandwidth from 610 nm to 690 nm. While for the DNA length of 20 nm (Figure 3.2.3(b)), most reflected power is reflected to 0°. More specifically, if we slice the result at 670 nm (Figure 3.2.3(c) and (d)). We could clearly compare the power in two scenarios.
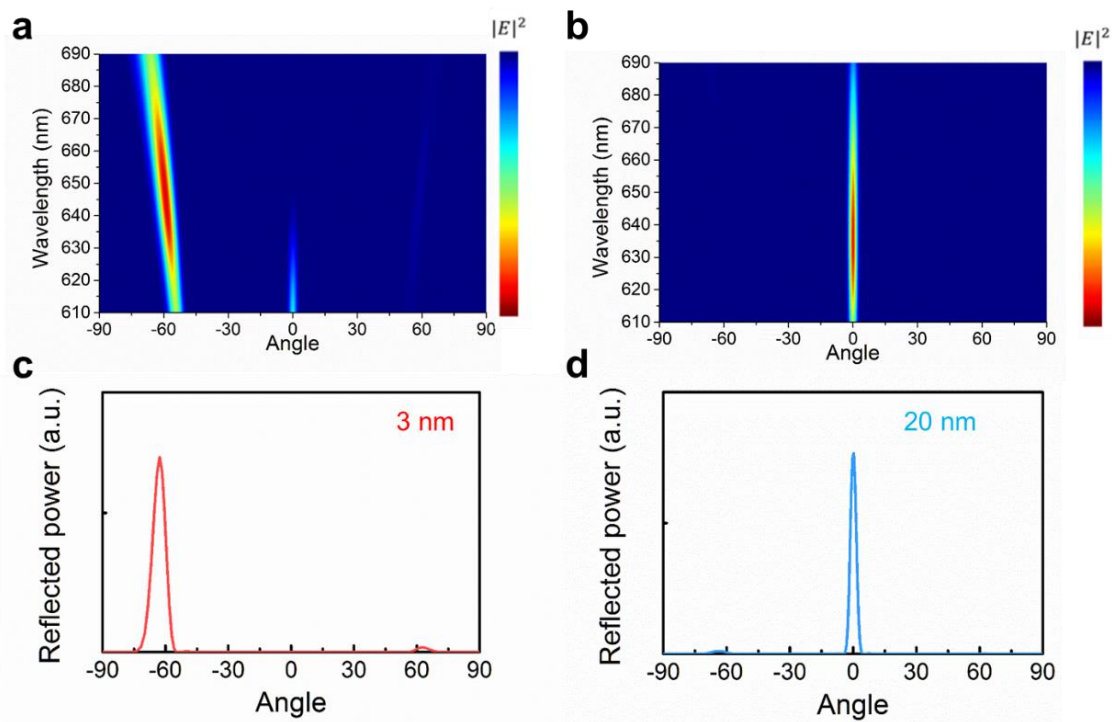
Figure 3.2.3. (a, b) Calculated reflected power for the wavelengths from 610 nm to 690 nm for 3 nm DNA length and 20 nm DNA length. (c, d) Calculated reflected power at 670 nm for 3 nm DNA length and 20 nm DNA length.

To better illustrate the idea, we calculate the electric field distribution near the around the structure at 670 nm. As shown in Figure 3.2.4, for 3 nm DNA length, the reflected power is guided to the anomalous angle while for 20 nm DNA length, the structure is acting like a mirror and most of power will be reflected at 0°. One thing to notice here is that the electric field power distribution is calculated in the near field. So, the angel shown in Figure 3.2.4 is not around 62°, which is the far field angle in Figure 3.2.4(c). This is because the refractive index near the structure is 1.36 for EtOH but the far field environment refractive index is 1.
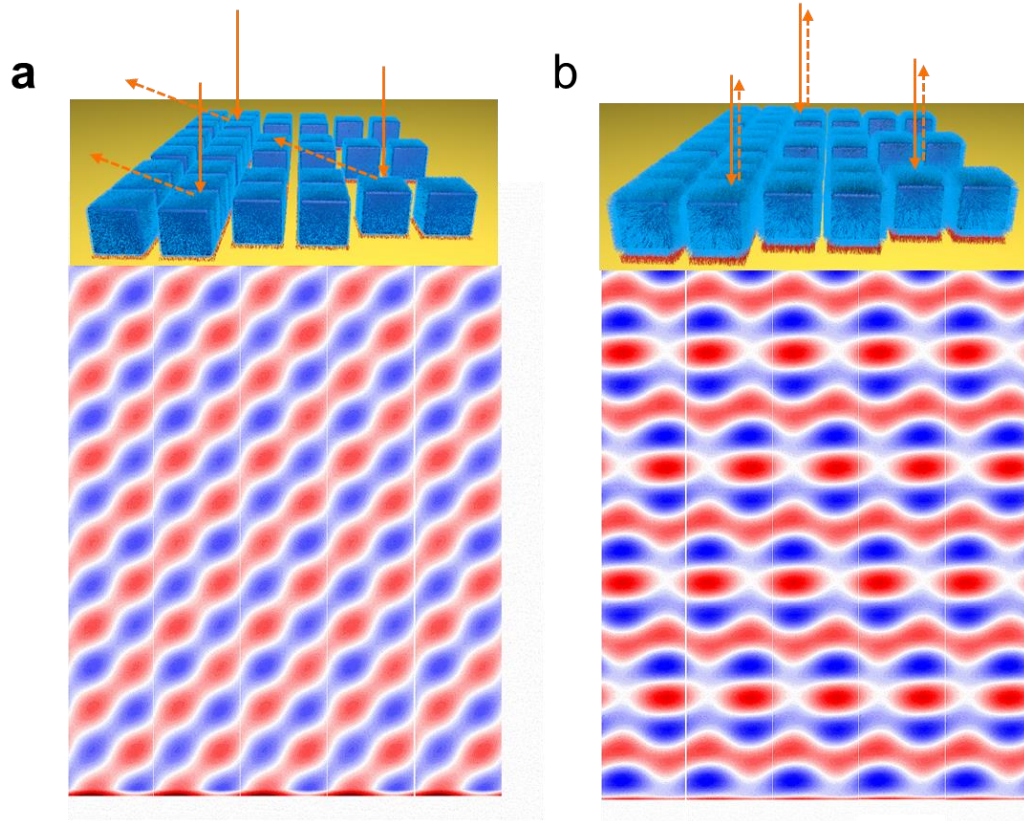
Figure 3.2.4. (a, b) Calculated electric field power distribution around the structure for 3 nm and 20 nm.

3.3. Experimental characterization with oblique incident light

To verify our proposed metasurface experimentally, we build the angle-resolved system with the incident collimated light and the rotation arm to detect reflected power at different collection degrees as shown in Figure 3.3.1(a). The sample is imbedded in the imaging chamber (Figure 3.3.1(b)) so that we could change the EtOH concentration around the sample at will. Here I took the pictures with the incident light coming directly at 0°. In Figure 3.3.1(c), we could observe that most of the light was directed to the left part. When I rotated the sample, the light was guided to the right side (Figure 3.3.1(d)).
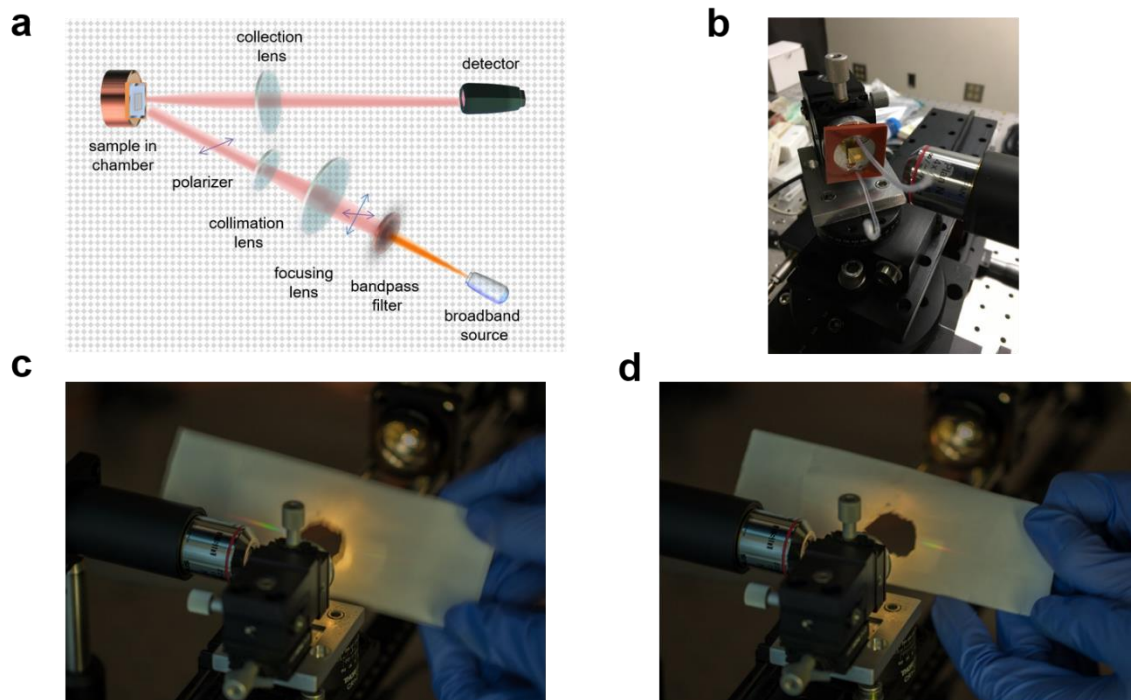
Figure 3.3.1. (a) Experimental setup with the angle-resolved system. (b) The imaging chamber including the sample for the tunable environment for different EtOH concentration. (c, d) Pictures of the 0° incident light with anomalous reflection while rotating the sample.

However, in this scenario, we couldn't directly compare the power at the anomalous angle and the normal angle since it is not possible to rotate the arm to detect the power at the same direction of the incident light. To compare the anomalous power and the normal power, we determine to have the incident light at an angle. Then the normal power will be guided to the other side with the same reflection angel. But the anomalous power will be guided to certain angle in between.

Specifically, since we shoot for the tunability at 670 nm, the incident angle is set at 62°. We recalculate the far field power similar to Figure 3.2.2 at this scenario. As shown in Figure 3.3.2, with 3 nm DNA length, most of the power is guided to the angle near 0°. And

for large DNA length at 20 nm, the light is reflected to 62°, just like a mirror following the reflection law. Similarly, we slice the reflected power at 670 nm. We could easily identify the dominant anomalous power at 3 nm and the dominant normal power.
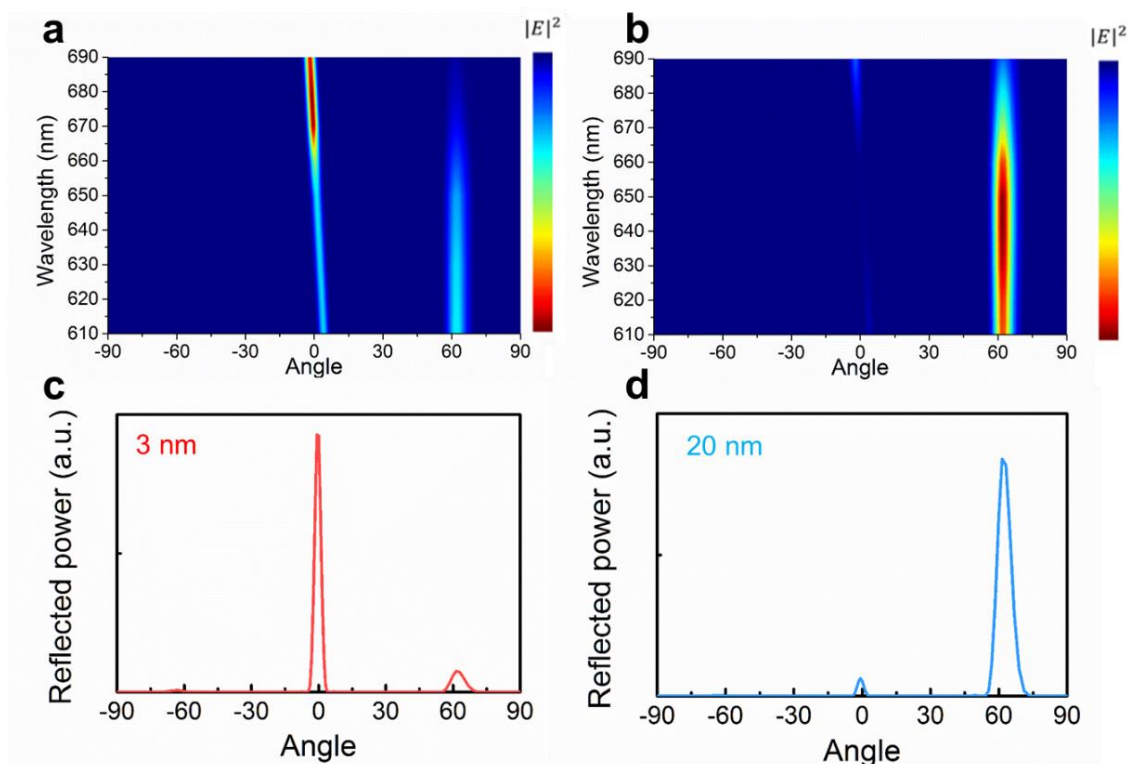
Figure 3.3.2. (a, b) Calculated reflected power for the wavelengths from 610 nm to 690 nm for 3 nm DNA length and 20 nm DNA length. (c, d) Calculated reflected power at 670 nm for 3 nm DNA length and 20 nm DNA length.

In Figure 3.3.3, we present the measurement results with the exact same incident angle of 62°. We put five different wavelengths filters (610 nm, 635 nm, 650 nm, 670 nm, 690 nm) and measure the power around anomalous angle and normal angle. The power at other angles are at the same level of the environment noise. In both cases, we normalize the overall amplitude the reflected power from the gold substrate measured at the normal angle

(62°). Data points other than those five wavelengths are fitted in between. Figure 3.3.3(c) and (d) show the reflected power comparison at 670 nm. We could observe quite good agreement with the calculated results at Figure 3.3.2.
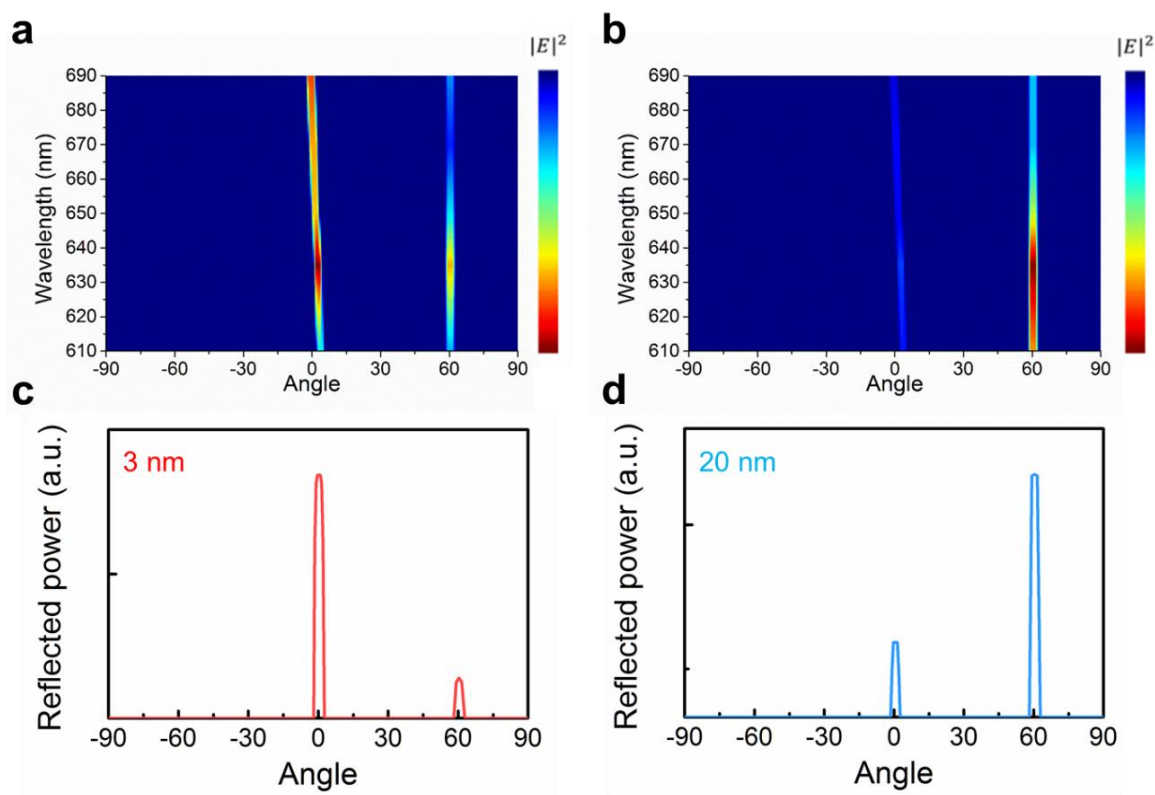
Figure 3.3.3. (a, b) Measured reflected power for the wavelengths from 610 nm to 690 nm for 3 nm DNA length and 20 nm DNA length. (c, d) Measured reflected power at 670 nm for 3 nm DNA length and 20 nm DNA length.

3.4. Chapter summary

In conclusion, we have demonstrated a tunable metasurface at visible wavelengths based on DNA dynamics. By changing the environmental EtOH concentration, the length of the DNA, thus the gap mode of the nanocubes could be actively controlled. We show both in

simulation and in experiment that with 80% EtOH, we could have small DNA length around 3 nm and the metasurface could work as an anomalous deflector. While with 0% EtOH, we will have large DNA length around 20 nm and the metasurface will work similar to a mirror. The electric field power distribution also verifies the idea of the tunability. We believe out platform provides both novel and unique tunable light guiding performance by utilizing the gap mode. With the emergence of the dielectric metasurfaces, the DNA-mediated platform could also be combined with the dielectric nanoparticles in the future for building metalenses. Our work here provides a proof of concept to fulfill the tunable metalenses. And due to the special properties of many available DNA properties, the platform will find more use with other mechanism in active applications.

CHAPTER 4

Temporal phase control for time-varying metasurfaces

4.1. Temporal modulation and optical isolator

As described before for the normal metasurfaces, resonant elements with different sizes and shapes are arranged together to enable a space-varying phase across the metasurface. Additional phase jump induced by metasurfaces relaxes the conservation of the tangential momentum, leading to anomalous reflection and transmission thus enabling new classes of optical devices. There is an additional possibility allowed by the Snell's law, which is to use a time-varying phase change rather than commonly used a space-varying phase-change[65]. By introducing a time-gradient phase discontinuity using a metasurface, it is possible to mimic a Doppler-like wavelength (energy) shift in optical devices. Time-varying phase-change breaks the Lorentz reciprocity enabling novel optical devices such as optical isolators without using nonlinear materials. The introduction of the temporal modulation can also couple larger amount of energy, which overcomes the geometric limitations of ultrathin metasurfaces.

One example of using time-varying metasurfaces to build the optical isolator is illustrated in Figure 4.1. Assume we obtain a time-varying metasurface that could increase the frequency of the incident light by $\Delta\omega$. When we combine the metasurface with two filters with ω and $\omega + \Delta\omega$, the first light path will be possible. But if we reverse the light path, the Lorentz reciprocity is not conserved and we actually obtain a optical isolator.
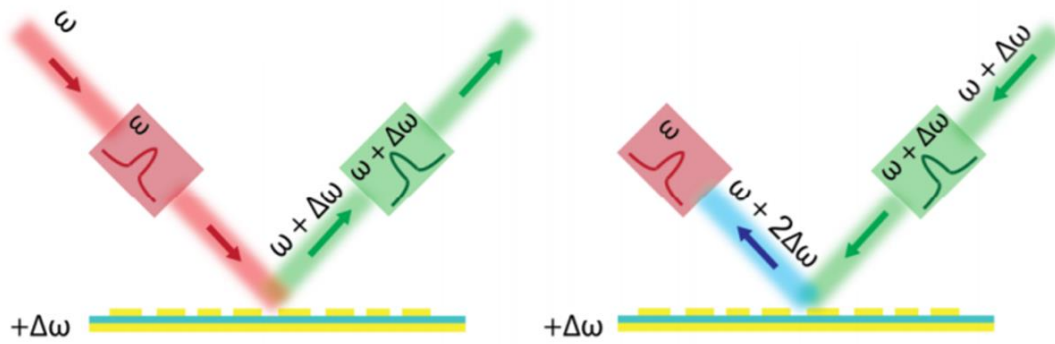
Figure 4.1. Time-varying metasurfaces with increased frequency for optical isolator[65].

4.2. Graphene microribbons with modulated Fermi levels

Although time-varying metasurfaces offer new ways to control light-matter interactions, it is rather challenging to realize time-varying metasurfaces especially at optical frequencies. In order to yield noticeable wavelength/frequency change at optical frequencies, phase needs to be controlled extremely fast (on the order of 500 THz) which is quite difficult to achieve with existing optical modulation techniques. On the other hand, it is rather straightforward to realize time-varying metasurfaces at microwave frequencies using varactors. Here, we theoretically propose a time-varying metasurface design based on graphene micro-ribbons that can be used to induce wavelength change for reflected waves at terahertz frequencies.

Graphene's optical conductivity therefore complex refractive coefficients can be tuned dynamically by changing its Fermi level via applied electrostatic potential[66]. FDTD simulations are performed to calculate phase-change through graphene micro-ribbon arrays for different Fermi levels. By adjusting the Fermi level of graphene with a specific temporal

modulation frequency, graphene micro-ribbon metasurface has been shown to reflect terahertz electromagnetic waves with either increased or decreased frequency when compared with the incident waves. Here, we demonstrate a simple yet an efficient time-varying metasurface design that will provide guidelines for experimental realization of such metasurfaces at terahertz frequencies and beyond. To understand the concept of time-varying metasurfaces, we will use a simple numerical analysis. As mentioned in Chapter 1, the frequency of the light could be determined by:

$$\omega = -\frac{\partial \phi}{\partial t}$$

Time-varying phase change, which can be introduced via temporal modulation, will change the frequency of reflected electromagnetic wave by $\Delta\omega = -\frac{\partial \Delta\phi}{\partial t}$. In order to realize time-varying metasurfaces, phase of reflected-wave needs to be modulated temporally such that $\frac{\partial \Delta\phi}{\partial t} \neq 0$.

Here, we propose to use graphene micro-ribbons whose Fermi level can be tuned by applying voltage. The optical conductivity, as mentioned before, as well as the complex refractive indices of graphene depends strongly on the Fermi level E_F. However, it is rather challenging to achieve large enough phase change using a continuous graphene film due to weak wave-matter interactions as a result of its monolayer thickness. We propose to use graphene micro-ribbon arrays rather than a continuous graphene film simply to enhance wave-matter interactions that yields relatively larger phase changes due to resonant behavior at certain frequencies. Graphene micro-ribbon arrays provide a unique platform to excite the localized surface plasmons at terahertz and infrared wavelengths. Our time-varying metasurface design is schematically shown in Figure 4.2.1, where graphene micro-

ribbon arrays are placed on top of a transparent spacer layer and a thick metal substrate. The ribbon width and the periodicity of graphene micro-ribbon arrays are chosen to be 25 μm and 50 μm. These structural parameters result from the optimization of the graphene micro-ribbon arrays after many electromagnetic simulations such that large-enough phase change can be achieved around the wavelength of 300 μm (around $f = 1$ THz) for different Fermi levels of graphene. The refractive index of the dielectric spacer (polyimide) is set to a constant value of $n = 1.7$. The dielectric layer thickness is optimized to be 10 μm to enhance the overall performance. The metal at the backside is assumed to be a perfect electric conductor (PEC) serving as a mirror to reflect waves back into the dielectric spacer. As we will illustrate later, the reflected waves will change the frequency due to the time-varying phase change from the metasurface.
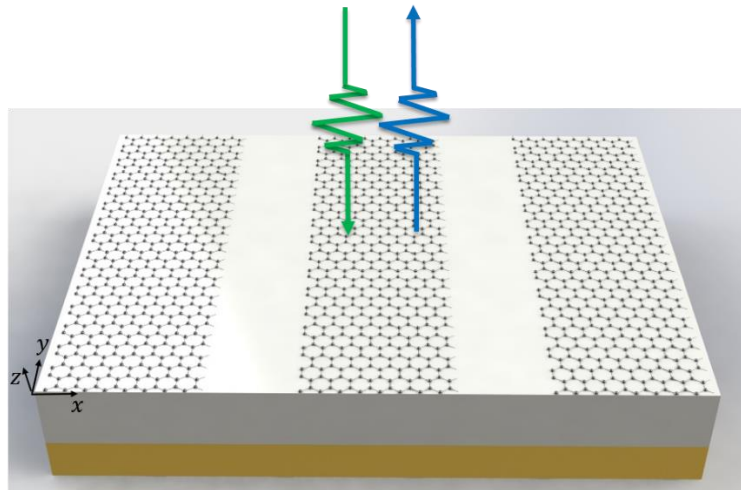
Figure 4.2.1. Schematic drawing of the graphene micro-ribbon array placed on top of a 10 μm thick dielectric spacer and a metallic mirror. Arrows with different colors are drawn to indicate the frequency change of the wave upon reflection.

Calculated reflection spectra of graphene micro-ribbon arrays for three different E_F values are plotted in Figure 4.2.2(a). For $E_F = 0.3$ eV, there exists a dip in the reflection spectra around 300 μm indicating a resonant behavior due to a localized electromagnetic response from micro-structured graphene. Increasing E_F from 0.3 eV to 0.9 eV results in a shift of the resonance wavelength towards shorter wavelengths. Figure 4.2.2(b) shows the side-view electric field distribution of the E_z for one ribbon at the wavelength of 300 μm and $E_F = 0.6$ eV. Localized resonant dipoles around the edges of the ribbon can be clearly seen in Figure 4.2.2(b).
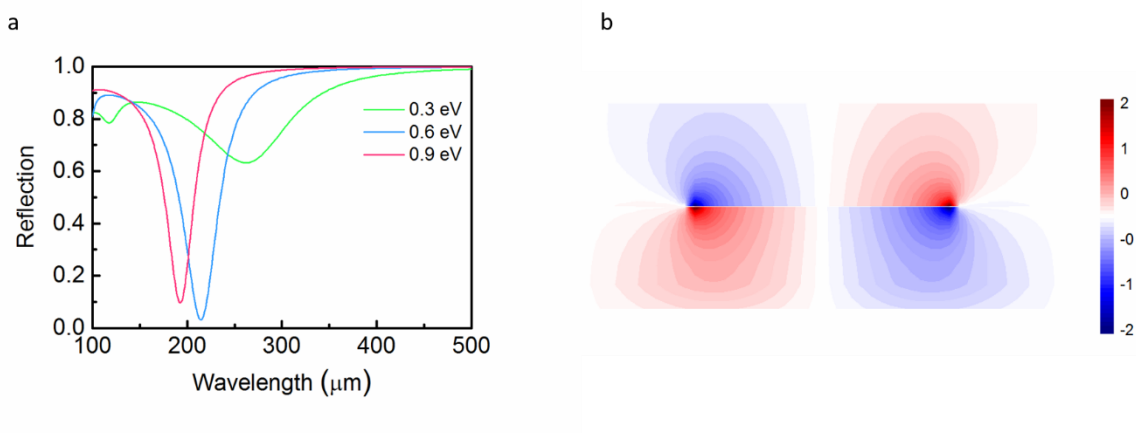
Figure 4.2.2. (a) Calculated reflection spectra of graphene micro-ribbon array metasurfaces for three different graphene Fermi energies. (b) Simulated electric-field distribution (E_z) for a single graphene micro-ribbon unit cell.

4.3. Figure of Merit for frequency change

Figure 4.3.1 plots phase changes at 5 different wavelengths as Fermi energy is changed from 0.1 eV to 1 eV with 0.1 eV step size. In order to achieve highest increase in the frequency of terahertz waves, metasurface should be operated at frequencies where largest

phase change occurs (typically around the resonance frequency). However, reflection will be significantly lower and waves will be mostly absorbed by the ultrathin graphene metasurface due to resonant behavior. A better approach is to slightly deviate the operation frequency away from the resonance frequency such that there is still moderate phase change with suitable reflection from the graphene metasurface.

Time-varying metasurface enabling a frequency change in reflected terahertz waves can be obtained by changing the Fermi level, therefore the complex refractive indices of graphene as a function time. In Figure 4.3.2(a) we plot a temporal modulation pattern for changing the Fermi level of graphene. In this case, the derivative of Fermi level is negative in every period. In order to understand the operation principle and key parameters such as the frequency change, we are going to utilize a simple analytical formula and make certain assumptions. When terahertz waves with a wavelength of 200 µm ($f = 1.5$ THz) are incident on the graphene metasurface, overall phase change is calculated to be $\Delta\phi \sim 5$ (Figure 4.3.1) for Fermi Levels changing from 0.1 eV to 1 eV. Assume Fermi levels are modulated by $\Delta t \sim 10^{-9}$s, which requires 1 GHz alternative current (AC) to be applied on the graphene (Figure 4.3.2(a)). For such a scenario, the frequency change is $\Delta\omega \sim -\frac{\Delta\phi}{\Delta t} = 5$ GHz with a quality factor of $\frac{\Delta\omega}{\omega} = 0.021$. Here, we choose a moderate temporal modulation frequency for realistic applications, however faster modulation speeds that might be achieved in the future will induce larger frequency change, since the frequency change is proportional to the modulation frequency. As mentioned earlier one of the significant drawbacks for operation around resonance frequency is low reflection from the metasurface. For this particular wavelength of 200 µm, reflection is almost zero for a Fermi

level of 0.6 eV (Figure 4.2.2(a)), where largest phase jump occurs (Figure 4.3.1). Let us consider a different scenario in which the operation frequency is chosen to be away from the resonance frequency resulting in a smaller phase change but better reflection performance. For terahertz waves with a wavelength of 300 μm, Fermi level change from 0.4 eV to 1 eV leads to a decrease in $\Delta\phi = 0.03$. Here, we only consider the Fermi level range between 0.4 eV to 1.0 eV, since in this range the phase change is monotonously decreasing. One could also choose the Fermi level range of 0.2 eV to 0.4 eV where phase change is increasing with increased Fermi level. However, in order to compare our results with previously discussed wavelengths, we decided to focus only on the region where we observe a similar behavior of reduced phase change. Still assuming the same temporal modulation pattern with 1 GHz AC frequency, we obtain $\Delta\omega \sim -\frac{\Delta\phi}{\Delta t} = 3 \times 10^{-2}$ GHz and the quality factor is about 1.9×10^{-4}. It is expected that due to smaller phase change, the frequency change is also smaller. However, it is worthy of note that even such frequency change is quite fascinating, which is hardly achievable with traditional optical devices. And in this case, the overall reflection is always above 70% as can be seen from Figure 4.2.2(a).
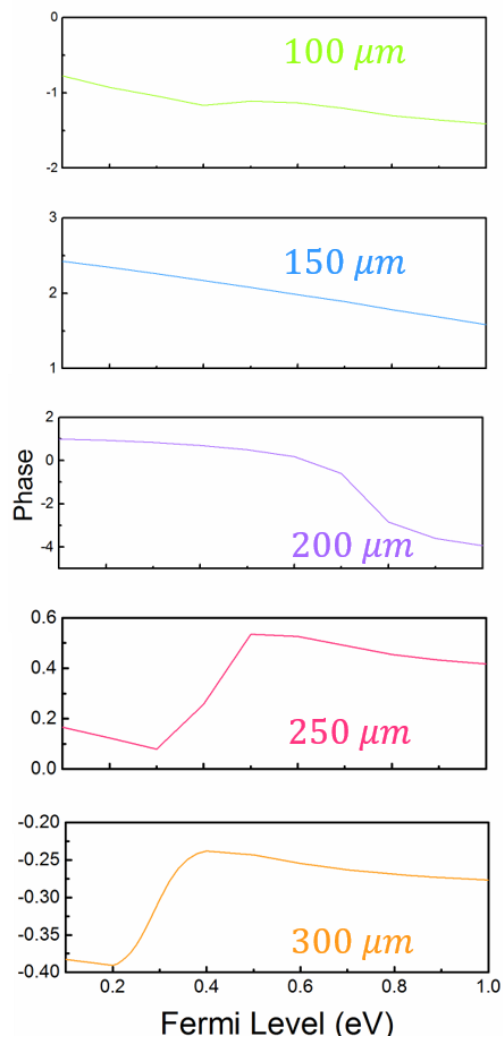
Figure 4.3.1. Simulated phase change enabled by graphene micro-ribbon metasurface at different wavelengths for different Fermi levels tuned from 0.1 eV to 1.0 eV with 0.1 eV steps. Note that the phase change scales for each plot are different to better illustrate the phase change trend. Highest phase change occurs at 200 μm where reflection is minimum for 0.6 eV Fermi level.

The frequency change of the reflected wave is an important parameter and we choose it to be a figure of merit (FOM) to compare the performance of our graphene based time-varying metasurfaces for different operation wavelengths. In Figure 4.3.2(b), we plot the

frequency change as a function of the operation wavelength, assuming 1 GHz AC current is applied to change the Fermi Level of graphene. For wavelengths longer than 200 μm, the frequency change is calculated by the phase difference of the monotonously decreasing region as discussed in the case of 300 μm. As one can see from Figure 4.3.2(b), the largest frequency change occurs around 200 μm, where the reflection is calculated to be almost zero for a Fermi level of 0.6 eV, indicating a strong resonance.
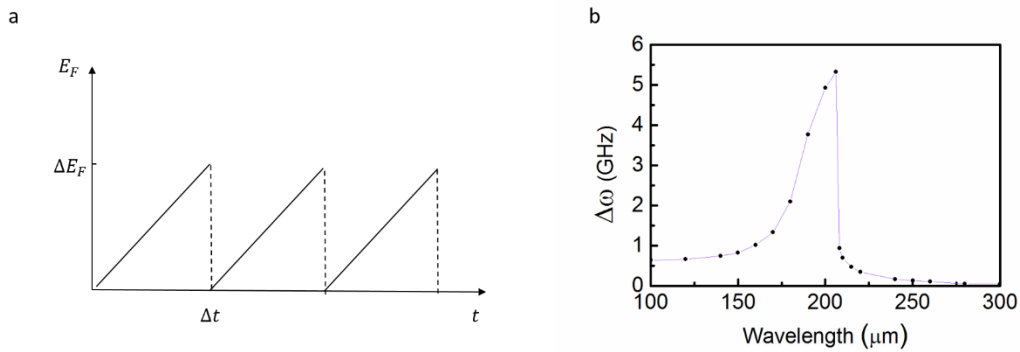
Figure 4.3.2. (a) Proposed temporal modulation pattern for changing the Fermi levels of graphene. (b) Calculated frequency change of reflected terahertz waves for different operation wavelengths of time-varying metasurface.

Compared with space-varying metasurfaces, 2π phase change for one designed element is not required for time-varying metasurfaces. In the previous case, the phase modulation enabled by spatial distribution of varying sizes of resonators is passive and the device needs to cover almost 2π phase change to accumulate the overall gradient as well as the additional wavevectors. In time-varying metasurfaces, since the modulation is controlled actively, the restriction is no longer an essential design guideline but a preferred one. With larger phase change approaching 2π, it is easier to obtain higher quality factor.

4.4. Chapter summary

In conclusion, we propose and theoretically demonstrate a graphene micro-ribbon array-based time-varying metasurface providing a novel platform to modulate the electromagnetic wave frequency in ultra-thin devices. The graphene micro-ribbon arrays are able to work on different frequency regions and fulfill various aims for optical performances. Compared with space-varying metasurfaces, the time-varying metasurfaces offer the opportunities to control the light in a more active manner. It is possible to combine both space-gradient patterns and temporal modulation at the same time to build more complicated devices, such as multifunctional anomalous deflectors and optical isolators. We believe our design will pave the way towards novel metasurface designs and enable mimicking the Doppler-like phenomenon in future optical devices.

CHAPTER 5

Further spectra engineering with active controllable materials

5.1. Applications with active controllable materials

In this Chapter, I will cover two more spectra engineering topics, which includes the excitation of the graphene surface plasmons and the control of dynamic properties of vanadium dioxide (VO_2). Both materials have active controllable properties. Specifically, I will focus the applications for the enhanced transmission and the dynamic absorption.

Enhanced transmission of light using nanostructured metals has always been of great interest in the field of plasmonics[67]. With the aid of near-field effects, the transmission of the electromagnetic waves can be enhanced or depressed. Extraordinary light transmission through single sub-wavelength apertures nanohole arrays have been studied thoroughly. With similar motivations, electromagnetic transmission through a metal film with the mediation of surface plasmons has also been proposed. Much of the work on enhanced transmission has been shown to be frequency-selective due to size-dependent optical resonance frequencies. And we would like to show a counter-intuitive model to increase the mid-infrared (mid-IR) transmission over a broad range of frequencies by using an absorptive, continuous graphene film, which has shown broadband properties in many applications.

The other application to be covered in this Chapter is the dynamic absorber with thin film light interference. Resonant light absorption has been investigated extensively in recent years with various materials and different resonance mechanisms. Conventional approach is to enhance the absorption by structuring either the absorbing material or using

resonant elements such as optical antennas to enhance the local electromagnetic field inside the absorbing media[68-71]. Alternatively, planar devices composed of thin-film materials have been recently investigated as an optical absorber platform[72-75], that are used for applications such as modulators[76-77], photodetectors[78-79], and thermal emitters[80-82]. Most of these planar lithography-free devices rely on the interference of the reflected light with the incident light to enhance the absorption. In particular, multilayer thin films with Fabry-Perot resonance response have been investigated thoroughly[80, 83-84]. However, those platforms require at least wavelength-scale dielectric cavities to form the resonances, making the whole devices quite thick. Thus, it is favorable to design a platform, which could mimic the resonant behavior of the lithography cavity while still remains compact as the devices incorporating nanostructures. One possible solution is to use highly absorbing materials, which could drastically decrease the thickness to fulfill the effective interference. And VO_2 is great candidate for the job.

5.2. Enhanced transmission control by exciting graphene surface plasmons

First, let us see how we could demonstrate enhanced infrared transmission through gold nanoslit arrays. The performance is achieved at mid-IR frequency range via excitation of surface plasmon polaritons (SPPs) at the graphene/metal interface. We theoretically demonstrate that with the excitation of the SPPs in continuous graphene, mid-IR radiation transmitted through nanoslit arrays with narrow slit widths can be enhanced over broad range of frequencies. This type of hybrid structure offers new opportunities for the study and the control of propagating SPPs in a continuous graphene sheet.

Metallic slit arrays or so-called wire grid structures are widely used as optical polarizers especially in the infrared spectral range. A wire grid polarizer is composed of a grid of metallic strips with the periodicity much smaller than the wavelength of the radiation. For p-polarized light, that is, when the magnetic field is parallel to the metallic strips, it can travel through the slits while s-polarized light will be reflected back. When using narrow slit width between the metallic strips, the light transmission is also quite poor for p-polarized light. Here, we propose to enhance the mid-IR transmission from the gold nanoslit arrays by coupling with graphene SPPs.

In the mid-IR wavelength range, the optical properties of doped or gated graphene will be dominated by optical intraband transitions, instead of interband transition and phonon-induced scattering. In this case, the optical response of the graphene can be modeled with a semiclassical Drude-like expression[25]:

$$\sigma(\omega) = \frac{e^2 E_F}{\pi \hbar^2} \frac{i}{\omega + i\tau^{-1}}$$

and the plasmon dispersion relation reads:

$$q(\omega) = \frac{\pi \hbar^2 \epsilon_0 (\epsilon_{r1} + \epsilon_{r2})}{e^2 E_F} \left(1 + \frac{i}{\tau \omega}\right) \omega^2$$

where $q(\omega)$ is the wave vector in graphene, ϵ_{r1} and ϵ_{r2} are relative permittivity surrounding the graphene sheet, E_F is the Fermi level and τ is the relaxation time. In our simulations, we optimize and choose the Fermi level to be at 0.3 eV, which maximizes the performance in the wavelength region of interest. The relaxation time τ is connected with the mobility µ as well as the Fermi-level: $\tau = \frac{\mu E_F}{e\, v_F^2}$ and v_F is the well-known Fermi velocity (10^6 m/s). The mobility in the simulation is chosen to be 10000 cm^2/Vs.

The optical gratings are commonly used to excite surface plasmons[85]. Here, the gold nanoslit arrays provide an ideal frame to compensate the momentum mismatch to excite the surface plasmons in graphene. As shown in Figure 5.2.1(a), continuous graphene is placed underneath the gold grating with silicon as the substrate, which could be fulfilled in experiment by transferring graphene film on silicon followed by patterning gold nanoslit arrays. The silicon is used as the transparent substrate in the wavelengths of interest. The p-polarized EM wave is normally incident in all the simulations. We use FDTD technique to simulate the optical response of the graphene/gold nanoslit arrays which has 500 nm periodicity and 20 nm slit width. The thickness of the gold is chosen to be 50 nm and the graphene is modeled as an anisotropic material with 1 nm thickness. The transmission spectra of gold nanoslit arrays without and with graphene are plotted in Figure 5.2.1(b). For the gold nanoslit array case, the transmission of the radiation covers the mid-IR region broadly with 20% to 40% due to the polarizer effect with small slit width between the gold strips. After placing graphene underneath the gold grating in the simulations, we observe a broad transmission enhancement up to 40% to 60%, which is quite surprising since graphene is just a monolayer and lossy material. The physical mechanism for this enhanced transmission will be discussed later.

The transmission enhancement is strongly dependent on the structure parameters, i.e. the periodicity and the slit width. To figure out the effect of these parameters, the transmission spectra with different periodicities and slit widths are simulated for two cases: without graphene and with graphene.
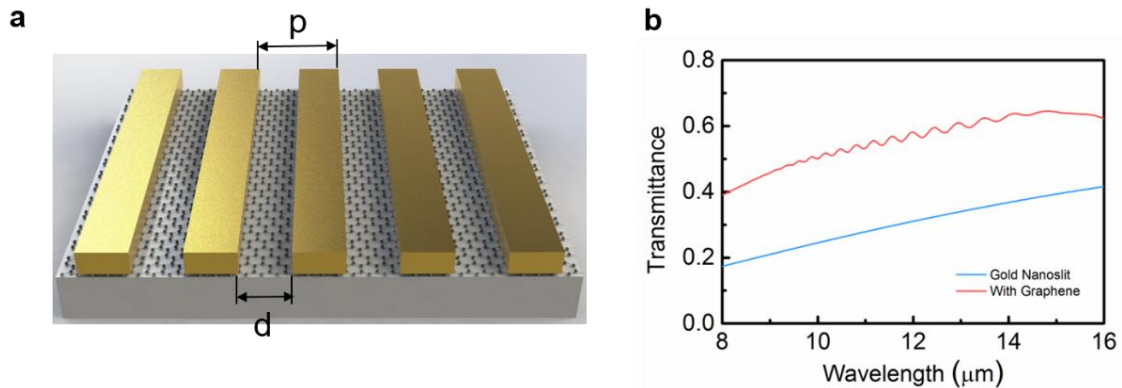
Figure 5.2.1 (a) Schematics of continuous graphene film at the bottom of the gold nanoslit arrays. (b) Transmittance of the structures of gold nanoslit arrays with and without graphene for periodicity p = 500 nm and d = 20 nm.

The transmission spectra shown in Figure 5.2.2 were obtained by changing the periodicity from 200 nm to 1000 nm and keeping the slit width fixed at 20 nm. As shown in Figure 5.2.2(a), when there is no graphene, the transmission increases with decreasing periodicity and larger transmission happens at longer wavelengths. When the periodicity is extremely small compared with the wavelength, the gold nanoslit structure can be described with an effective index model which indicates the flat transmission spectra[86]. After combining with graphene, we observe that the transmission is enhanced for the entire spectrum, especially for larger periodicities at longer wavelengths, as shown in Figure 5.2.2(b). The transmission spectra of several periodicities are selected and plotted separately in Figure 5.2.2(c) for comparison. There are oscillations in the transmission spectrum due to Fabry-Perot type reflection of the graphene surface plasmons from the nanoslit period boundaries. Increasing the periodicity will induce higher order reflections and thus increase the number of oscillations. The enhancement ratio is obtained by dividing

the transmission with graphene to that without graphene (ER $= \frac{T_{Graphene}}{T_{Gold}}$), as plotted in

Figure 5.2.2(d). Since we are keeping the slit width fixed at 20 nm while increasing the

periodicity, the transmission reduces significantly in the case of gold nanoslit arrays.

Therefore, it is easier to enhance transmission with larger periodicity, hence larger

enhancement factors.
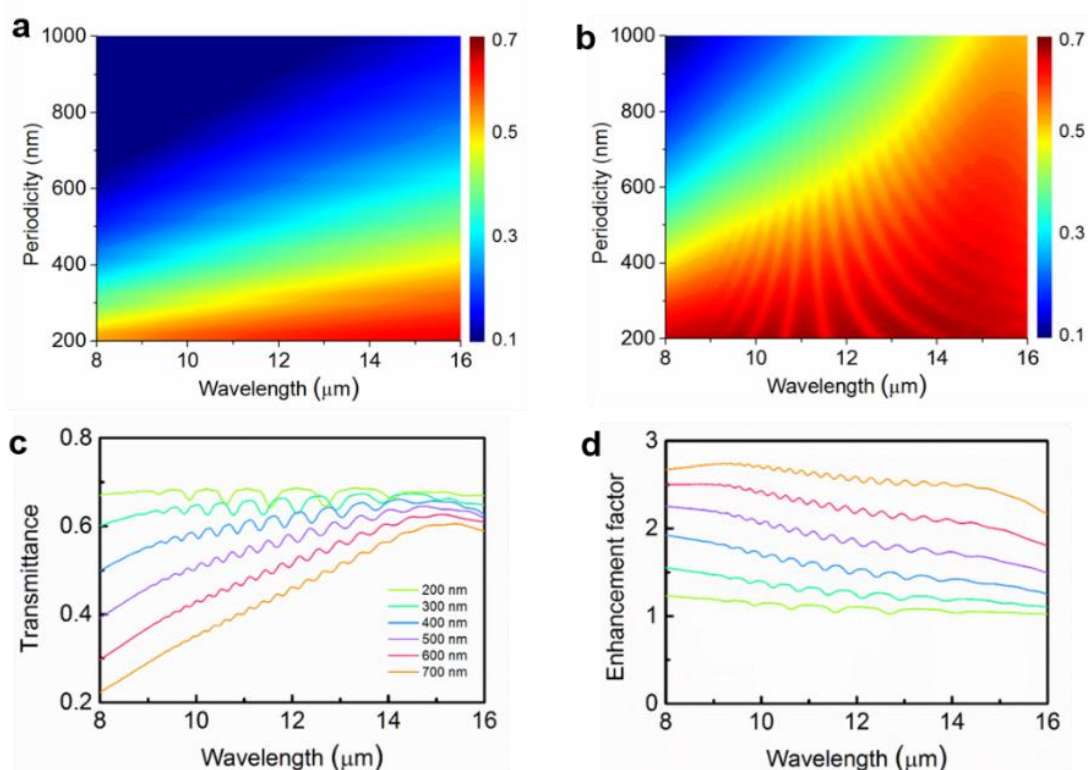
Figure 5.2.2 (a) and (b) Transmittance spectrum of gold nanoslit arrays without and with graphene for different periodicities (fixed slit width 20 nm). (c) Transmittance of selected periodicities of the structures with graphene at the bottom. (d) Enhancement factor $\left(EF = \frac{T_{Graphene}}{T_{Gold}} \right)$ for selected periodicities compared by two cases.

Additional simulations are performed by keeping the periodicity fixed at 500 nm and

changing the slit width. Simulated transmission spectra for varying slit widths from 0 nm

(continuous gold) to 100 nm are shown in Figure 5.2.3(a) and 5.2.3(b). The transmission is rather low for slit widths smaller than 20 nm. Increasing the slit width results in higher transmission. Similar to the periodicity effect, larger transmission also happens at longer wavelengths. After combining with graphene, we observe how the oscillations perform with varied slit widths. When the slit widths are larger than 40 nm, the transmission dips can be observed. And the dips move to higher wavelengths for wider slit widths, which indicates the localized features of the graphene surface plasmons in the slits.

The spectra of several slit widths as well as the corresponding enhancement ratios are plotted in Figure 5.2.3(c) and 5.2.3(d). The enhancement is getting larger with smaller slit widths which resembles the performance of the case with large periodicities when considering in terms of the duty cycles. Actually the enhancement ratio can be quite large when the slit width is about 10 nm in simulations. In the case of small slit widths, the transmission without graphene is approaching zero with large portion of reflective gold in one period. And the transmission dips shift to longer wavelengths when the slit widths get wider, which is the typical trend in localized surface plasmons. For 100 nm slit width case, higher order resonance can also be observed in this wavelength region.
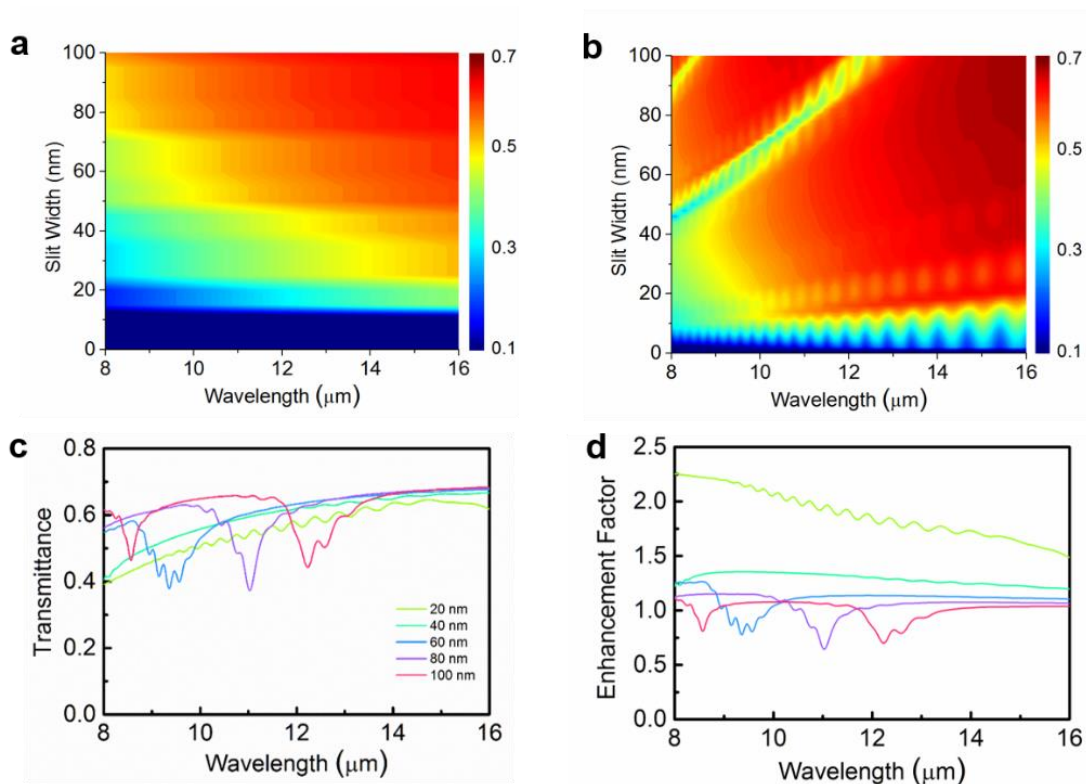
Figure 5.2.3 (a) and (b) Transmittance spectrum of gold nanoslit arrays without and with graphene for different slit widths (fixed periodicity 500 nm). (c) Transmittance of selected slit widths of the structures with graphene at the bottom. (d) Enhancement factor ($EF = \frac{T_{Graphene}}{T_{Gold}}$) for selected slit widths compared by two cases.

To further investigate the physical explanations of the phenomenon observed in the spectra, we plot the vertical component of the electric field in side-view for the structure proposed before (500 nm periodicity and 20 nm slit width) at the wavelength of 13 μm. When there is no graphene, as shown in Figure 5.2.4(a), since gold serves much like the perfect conductor in mid-IR wavelength region, the electric field is mostly concentrated around the small slit. After combining with the graphene, the electric field is enhanced overall (Figure 5.2.4(b)), especially in the slit and on the graphene. The zoomed-in version

shown in Figure 5.2.4(c) indicates the plasmonic characteristic of the graphene with which the surface plasmons propagate. Due to the excitation of the SPPs in graphene sheet, more light can be coupled to the structure therefore increasing the overall transmission. Since the graphene surface plasmons are propagating back and forth horizontally in the period, the interference of them will lead to the oscillations in the spectra. When the periodicity is increasing with the fixed slit width, the overall effective permittivity of the gold grids is also increasing. And in this case, since the wavevector of the graphene SPPs also becomes larger, more SPPs are expected to propagate through one period, which accounts for the increasing of the oscillations in Figure 5.2.2(c).
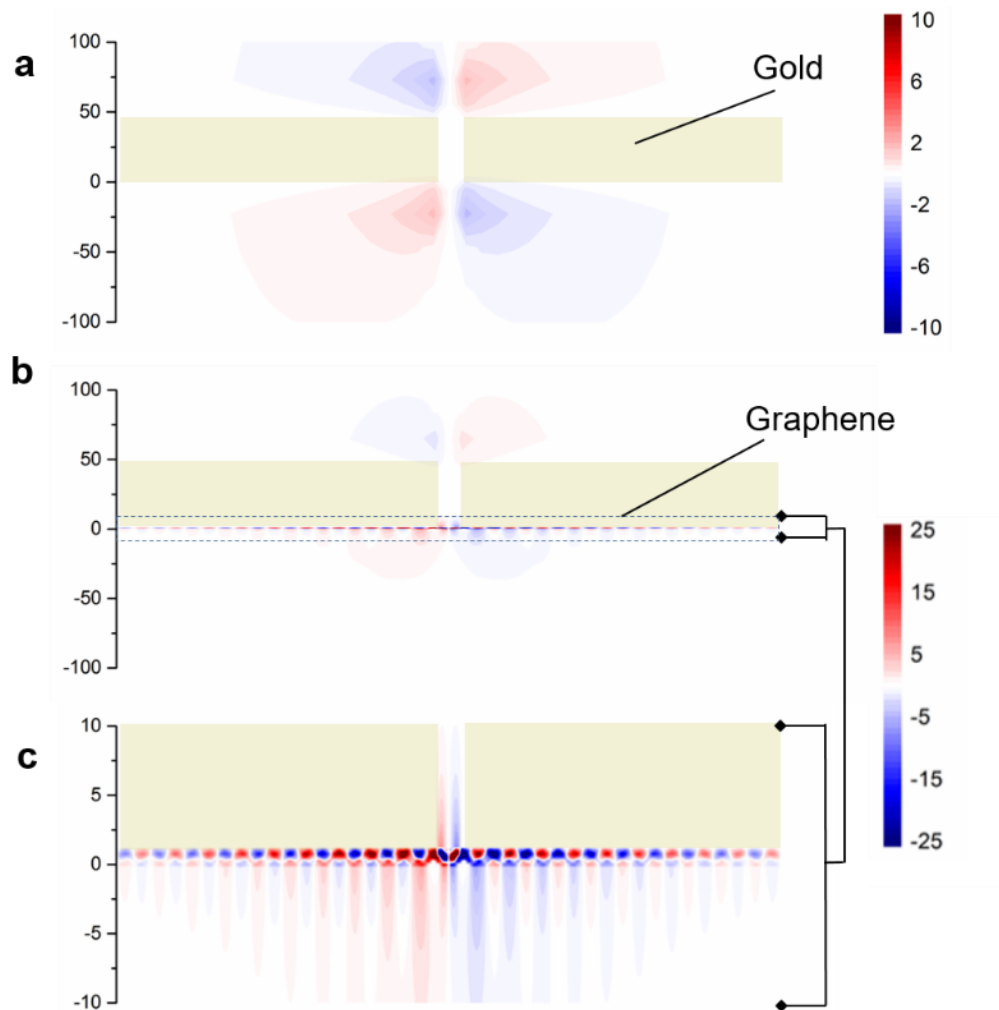
Figure 5.2.4 (a) Side-view electric field distribution of the gold nanoslit arrays structures. (b) and (c) Side-view electric field distribution of the hybrid structures.

5.3. Dynamic near-perfect absorption with controlled temperatures

Now let us move to the application of building the dynamic absorber with VO_2. The absorber is designed to operate at near infrared (near-IR) wavelengths. It is composed of VO_2 thin film on a gold reflecting substrate. VO_2 is a phase transition material that undergoes phase transition at 68 °C. Phase transition occurs through formation domain switching during which nanoscale metallic islands are formed inside an insulating film[87-

[94]. If the temperature is well above the transition temperature, metallic domains will merge together and form completely metallic thin film. The optical losses in VO_2 gradually increases as well. The absorption thus could be tuned by controlling the environmental temperature. Moreover, when the imaginary part of the VO_2 refractive index increases to the order of the real part, the losses cannot be considered as a perturbation anymore and the light is quickly attenuated due to the resonance behavior in the thin film[74]. Previously, thin-film VO_2 absorber on sapphire substrate has been proposed for mid-IR wavelength region[95]. Tunable absorption near visible wavelength region is also investigated with Pt back reflector. A comprehensive study for choosing epsilon-near-zero substrate has been showed and verified on tunable aluminum-doped zinc oxide substrate[96]. Here, we quantitatively utilize the effective medium theory to model the tunable optical response of VO_2 in the intermediate states, which could serve as a useful tool to understand this ultra-thin film absorption platform. Particularly, the metallic percentage factors in the material model are fitted for selected temperatures. We propose using gold substrate as a broadband reflective back mirror and obtaining the near-IR absorption resonances. This indicates that the absorption of the intermediate state is not necessarily due to the metamaterial structure. And the gold substrate could serve as an epsilon-near-zero material to fulfill the requirement for near-perfect absorption and make the absorption almost only occur in VO_2 in the near-infrared region. The performances for VO_2 film in 100 nm and 200 nm thickness are compared to both verify the effective medium theory model and show the possibility to shift the target resonances by changing the layer thickness. The mechanism of the thin

film absorption is also elaborated with the electric field distribution and absorbed power density map.

The tunable absorber design is schematically shown in Figure 5.3.1. The VO_2 thin film was first grown on a double side polished sapphire substrate. Then the sample was flipped over and an optically thick gold layer (150 nm) was deposited just on top of the VO_2 film. The near-IR light source was incident from the sapphire side and the sample was placed on a metal ceramic heater (below the gold layer) to control the temperature of the VO_2 film. Fourier transform infrared (FTIR) spectrometer was used to measure the reflection (R) from the sapphire side. Since the back gold layer served as a mirror in this case, no transmission could be observed. Thus, the absorption (A) in VO_2 could be deducted as $A = 1 - R$.
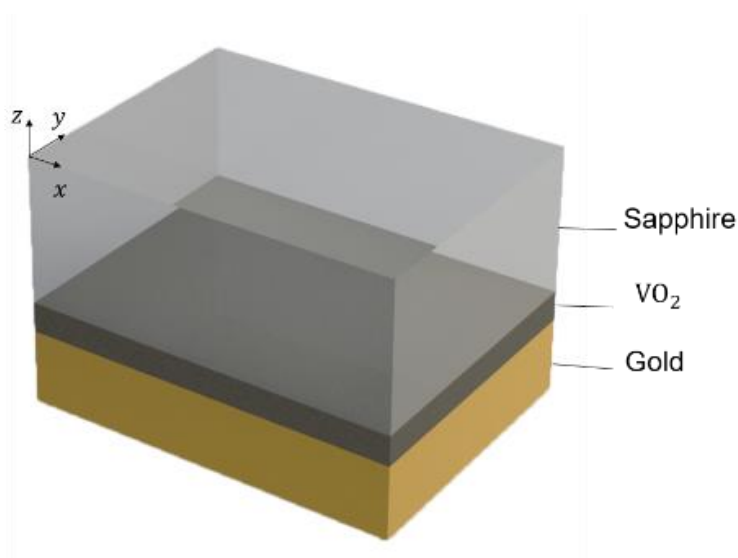
Figure 5.3.1. Schematics of VO_2 film grown on double polished sapphire with deposited gold. The near-IR light source was incident from the top side and the ceramic heater was placed below the gold.

To obtain the theoretical absorption of the proposed devices, FDTD modeling was used to calculate the optical response. The refractive index of the sapphire was chosen as 1.7 and the complex dispersive refractive index of gold was fitted from the Palik database[61]. The refractive indices of VO_2 in both dielectric (room temperature) case and metallic (hot temperature) case were taken from previous experimental study[97]. To calculate the optical response of the VO_2 in the intermediate states, we employ a Lorentz-Lorenz model to evaluate the binary mixture of two different permittivity. With this effective medium model, we could describe total response from both the surrounding dielectric VO_2 and the metallic nanoscale islands[98]. For the intermediate state, the polarization density P_i could be written as the mixture of the polarizations in dielectric (P_d) and metallic states (P_m)[99]:

$$P_i = \alpha P_m + (1 - \alpha)P_d$$

where α is the percentage of the metallic state. In particular, $\alpha = 0\%$ indicated the room temperature case and $\alpha = 100\%$ indicated the hot temperature case. The polarization density could be expressed with the Clausius-Mossotti relation. Thus, we obtained the corresponding permittivity with different metallic percentage factor α:

$$\frac{\epsilon_i - 1}{\epsilon_i + 2} = \alpha \frac{\epsilon_m - 1}{\epsilon_m + 2} + (1 - \alpha)\frac{\epsilon_d - 1}{\epsilon_d + 2}$$

Comparing with the previously employed Bruggeman model[87, 92], our effective medium model could also describe all the intermediate states but only one fitting parameter α is needed. After obtaining the permittivity for dielectric and metallic cases, the model could predict the optical collective response for states in between. As compared later with the experimental results, our effective medium model works quite well.

The VO_2 films were put in *x-y* planes with periodic boundary conditions in the simulation, as shown in Figure 5.3.1. Broadband near-IR plane waves were incident from *z* directions. Along the z directions, perfect matched layers were used to absorb all the electromagnetic power coming out to the boundaries. Electric field distribution was gathered by the field profile monitors around the structures.

Two samples with 100 nm and 200 nm thickness of VO_2 were prepared and measured with identical procedures. The measurements were taken by controlling the ceramic heater from room temperature 23 °C to hot temperature 120 °C with every 2 °C increments. To observe the hysteresis behavior[100], the reverse measurements were also taken by 2 °C decrements by cooling down the ceramic heater. The detailed measurement results including both the temperature-increasing and decreasing cases are presented in the Figure 5.3.3. In Figure 5.3.3(a) and Figure 5.3.3(c), we plot the selected normalized spectra taken from 100 nm and 200 nm thickness VO_2 samples in the temperature-increasing measurement. The phase transition happens around 68 °C. For both samples, we observed a red shift in the absorption peak position when transforming from the insulator state to the intermediate state. During the transition, the intensity of the resonance becomes higher and leads to almost perfect absorption around 1.5 μm for 100 nm VO_2 and 3 μm for 200 nm VO_2 layers. The absorbing film thickness is in the order of $\lambda/15$, which is very thin compared with the common Fabry-Perot cavities. While increasing the temperature, the VO_2 gradually becomes metallic beyond which no resonant behavior could be observed. In this case, the electromagnetic field partially penetrates the lossy VO_2 film and approximately 60% of the light was still absorbed over a broad range of wavelengths.

Figure 5.3.3(b) and Figure 5.3.3(d) present the corresponding simulation results. The metallic percentage factors were fitted for various temperatures to match the peak positions in the 100 nm thickness film measurements. Good agreement is shown between the calculated (Figure 5.3.3(b) and Figure 5.3.3(d)) and measured (Figure 5.3.3(a) and Figure 5.3.3(c)) optical responses, both in magnitude and in spectral profile. The calculated and measured absorption peak positions slightly deviate, which could be attributed to the differences in the growth conditions of our sample and the VO_2 measured in previous reference[91]. Nevertheless, it seems that the effective medium theory for VO_2 models the intermediate states quite well. The near perfect absorption performance is also well presented in the simulation results.
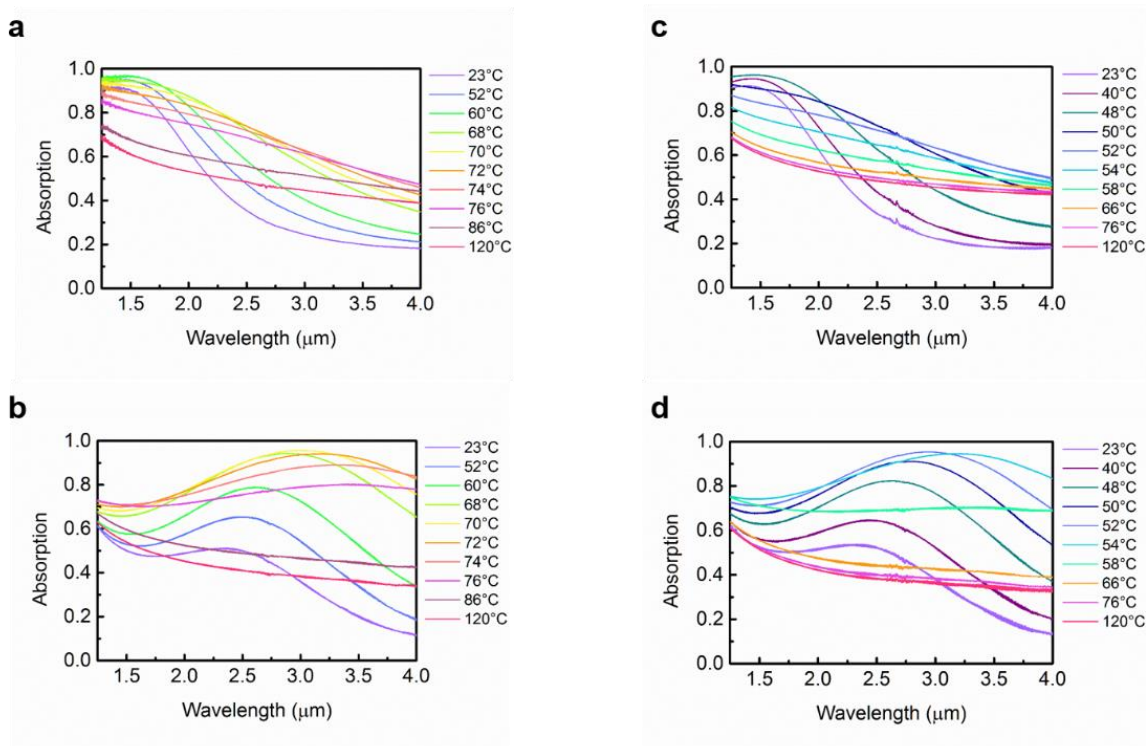
Figure 5.3.2. Measured absorption with more temperature data points for 100 nm thickness case (a and c) and 200 nm thickness case (b and d).
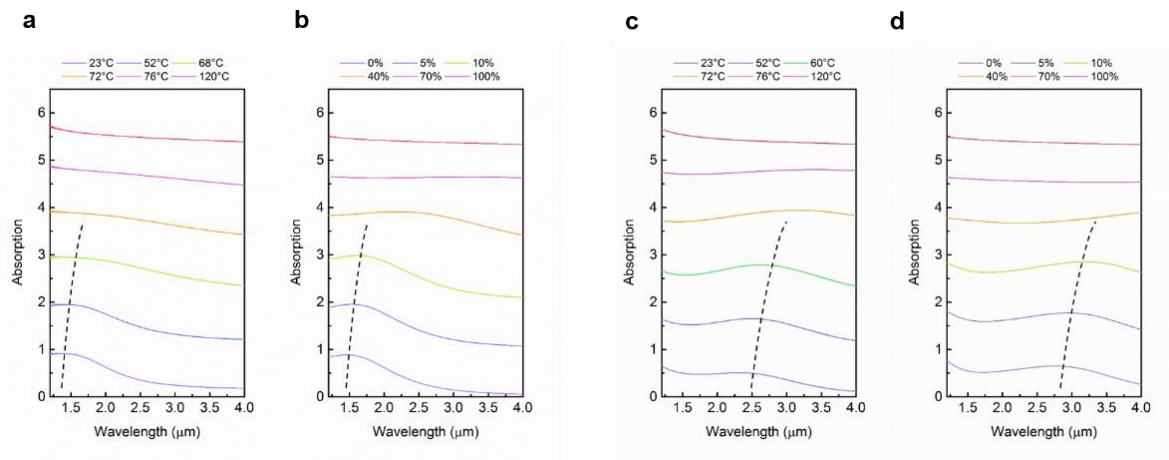
Figure 5.3.3. Absorption spectra with various material states. To compare the trend, the scale of the absorption is offseted by additional translation. The amplitude of the absorption for each material state is still in the range of 0 and 1 but with additional translation of 1,2,3,4 and 5 from states 2 to 6. (a, c) Measured absorption at selected temperatures for 100 nm thickness VO_2 and 200 nm thickness VO_2 respectively. (b, d) Calculated absorption with fitted metallic percentage factors for 100 nm thickness VO_2 and 200 nm thickness VO_2 respectively. The fitted dash lines track the shifts of resonance positions.

The expected hysteresis properties of the VO_2 based absorber have been observed in both cases as well. The absorption spectra at resonant wavelengths (1.5 μm for 100 nm VO_2 and 3 μm for 200 nm VO_2) as a function of temperature are plotted in Figure 5.3.4(a) and Figure 5.3.4(b), respectively. For both cases, ~15 °C hysteresis range was observed in the measurements. Note that the absorption for 200 nm VO_2 is substantially more sensitive to temperature change and that high absorption occurs only at narrow range of the temperature (~2 °C). On the other hand, in 100 nm VO_2, the absorption remains quite high over a range of about 20 °C.
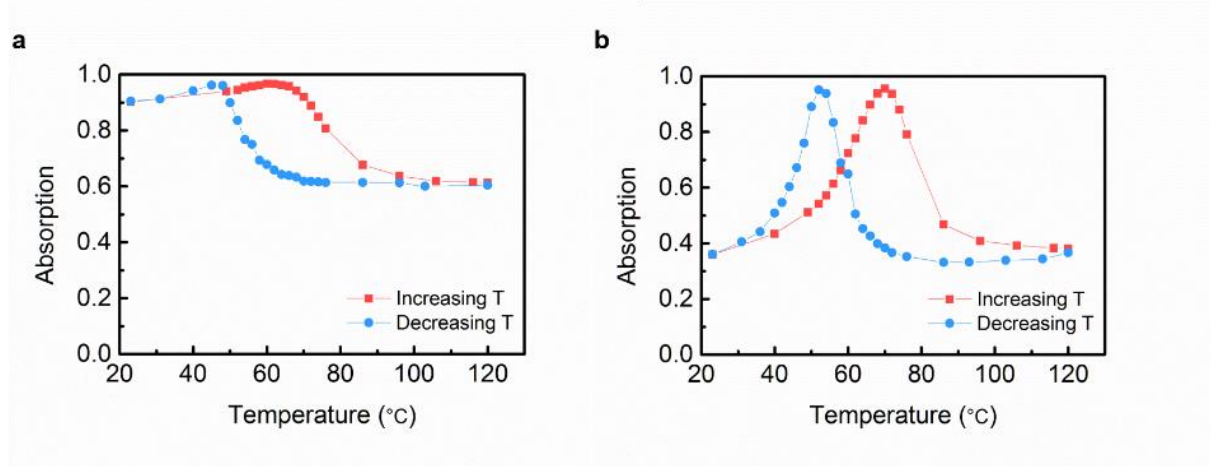
Figure 5.3.4. Measured absorption intensity as a function of increasing temperature and decreasing temperature at 1.5 μm wavelength for (a) 100 nm thickness VO_2 and at 3 μm wavelength for (b) 200 nm thickness VO_2.

To better understand the absorption mechanism, we calculate the absorption maps and the electric field distribution (as a function of wavelength and vertical position) of an intermediate state with metallic percentage α = 10%. The absorbed power density is calculated spatially using the equation $P = -\frac{1}{2}\omega|E|^2\epsilon''$, where ω is the angular optical frequency, ϵ'' is the imaginary part of the dielectric permittivity and $|E|^2$ is the intensity of the electric field. The maps for the 100 nm VO_2 layer cases are depicted in Figure 5.3.5(a) and Figure 5.3.5(c). It is clearly seen that near the interface of the VO_2 layer and back gold, the absorbed power is weak. The highest absorbed power is obtained around 1.5 μm and 3 μm for 100 nm VO_2 and 200 nm VO_2 respectively, which match the peak positions in the absorption spectra. The intensities of the electric field distributions (Figure 5.3.5(c) and Figure 5.3.5(d)) indicate that at the mentioned resonance peaks, the interference leads to weak electric field density at the interface of VO_2 layer and back gold. This explains why

the light is absorbed mostly in the top part of VO_2 film, near the sapphire side. As mentioned before, the enhanced electric field intensity near the top part stems from the reflection phase shift due to the high losses in the VO_2 film. The near-perfect absorption occurs at the wavelengths where the destructive interference largely suppresses the reflection. Note that at wavelengths far from the resonances, the electric field inside the VO_2 films is relatively weak.
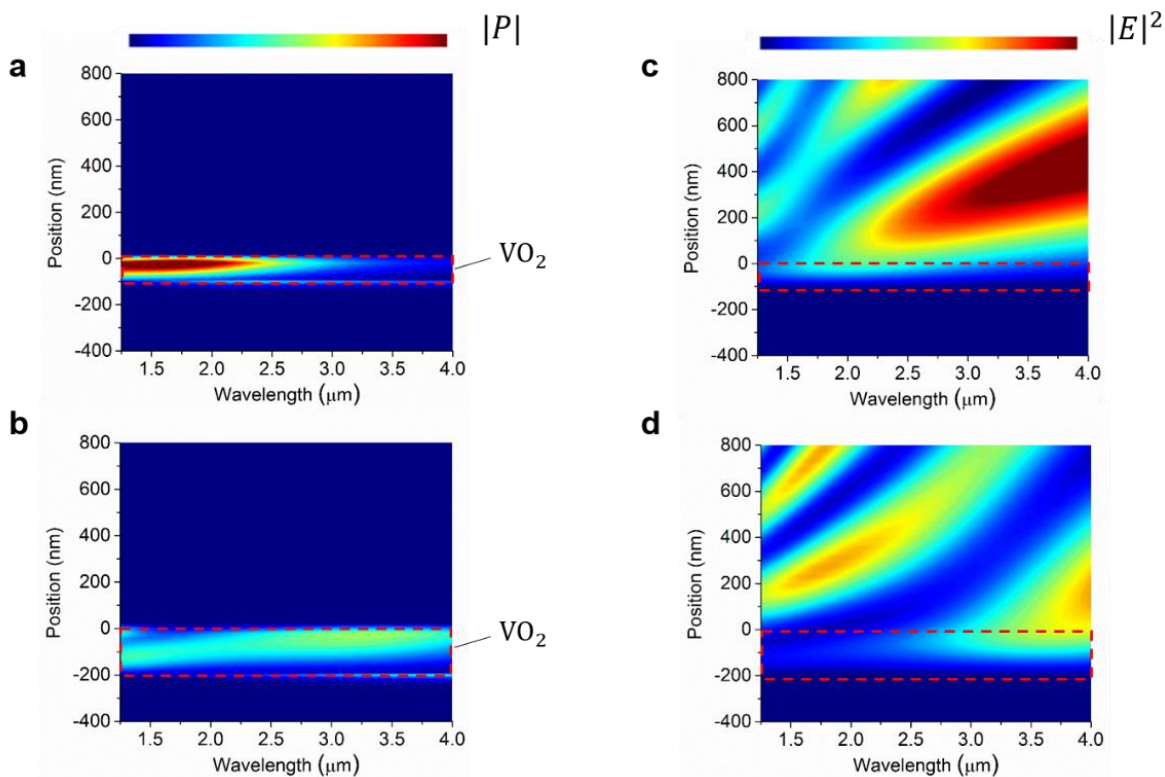
Figure 5.3.5. Calculated electrical field intensity distribution and absorption maps for (a, c) 100 nm thickness VO_2 and (b, d) 200 nm thickness VO_2. The left two plots show the absorbed power density maps. The positions of the VO_2 films are indicated by the dashed line.

5.4.   Chapter summary

In conclusion, we first investigate the graphene/gold nanoslit arrays hybrid structure. By making use of the excitations of SPPs in continuous graphene, it is possible to enhance the mid-IR transmission broadly through the gold nanoslit arrays structures. In addition, various structure parameters and the electric field distribution have been investigated with FDTD simulations to understand the underlying mechanism. This hybrid structure can also potentially help the study and control of propagating SPPs in continuous graphene sheet.

Then we investigated theoretically and experimentally a tunable thin absorber structure based on VO_2 phase transition. By enhancing the electromagnetic field above the reflector, the near-IR absorption in VO_2 thin films can be largely enhanced. The absorption intensity can be tuned by controlling the ambient temperature around the phase transition temperature. We utilized the effective medium model to fit the spectral properties of the intermediate states at selected temperatures. Good agreements were obtained between the calculated and measured optical responses. We also compare the hysteresis properties of VO_2 layers with electric field distribution and absorption maps. We believe this study will both enhance the fundamental understanding of the material properties of VO_2 and motivate new device design implementations including thin photodetectors, modulators and tunable emitters.

CHAPTER 6

Summary and Outlook

6.1. Hyperbolic metasurfaces with ultra-compact optical component

One future direction following the work I shown in this dissertation could be the hyperbolic metasurfaces, which could locally modify the phase, polarization and amplitude of the light to achieve exotic scattering properties, such as negative refraction, hyperlensing, and the generation of vortex beams.

The term "hyperbolic" is due to its hyperbolic dispersion of the material. Usually the hyperbolic metamaterial or metasurface needs to have positive permittivity at one direction and negative permittivity at the other direction at certain wavelengths. Figure 6.1(a) shows one of our previous work of using black phosphorus and silver alternating layers to achieve the hyperbolic metamaterials with different wavelengths working region[101]. For example, in region I, the permittivity is negative along z direction but positive along x and y directions. And we could also differentiate other regions with the negative permittivity at either x or y direction but with positive permittivity at z direction, or with positive permittivity at all three directions.

Making use of the confined surface plasmons polaritons, it is also possible to realize the in-plane near field guided light propagation for on-chip networks and in-plane imaging. IN this case, we need to introduce the in-plane anisotropy. And black phosphorus is an ideal material to fulfill that intrinsically. We could also use nanostructured graphene of thin metals to achieve the in-plane anisotropy. Figure 6.1(b) shows an example of using an isotropic metasurface (sheet 1) with an anisotropic σ-nearzero metasurface (sheet 2)[102].

Sheet 1 is excited by two *z*-oriented dipoles (depicted by magenta arrows) separated by a distance of 60 nm and located on the layer 2 nm from the interface. The color map illustrates the *z*-component of the electric field along the sheets. Insets show the isofrequency contour of each layer. This specific hyperbolic metasurface provides dispersion-free propagation and resolves the sources with subwavelength details preserved.
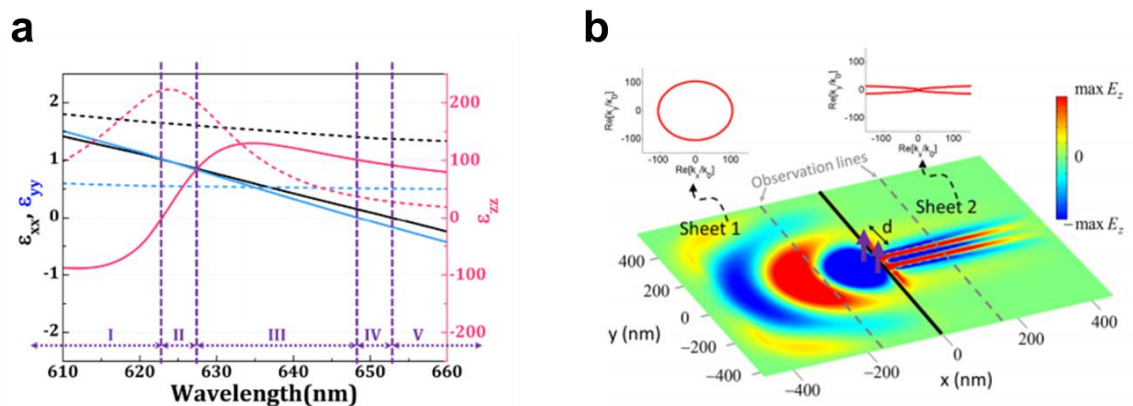
Figure 6.1. (a) Hyperbolic metamaterials with permittivity along different directions[101]. (b) Hyperbolic metasurfaces for hyper lensing[102].

6.2. Inverse design for efficient parameters design

The other direction of future opportunities could be using the up-to-date inverse design methods to efficiently guide the metasurface parameters design. Compared with the conventional forward design by heuristically choosing the structure parameters for specific optical performances, the inverse design goes through the process backward. The figure of merit is determined at the first, like the desired spectra. Then the algorithm will try to solve the Maxwell equations inversely and predict the required structure parameters. There are a

lot of inverse design methods in the field now, including adjoint-based method, objective-first optimization, genetic algorithms and so on.

Here I'd like to present deep learning method[103-106] for designing metasurfaces with DNA-mediated nanoparticles assembly. Figure 6.2 shows the framework of design paradigm. We want to generate the desired spectra for the structure with two gold nanocubes. We first pre-run thousands of simulations with various sizes, distances and orientations of the cubes. We also calculate two separate spectra for the same pattern but with different DNA lengths. Then we could try to build neural network with the spectra of both 3 nm and 20 nm DNA lengths as the input. The output of the network are just the parameters we need to build the structure. Once we finish training the network with the pre-run simulation results, we could set the desired spectra for both cases of DNA lengths and see what like of the parameters we need to set for the metasurfaces. In particular, the desired spectra are not necessarily in the training data set. The algorithm will take care of the fitting process.

There are two advantages of using the deep learning in this scenario. For one thing, with a lot of controllable parameters in the structures, it is almost impossible to run the simulations through the full sweep to understand how to adjust the peaks and dips. But with the deep learning method, we could actually control the contribution from all the parameters at the same time. The other advantage roots from the intrinsic control of two spectra from the input. For conventional design method, the whole design can only work for one specific design the environment, like the case for 3 nm DNA length. The spectra of the same structure at 20 nm DNA length is not in control when designing the structure.

However, with the deep learning, we could easily incorporate both spectra into the design paradigm and achieve the switchable functionality.
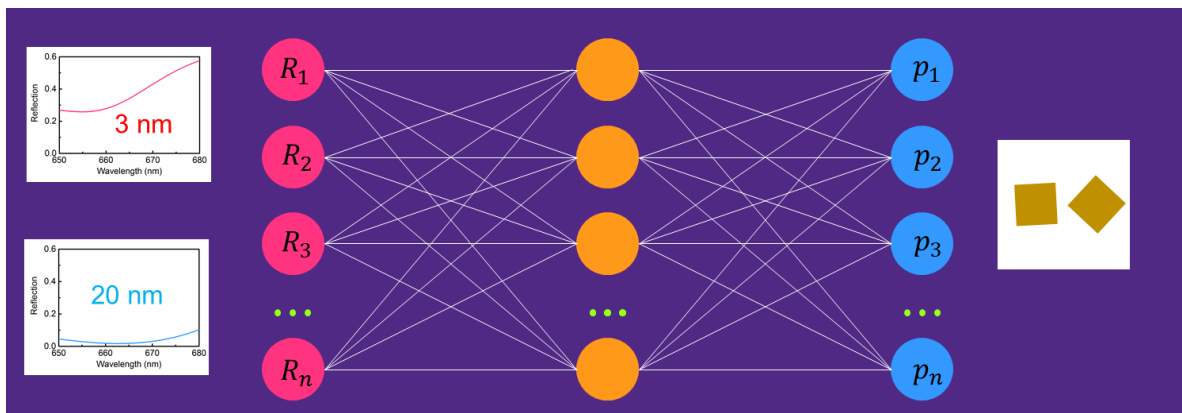
Figure 6.2. Deep learning for absorption modulations with two nanocubes on DNA-mediated surfaces.

6.3. Summary

To summary, in this dissertation, I show the possibility to achieve full active control of the electromagnetic waves with the platform in the flatland. We could achieve the amplitude control, the spatial phase control, and the temporal phase control. We use intrinsic anisotropy monolayer black phosphorus and the extrinsic control by combining metal antennas and thin film black phosphorus to achieve the polarization-controlled absorption and photodetection. The special patterning method using DNA-mediated nanoparticles assembly is presented, which provides an alternative platform to build the desired metasurface. The spatial phase control is achieved by patterning the nanoparticles at the substrate with designed phase profile. By controlling the DNA length, the performance of the metasurface could be tuned to switch functionality. We also achieve the temporal phase control by combining the active features of graphene and engineered phase control of

metasurfaces to fulfill time-varying metasurfaces. The ultrathin devices show quite a large degree for frequency conversion. Other than the three main parts of the control, I also discuss the enhanced transmission through the gold nanoslits by exciting the continuous graphene surface plasmons. An additional way of control if using temperature to tune the optical response of phase transition materials vanadium dioxide to build dynamic absorber. Some outlooks of combining the anisotropy in plane for the hyperbolic metasurfaces and the emerging inverse-design methods are also briefly discussed. We believe the flatland optics for the light-matter interaction control could become one of the center tasks for future optical components design. We don't know for sure how, when or even whether the flatland optics structures and designing principles presented in this dissertation will lead to a real industrial product, like a light-weight headset. But we know once it works, it will change the future.

REFERENCES

1.   Xia, F.; Wang, H.; Xiao, D.; Dubey, M.; Ramasubramaniam, A., Two-dimensional material nanophotonics. *Nat. Photonics* **2014,** *8* (12), 899-907.

2.   Koppens, F. H. L.; Mueller, T.; Avouris, P.; Ferrari, A. C.; Vitiello, M. S.; Polini, M., Photodetectors based on graphene, other two-dimensional materials and hybrid systems. *Nat. Nanotechnol.* **2014,** *9* (10), 780-793.

3.   Grigorenko, A. N.; Polini, M.; Novoselov, K. S., Graphene plasmonics. *Nat. Photonics* **2012,** *6* (11), 749-758.

4.   Gao, W.; Shu, J.; Qiu, C.; Xu, Q., Excitation of plasmonic waves in graphene by guided-mode resonances. *ACS Nano* **2012,** *6* (9), 7806-7813.

5.   Ju, L.; Geng, B.; Horng, J.; Girit, C.; Martin, M.; Hao, Z.; Bechtel, H. A.; Liang, X.; Zettl, A.; Shen, Y. R.; Wang, F., Graphene plasmonics for tunable terahertz metamaterials. *Nat. Nanotechnol.* **2011,** *6* (10), 630-4.

6.   Low, T.; Roldán, R.; Wang, H.; Xia, F.; Avouris, P.; Moreno, L. M.; Guinea, F., Plasmons and Screening in Monolayer and Multilayer Black Phosphorus. *Phys. Rev. Lett.* **2014,** *113* (10), 106802.

7.   Yan, H.; Li, X.; Chandra, B.; Tulevski, G.; Wu, Y.; Freitag, M.; Zhu, W.; Avouris, P.; Xia, F., Tunable infrared plasmonic devices using graphene/insulator stacks. *Nat. Nanotechnol.* **2012,** *7* (5), 330-4.

8.   Thongrattanasiri, S.; Koppens, F. H. L.; García de Abajo, F. J., Complete Optical Absorption in Periodically Patterned Graphene. *Phys. Rev. Lett.* **2012,** *108* (4).

9.   Yu, N.; Capasso, F., Flat optics with designer metasurfaces. *Nat. Mater.* **2014,** *13* (2), 139-50.

10.   Kildishev, A. V.; Boltasseva, A.; Shalaev, V. M., Planar photonics with metasurfaces. *Science* **2013,** *339* (6125), 1232009.

11.   Zheng, G.; Mühlenbernd, H.; Kenney, M.; Li, G.; Zentgraf, T.; Zhang, S., Metasurface holograms reaching 80% efficiency. *Nat. Nanotechnol.* **2015,** *10* (4), 308-312.

12.   Chen, H. T.; Taylor, A. J.; Yu, N., A review of metasurfaces: physics and applications. *Rep. Prog. Phys.* **2016,** *79* (7), 076401.

13.   Yu, N.; Genevet, P.; Kats, M. A.; Aieta, F.; Tetienne, J. P.; Capasso, F.; Gaburro, Z., Light propagation with phase discontinuities: generalized laws of reflection and refraction. *Science* **2011,** *334* (6054), 333-7.

14.   Ni, X.; Emani, N. K.; Kildishev, A. V.; Boltasseva, A.; Shalaev, V. M., Broadband Light Bending with Plasmonic Nanoantennas. *Science* **2012,** *335* (6067), 427-427.

15.   Khorasaninejad, M.; Chen, W. T.; Devlin, R. C.; Oh, J.; Zhu, A. Y.; Capasso, F., Metalenses at visible wavelengths: Diffraction-limited focusing and subwavelength resolution imaging. *Science* **2016,** *352* (6290), 1190-1194.

16.   Huang, Y. W.; Lee, H. W.; Sokhoyan, R.; Pala, R. A.; Thyagarajan, K.; Han, S.; Tsai, D. P.; Atwater, H. A., Gate-Tunable Conducting Oxide Metasurfaces. *Nano Lett.* **2016,** *16* (9), 5319-25.

17.   Balendhran, S.; Walia, S.; Nili, H.; Sriram, S.; Bhaskaran, M., Elemental Analogues of Graphene: Silicene, Germanene, Stanene, and Phosphorene. *Small* **2014**, *11* (6), 640-652.

18.   Xia, F.; Wang, H.; Jia, Y., Rediscovering black phosphorus as an anisotropic layered material for optoelectronics and electronics. *Nat. Commun.* **2014,** *5*, 4458.

19.   Zhang, S.; Yang, J.; Xu, R.; Wang, F.; Li, W.; Ghufran, M.; Zhang, Y.-W.; Yu, Z.; Zhang, G.; Qin, Q., Extraordinary photoluminescence and strong temperature/angle-dependent raman responses in few-layer phosphorene. *ACS Nano* **2014**, *8* (9), 9590-9596.

20.   Hao, C.; Yang, B.; Wen, F.; Xiang, J.; Li, L.; Wang, W.; Zeng, Z.; Xu, B.; Zhao, Z.; Liu, Z., Flexible All-Solid-State Supercapacitors based on Liquid-Exfoliated Black-Phosphorus Nanoflakes. *Adv. Mater.* **2016,** *28* (16), 3194-3201.

21.   Li, L.; Yu, Y.; Ye, G. J.; Ge, Q.; Ou, X.; Wu, H.; Feng, D.; Chen, X. H.; Zhang, Y., Black phosphorus field-effect transistors. *Nat. Nanotechnol.* **2014,** *9* (5), 372-7.

22.   Abbas, A. N.; Liu, B.; Chen, L.; Ma, Y.; Cong, S.; Aroonyadet, N.; Köpf, M.; Nilges, T.; Zhou, C., Black phosphorus gas sensors. *ACS Nano* **2015,** *9* (5), 5618-5624.

23.   Chen, X.; Lu, X.; Deng, B.; Sinai, O.; Shao, Y.; Li, C.; Yuan, S.; Tran, V.; Watanabe, K.; Taniguchi, T.; Naveh, D.; Yang, L.; Xia, F., Widely tunable black phosphorus mid-infrared photodetector. *Nat. Commun.* **2017,** *8* (1), 1672.

24.   Maier, S. A.; Atwater, H. A., Plasmonics: Localization and guiding of electromagnetic energy in metal/dielectric structures. *J. App. Phys.* **2005,** *98* (1), 10.

25.   Jablan, M.; Buljan, H.; Soljacic, M., Plasmonics in graphene at infrared frequencies. *Phys. Rev. B* **2009,** *80* (24), 245435.

26.   Nikitin, A. Y.; Low, T.; Martin-Moreno, L., Anomalous reflection phase of graphene plasmons and its influence on resonators. *Phys. Rev. B* **2014,** *90* (4), 041407.

27.   Li, X.; Zhu, J.; Wei, B., Hybrid nanostructures of metal/two-dimensional nanomaterials for plasmon-enhanced applications. *Chem. Soc. Rev.* **2016,** *45* (11), 3145-3187.

28.   Butun, S.; Tongay, S.; Aydin, K., Enhanced light emission from large-area monolayer MoS$_2$ using plasmonic nanodisc arrays. *Nano Lett.* **2015,** *15* (4), 2700-2704.

29.   Palacios, E.; Park, S.; Lauhon, L.; Aydin, K., Identifying excitation and emission rate contributions to plasmon-enhanced photoluminescence from monolayer MoS$_2$ using a tapered gold nanoantenna. *ACS Photonics* **2017,** *4* (7), 1602-1606.

30.   Liu, Z.; Aydin, K., Localized Surface Plasmons in Nanostructured Monolayer Black Phosphorus. *Nano Lett.* **2016,** *16* (6), 3457-62.

31.   Ling, X.; Huang, S.; Hasdeo, E. H.; Liang, L.; Parkin, W. M.; Tatsumi, Y.; Nugraha, A. R.; Puretzky, A. A.; Das, P. M.; Sumpter, B. G.; Geohegan, D. B.; Kong, J.; Saito, R.; Drndic, M.; Meunier, V.; Dresselhaus, M. S., Anisotropic Electron-Photon and Electron-Phonon Interactions in Black Phosphorus. *Nano Lett.* **2016,** *16* (4), 2260-7.

32.   Carvalho, A.; Wang, M.; Zhu, X.; Rodin, A. S.; Su, H. B.; Neto, A. H. C., Phosphorene: from theory to applications. *Nat. Rev. Mater.* **2016,** *1* (11), 16061.

33.   Liu, H.; Neal, A. T.; Zhu, Z.; Luo, Z.; Xu, X.; Tomanek, D.; Ye, P. D., Phosphorene: an unexplored 2D semiconductor with a high hole mobility. *ACS Nano* **2014,** *8* (4), 4033-41.

34.   Wang, X.; Jones, A. M.; Seyler, K. L.; Tran, V.; Jia, Y.; Zhao, H.; Wang, H.; Yang, L.; Xu, X.; Xia, F., Highly anisotropic and robust excitons in monolayer black phosphorus. *Nat. Nanotechnol.* **2015,** *10* (6), 517-21.

35.   Tran, V.; Soklaski, R.; Liang, Y. F.; Yang, L., Layer-controlled band gap and anisotropic excitons in few-layer black phosphorus. *Phys. Rev. B* **2014,** *89* (23).

36.   Buscema, M.; Groenendijk, D. J.; Blanter, S. I.; Steele, G. A.; van der Zant, H. S.; Castellanos-Gomez, A., Fast and broadband photoresponse of few-layer black phosphorus field-effect transistors. *Nano Lett.* **2014,** *14* (6), 3347-52.

37.   Hong, T.; Chamlagain, B.; Lin, W.; Chuang, H.-J.; Pan, M.; Zhou, Z.; Xu, Y.-Q., Polarized photocurrent response in black phosphorus field-effect transistors. *Nanoscale* **2014,** *6* (15), 8978-8983.

38.   Suess, R. J.; Leong, E.; Garrett, J. L.; Zhou, T.; Salem, R.; Munday, J. N.; Murphy, T. E.; Mittendorff, M., Mid-infrared time-resolved photoconduction in black phosphorus. *2d Mater.* **2016,** *3* (4).

39.   Youngblood, N.; Chen, C.; Koester, S. J.; Li, M., Waveguide-integrated black phosphorus photodetector with high responsivity and low dark current. *Nat. Photonics* **2015,** *9* (4), 247-252.

40.   Liu, X.; Ryder, C. R.; Wells, S. A.; Hersam, M. C., Resolving the In-Plane Anisotropic Properties of Black Phosphorus. *Small Methods* **2017**, *1* (6), 1700143.

41.   Zhang, G.; Huang, S.; Chaves, A.; Song, C.; Özçelik, V. O.; Low, T.; Yan, H., Infrared fingerprints of few-layer black phosphorus. *Nat. Commun.* **2017,** *8*, 14071.

42.   Mao, N.; Tang, J.; Xie, L.; Wu, J.; Han, B.; Lin, J.; Deng, S.; Ji, W.; Xu, H.; Liu, K.; Tong, L.; Zhang, J., Optical Anisotropy of Black Phosphorus in the Visible Regime. *J. Am. Chem. Soc.* **2016,** *138* (1), 300-305.

43.   Fei, R.; Yang, L., Strain-engineering the anisotropic electrical conductance of few-layer black phosphorus. *Nano Lett.* **2014,** *14* (5), 2884-9.

44.   Lan, S. F.; Rodrigues, S.; Kang, L.; Cai, W. S., Visualizing Optical Phase Anisotropy in Black Phosphorus. *Acs Photonics* **2016,** *3* (7), 1176-1181.

45.   Buscema, M.; Groenendijk, D. J.; Steele, G. A.; van der Zant, H. S.; Castellanos-Gomez, A., Photovoltaic effect in few-layer black phosphorus PN junctions defined by local electrostatic gating. *Nat. Commun.* **2014,** *5*, 4651.

46.   Yuan, H.; Liu, X.; Afshinmanesh, F.; Li, W.; Xu, G.; Sun, J.; Lian, B.; Curto, A. G.; Ye, G.; Hikita, Y.; Shen, Z.; Zhang, S. C.; Chen, X.; Brongersma, M.; Hwang, H. Y.; Cui, Y., Polarization-sensitive broadband photodetector using a black phosphorus vertical p-n junction. *Nat. Nanotechnol.* **2015,** *10* (8), 707-13.

47.   Hong, T.; Chamlagain, B.; Wang, T.; Chuang, H. J.; Zhou, Z.; Xu, Y. Q., Anisotropic photocurrent response at black phosphorus-MoS$_2$ p-n heterojunctions. *Nanoscale* **2015,** *7* (44), 18537-41.

48.   Youngblood, N.; Li, M., Ultrafast photocurrent measurements of a black phosphorus photodetector. *Appl.Phys. Lett.* **2017,** *110* (5), 051102.

49.   Chen, C.; Youngblood, N.; Peng, R.; Yoo, D.; Mohr, D. A.; Johnson, T. W.; Oh, S. H.; Li, M., Three-Dimensional Integration of Black Phosphorus Photodetector with Silicon Photonics and Nanoplasmonics. *Nano Lett.* **2017,** *17* (2), 985-991.

50.   Bellus, M. Z.; Yang, Z. B.; Hao, J. H.; Lau, S. P.; Zhao, H., Amorphous two-dimensional black phosphorus with exceptional photocarrier transport properties. *2d Mater.* **2017,** *4* (2).

51.   Guo, Q.; Pospischil, A.; Bhuiyan, M.; Jiang, H.; Tian, H.; Farmer, D.; Deng, B.; Li, C.; Han, S. J.; Wang, H.; Xia, Q.; Ma, T. P.; Mueller, T.; Xia, F., Black Phosphorus Mid-Infrared Photodetectors with High Gain. *Nano Lett.* **2016,** *16* (7), 4648-55.

52.   Butun, S.; Palacios, E.; Cain, J. D.; Liu, Z.; Dravid, V. P.; Aydin, K., Quantifying Plasmon-Enhanced Light Absorption in Monolayer WS$_2$ Films. *ACS Appl. Mater. Interfaces.* **2017,** *9* (17), 15044-15051.

53.   Kern, J.; Trügler, A.; Niehues, I.; Ewering, J.; Schmidt, R.; Schneider, R.; Najmaei, S.; George, A.; Zhang, J.; Lou, J., Nanoantenna-enhanced light–matter interaction in atomically thin WS$_2$. *ACS Photonics* **2015,** *2* (9), 1260-1265.

54.   Liu, F.; Zheng, S.; He, X.; Chaturvedi, A.; He, J.; Chow, W. L.; Mion, T. R.; Wang, X.; Zhou, J.; Fu, Q., Highly sensitive detection of polarized light using anisotropic 2D ReS$_2$. *Adv. Funct. Mater.* **2016,** *26* (8), 1169-1177.

55.   Lee, B.; Park, J.; Han, G. H.; Ee, H.-S.; Naylor, C. H.; Liu, W.; Johnson, A. C.; Agarwal, R., Fano resonance and spectrally modified photoluminescence enhancement in monolayer MoS2 integrated with plasmonic nanoantenna array. *Nano Lett.* **2015,** *15* (5), 3646-3653.

56.   Khaliji, K.; Fallahi, A.; Martin-Moreno, L.; Low, T., Tunable plasmon-enhanced birefringence in ribbon array of anisotropic two-dimensional materials. *Phys. Rev. B* **2017,** *95* (20), 201401.

57.   Zhang, E.; Wang, P.; Li, Z.; Wang, H.; Song, C.; Huang, C.; Chen, Z.-G.; Yang, L.; Zhang, K.; Lu, S., Tunable ambipolar polarization-sensitive photodetectors based on high-anisotropy ReSe$_2$ nanosheets. *ACS Nano* **2016,** *10* (8), 8067-8077.

58.   Huang, S.; Tatsumi, Y.; Ling, X.; Guo, H.; Wang, Z.; Watson, G.; Puretzky, A. A.; Geohegan, D. B.; Kong, J.; Li, J., In-plane optical anisotropy of layered gallium telluride. *ACS Nano* **2016,** *10* (9), 8964-8972.

59.   Wood, J. D.; Wells, S. A.; Jariwala, D.; Chen, K. S.; Cho, E.; Sangwan, V. K.; Liu, X.; Lauhon, L. J.; Marks, T. J.; Hersam, M. C., Effective passivation of exfoliated black phosphorus transistors against ambient degradation. *Nano Lett.* **2014,** *14* (12), 6964-70.

60.   Asahina, H.; Morita, A., Band-Structure and Optical-Properties of Black Phosphorus. *J Phys. C Solid State* **1984,** *17* (11), 1839-1852.

61.   Palik, E. D., *Handbook of optical constants of solids*. Academic press: 1998; Vol. 3.

62.   Lin, J.; Li, H.; Zhang, H.; Chen, W., Plasmonic enhancement of photocurrent in MoS2 field-effect-transistor. *Appl. Phys. Lett.* **2013,** *102* (20), 203109.

63.   Lin, Q.-Y.; Li, Z.; Brown, K. A.; O'Brien, M. N.; Ross, M. B.; Zhou, Y.; Butun, S.; Chen, P.-C.; Schatz, G. C.; Dravid, V. P.; Aydin, K.; Mirkin, C. A., Strong Coupling between Plasmonic Gap Modes and Photonic Lattice Modes in DNA-Assembled Gold Nanocube Arrays. *Nano Lett.* **2015,** *15* (7), 4699-4703.

64.   Mason, J. A.; Laramy, C. R.; Lai, C.-T.; O'Brien, M. N.; Lin, Q.-Y.; Dravid, V. P.; Schatz, G. C.; Mirkin, C. A., Contraction and Expansion of Stimuli-Responsive DNA Bonds in Flexible Colloidal Crystals. *J. Am. Chem. Soc.***2016,** *138* (28), 8722-8725.

65.   Shaltout, A.; Kildishev, A.; Shalaev, V., Time-varying metasurfaces and Lorentz non-reciprocity. *Opt. Mater. Express* **2015,** *5* (11), 2459-2467.

66.   Mak, K. F.; Sfeir, M. Y.; Wu, Y.; Lui, C. H.; Misewich, J. A.; Heinz, T. F., Measurement of the Optical Conductivity of Graphene. *Phys. Rev. Lett.* **2008,** *101* (19), 196405.

67.   Ebbesen, T. W.; Lezec, H.; Ghaemi, H.; Thio, T.; Wolff, P., Extraordinary optical transmission through sub-wavelength hole arrays. *Nature* **1998,** *391* (6668), 667-669.

68.   Aydin, K.; Ferry, V. E.; Briggs, R. M.; Atwater, H. A., Broadband polarization-independent resonant light absorption using ultrathin plasmonic super absorbers. *Nat. Commun.s* **2011,** *2*, 517.

69.   Cui, Y.; He, Y.; Jin, Y.; Ding, F.; Yang, L.; Ye, Y.; Zhong, S.; Lin, Y.; He, S., Plasmonic and metamaterial structures as electromagnetic absorbers. *Laser Photonics Rev.* **2014,** *8* (4), 495-520.

70.   Landy, N. I.; Sajuyigbe, S.; Mock, J.; Smith, D.; Padilla, W., Perfect metamaterial absorber. *Phy. Rev. Rett.* **2008,** *100* (20), 207402.

71.   Li, Z.; Butun, S.; Aydin, K., Ultranarrow band absorbers based on surface lattice resonances in nanostructured metal surfaces. *ACS Nano* **2014,** *8* (8), 8242-8.

72.   Li, Z.; Butun, S.; Aydin, K., Large-area, lithography-free super absorbers and color filters at visible frequencies using ultrathin metallic films. *ACS Photonics* **2015,** *2* (2), 183-188.

73.   Shu, S.; Li, Z.; Li, Y. Y., Triple-layer Fabry-Perot absorber with near-perfect absorption in visible and near-infrared regime. *Opt. Express* **2013,** *21* (21), 25307-25315.

74.   Kats, M. A.; Blanchard, R.; Genevet, P.; Capasso, F., Nanometre optical coatings based on strong interference effects in highly absorbing media. *Nat. Mater.* **2013,** *12* (1), 20-4.

75.   Li, Z.; Palacios, E.; Butun, S.; Kocer, H.; Aydin, K., Omnidirectional, broadband light absorption using large-area, ultrathin lossy metallic film coatings. *Sci. Rep.* **2015,** *5*, 15137.

76.   Yan, R.; Simes, R.; Coldren, L., Electroabsorptive Fabry-Perot reflection modulators with asymmetric mirrors. *IEEE Photonics Technol. Lett.* **1989,** *1* (9), 273-275.

77.   Law, K. K.; Yan, R.; Coldren, L.; Merz, J., Self-electro-optic device based on a superlattice asymmetric Fabry–Perot modulator with an on/off ratio$\gtrsim$ 100: 1. *Appl. Phys. Lett.* **1990,** *57* (13), 1345-1347.

78.   Ünlü, M. S.; Strite, S., Resonant cavity enhanced photonic devices. *J. Appl. Phys.* **1995,** *78* (2), 607-639.

79.   Chin, A.; Chang, T., Multilayer reflectors by molecular-beam epitaxy for resonance enhanced absorption in thin high-speed detectors. *J. Vac. Sci. Technol., B: Microelectron. Process. Phenom.* **1990,** *8* (2), 339-342.

80.   Nefzaoui, E.; Drevillon, J.; Ezzahri, Y.; Joulain, K., Simple far-field radiative thermal rectifier using Fabry–Perot cavities based infrared selective emitters. *Appl. Opt.* **2014,** *53* (16), 3479-3485.

81.   Streyer, W.; Law, S.; Rooney, G.; Jacobs, T.; Wasserman, D., Strong absorption and selective emission from engineered metals with dielectric coatings. *Opt. Express* **2013,** *21* (7), 9113-9122.

82.   Kocer, H.; Butun, S.; Banar, B.; Wang, K.; Tongay, S.; Wu, J.; Aydin, K., Thermal tuning of infrared resonant absorbers based on hybrid gold-VO_2 nanostructures. *Appl. Phys. Lett.* **2015,** *106* (16).

83.   Kishino, K.; Unlu, M. S.; Chyi, J.-I.; Reed, J.; Arsenault, L.; Morkoc, H., Resonant cavity-enhanced (RCE) photodetectors. *IEEE J. Quantum Electron.* **1991,** *27* (8), 2025-2034.

84.   Kocer, H.; Butun, S.; Palacios, E.; Liu, Z.; Tongay, S.; Fu, D.; Wang, K.; Wu, J.; Aydin, K., Intensity tunable infrared broadband absorbers based on VO_2 phase transition using planar layered thin films. *Sci. Rep.* **2015,** *5*, 13384.

85. Zhu, X.; Yan, W.; Uhd Jepsen, P.; Hansen, O.; Asger Mortensen, N.; Xiao, S., Experimental observation of plasmons in a graphene monolayer resting on a two-dimensional subwavelength silicon grating. *Appl. Phys. Lett.* **2013,** *102* (13), 131101.

86. Yeh, P., A new optical model for wire grid polarizers. *Opt. Commun.* **1978,** *26* (3), 289-292.

87. Qazilbash, M. M.; Brehm, M.; Chae, B. G.; Ho, P. C.; Andreev, G. O.; Kim, B. J.; Yun, S. J.; Balatsky, A. V.; Maple, M. B.; Keilmann, F.; Kim, H. T.; Basov, D. N., Mott transition in VO_2 revealed by infrared spectroscopy and nano-imaging. *Science* **2007,** *318* (5857), 1750-3.

88. Choi, H. S.; Ahn, J. S.; Jung, J. H.; Noh, T. W.; Kim, D. H., Mid-infrared properties of a VO_2 film near the metal-insulator transition. *Phys. Rev. B* **1996,** *54* (7), 4621-4628.

89. Zhang, G.; Ma, H.; Lan, C.; Gao, R.; Zhou, J., Microwave Tunable Metamaterial Based on Semiconductor-to-Metal Phase Transition. *Sci. Rep.***2017,** *7* (1), 5773.

90. Wehmeyer, G.; Yabuki, T.; Monachon, C.; Wu, J.; Dames, C., Thermal diodes, regulators, and switches: Physical mechanisms and potential applications. *Appl. Phys. Rev.* **2017,** *4* (4), 041304.

91. Wang, S.; Kang, L.; Werner, D. H., Hybrid Resonators and Highly Tunable Terahertz Metamaterials Enabled by Vanadium Dioxide (VO_2). *Sci. Rep.* **2017,** *7* (1), 4326.

92. Rensberg, J.; Zhang, S.; Zhou, Y.; McLeod, A. S.; Schwarz, C.; Goldflam, M.; Liu, M.; Kerbusch, J.; Nawrodt, R.; Ramanathan, S., Active optical metasurfaces based on defect-engineered phase-transition materials. *Nano Lett.* **2016,** *16* (2), 1050-1055.

93. Menges, F.; Dittberner, M.; Novotny, L.; Passarello, D.; Parkin, S.; Spieser, M.; Riel, H.; Gotsmann, B., Thermal radiative near field transport between vanadium dioxide

and silicon oxide across the metal insulator transition. *Appl. Phys. Lett.* **2016,** *108* (17), 171904.

94.   Currie, M.; Mastro, M. A.; Wheeler, V. D., Characterizing the tunable refractive index of vanadium dioxide. *Opt. Mater. Express* **2017,** *7* (5), 1697-1707.

95.   Kats, M. A.; Sharma, D.; Lin, J.; Genevet, P.; Blanchard, R.; Yang, Z.; Qazilbash, M. M.; Basov, D. N.; Ramanathan, S.; Capasso, F., Ultra-thin perfect absorber employing a tunable phase change material. *Appl. Phys. Lett.* **2012,** *101* (22), 221101.

96.   Rensberg, J.; Zhou, Y.; Richter, S.; Wan, C.; Zhang, S.; Schöppe, P.; Schmidt-Grund, R.; Ramanathan, S.; Capasso, F.; Kats, M. A., Epsilon-Near-Zero Substrate Engineering for Ultrathin-Film Perfect Absorbers. *Phys. Rev. Appl.* **2017,** *8* (1), 014009.

97.   Dicken, M. J.; Aydin, K.; Pryce, I. M.; Sweatlock, L. A.; Boyd, E. M.; Walavalkar, S.; Ma, J.; Atwater, H. A., Frequency tunable near-infrared metamaterials based on VO< sub> 2</sub> phase transition. *Opt. Express* **2009,** *17* (20), 18330-18339.

98.   Webman, I.; Jortner, J.; Cohen, M. H., Theory of optical and microwave properties of microscopically inhomogeneous materials. *Phys. Rev. B* **1977,** *15* (12), 5712.

99.   Kaplan, G.; Aydin, K.; Scheuer, J., Dynamically controlled plasmonic nano-antenna phased array utilizing vanadium dioxide [Invited]. *Opt. Mater. Express* **2015,** *5* (11), 2513-2524.

100.   Beteille, F.; Livage, J., Optical switching in VO_2 thin films. *J. Sol-Gel Sci.Technol.* **1998,** *13* (1-3), 915-921.

101.   Song, X.; Liu, Z.; Xiang, Y.; Aydin, K., Biaxial hyperbolic metamaterials using anisotropic few-layer black phosphorus. *Opt. Express* **2018,** *26* (5), 5469-5477.

102.   Gomez-Diaz, J. S.; Alù, A., Flatland Optics with Hyperbolic Metasurfaces. *ACS Photonics* **2016,** *3* (12), 2211-2224.

103.   Malkiel, I.; Mrejen, M.; Nagler, A.; Arieli, U.; Wolf, L.; Suchowski, H. Deep learning for the design of nano-photonic structures, *IEEE International Conference on Computational Photography,* **2018,** 1-14.

104.   Liu, D.; Tan, Y.; Khoram, E.; Yu, Z., Training Deep Neural Networks for the Inverse Design of Nanophotonic Structures. *ACS Photonics* **2018,** *5* (4), 1365-1369.

105.   Peurifoy, J.; Shen, Y.; Jing, L.; Yang, Y.; Cano-Renteria, F.; DeLacy, B. G.; Joannopoulos, J. D.; Tegmark, M.; Soljačić, M., Nanophotonic particle simulation and inverse design using artificial neural networks. *Sci. Adv.* **2018,** *4* (6).

106.   Ma, W.; Cheng, F.; Liu, Y., Deep-Learning-Enabled On-Demand Design of Chiral Metamaterials. *ACS Nano* **2018,** *12* (6), 6326-6334.